GEOTHERMAL HEAT SOURCES CHARACTERIZATION AND MAPPING USING HEAT FLOW, GRAVITY, AND MAGNETICS IN EBURRU, KENYA

ERICK RAYORA NYAKUNDI

DOCTOR OF PHILOSOPHY

(Physics)

JOMO KENYATTA UNIVERSITY

OF

AGRICULTURE AND TECHNOLOGY

2022

Geothermal heat sources characterization and mapping using heat flow, gravity, and magnetics in Eburru, Kenya

Erick Rayora Nyakundi

A Thesis Submitted in Partial Fulfillment for the degree of Doctor of Philosophy in Physics in the Jomo Kenyatta University of Agriculture and Technology

2022

DECLARATION

This thesis is my original work and has not been presented for a degree in any other university.

Signature: …….. Date: ……

Erick Rayora Nyakundi

This thesis has been submitted for examination with our approval as the university Supervisors.

Signature: …… Date: …….

Prof. John Githiri, Ph.D.

JKUAT, Kenya

Signature: …… Date: …….

Dr. Maurice K'Orowe, Ph.D.

JKUAT, Kenya

DEDICATION

This thesis work is a special dedication to my lovely daughter June. She has been an encouragement and inspiration to me. God bless her abundantly.

ACKNOWLEDGEMENTS

First, I thank the Almighty God for making this Ph.D. program journey a success. He gave me good health, strength and protected me throughout the program.

Secondly, I wish to thank my university supervisors' Prof. John Githiri and Dr. Maurice K'Orowe, for their technical guidance in this work. They devoted their time to check my work regularly. They gave suggestions and contributions, which improved and made this work better. I also wish to thank the entire Department of Physics, Jomo Kenyatta University of Agriculture and Technology, for their positive criticism, contributions, and support that ensured the successful completion of this program.

Thirdly, special thanks go to the Kenya Electricity Generating Company (KenGen) for aiding in geophysical data collection and the Oasis montaj geosoft program used for data processing, analysis, and interpretation. Geophysical data were collected using three geophysical methods covering a large geographical area which was tedious and expensive. I, therefore, appreciate KenGen for making it easier and possible. I also acknowledge geologist Risper Kandie for welcoming and introducing me to KenGen. I appreciate the mining ministry for availing geological maps and reports for this study area which was paramount during interpretation. I also recognise my friend Joseph Gichira from GDC for the professional discussions we held.

Lastly, I wish to thank my family for their financial support, motivation, and humble time completing this work. I appreciate my lovely daughter Joan, born during this study, and she incredibly energized me. Thanks to my dear parents, Hellen and Vincent, for their prayers and inspiration. I salute my brother Aliphonce. I also acknowledge the Department of Physics, Kisii University, for the motivation and humble time to complete this work. Thank you all, and God bless.

TABLE OF CONTENTS

LIST OF FIGURES

LIST OF APPENDICES

LIST OF ABBREVIATIONS AND ACRONYMS

BC	Bouguer Correction
CBA	Complete Bouguer Anomaly
Cgs	Centimetre gram second
CPD	Curie Point Depth
D	Declination
FAC	Free Air Correction
FFT	Fast Fourier Transform
G	Universal gravitational constant
GA	Absolute gravity
GDC	Geothermal Development Company
GOK	Government of Kenya
GM − Sys	Geosoft Modelling System
GPS	Global Positioning System
HRAM	High Resolution Aeromagnetic
I	Inclination
IGRF	International Geomagnetic Reference Field
LC	Latitude Correction
M	Thermal gradient
m. b. s. l	metres below sea level
MT	Magnetotelluric
nT	nanotesla
Q	Quantity of heat
q	Heat flux
RTP	Reduction to Pole
TC	Terrain Correction
TEM	Transient Electromagnetics
V	Gravitational potential

$\mathbf{VE}$	Vertical Exaggeration
$\mathbf{g_z}$	The vertical component of gravity
$\mathbf{M_e}$	Mass of Earth
$\mathbf{R_e}$	Radius of Earth
$\mathbf{T_c}$	Curie temperature
$\mathbf{wm^{-1}{}^{\circ}C^{-1}}$	Watts per metre per degrees Celsius
$\boldsymbol{\rho}$	Average density of crustal rocks
$\boldsymbol{\mu}$	Magnetic permeability
$\mathbf{2D}$	Two dimensional
$\mathbf{3D}$	Three dimensional

ABSTRACT

Eburru area is a geothermal heat prospect region in Kenya's Rift Valley. The area is characterized by faults, fumaroles, geysers, volcanic craters, geothermal grass, and hot springs. Such surface manifestations indicate a possible occurrence of a geothermal heat source. Six exploration wells were drilled in the Southern part of the study area within the Eburru crater. Five wells did not produce steam pressure; hence there was a need to determine the depth of the heat sources and their characterization in the area. Previous studies were mainly carried out within the Eburru crater; however, this study covered a larger area for better imaging of deep heat structures. This study undertook a geophysical survey using heat flow, gravity, and magnetic geophysical methods to map and characterize the structures likely to be possible geothermal heat sources in the area. Spike mechanical tool was used for hole digging, while a thermocouple thermometer was used for temperature measurements during heat flow data collection. Gravity data were collected using a CG-5 gravimeter, and magnetic data were collected using a proton precession magnetometer G-856 model. The data were processed and analysed using Oasis montaj geosoft software. The heat flow data was used to plot thermal contour maps, which identified high and low heat flux areas. The gravity and magnetic data were reduced and processed to obtain anomalies that showed the variation of density and magnetic susceptibility within the Earth's subsurface. Gravity and magnetic data were forward modelled using Oasis Montaj geosoft software to determine the causative sources' depth, density, and magnetic susceptibility. Heat flux values were estimated to range between $0.02\ \mathrm{Wm^{-2}}$ and $92.80\ \mathrm{Wm^{-2}}$ with a mean of $10.06\ \mathrm{Wm^{-2}}$. Processed gravity and magnetic data revealed positive and negative anomalies. Euler deconvolution of gravity data located five solutions on high gravity amplitudes at a depth range of $433\ \mathrm{m} - 2271\ \mathrm{m}$ while ground magnetic data located five solutions either on a positive magnetic anomaly pole or negative magnetic anomaly pole with a depth range of $1090\ \mathrm{m}$ to $3973\ \mathrm{m}$. Spectral analysis of ground magnetic data estimated the curie point isotherm depth at $2970\ \mathrm{m}$ with a curie temperature range of $130\ ℃$ to $680\ ℃$. Joint forward modelling of gravity and magnetic data revealed intrusions within the Earth's subsurface with depth to the top ranging from the shallowest at $739\ \mathrm{m}$ to the deepest at $5811\mathrm{m}$. It was established that areas with high heat flux on the Earth's surface have shallow heat sources while those with low or moderate heat flux have deep heat sources. The densities of the anomaly sources were determined to range between $3.0\ \mathrm{gcm^{-3}}$ and $3.2\ \mathrm{gcm^{-3}}$ while the magnetic susceptibility was zero, implying the intrusions are from the mantle materials or dykes extending from a batholith rock with higher temperatures than their curie temperature. Joint forward modelling of gravity and magnetic data revealed geothermal heat sources with positive gravity anomaly and zero magnetic susceptibility on a high heat flux area. This was located in the western part of the study area along Opuru, Eburru settlement scheme, Oldoinyo Opuru, and towards Lake Elmenteita to the North of the study area. The study imaged a positive gravity anomaly oriented in a North-South direction at the central part of the study area near Eburru forest and Opuru. A Positive gravity anomaly implies that the causative body is an intruding dyke from the

mantle or a batholith rock of mantle origin with a higher density than the host crustal rocks. Magnetic susceptibility of zero implies that the intrusions have a higher temperature that affects the magnetic properties of constituent elements or the presence of hot fluids causing hydrothermal demagnetisation. This study shows that the Eburru area has high-temperature structures within the accessible depth. Geothermal wells should possibly be located vertically above the intrusions with high heat flux on the Earth's surface.

CHAPTER ONE

INTRODUCTION

1.0 Background information

Eburru study area is in Kenya's Rift Valley, approximately 123 km West of Nairobi city, as shown in Figure 1.1. It is to the South of Lake Elmenteita and 8 km Northwest of Lake Naivasha.

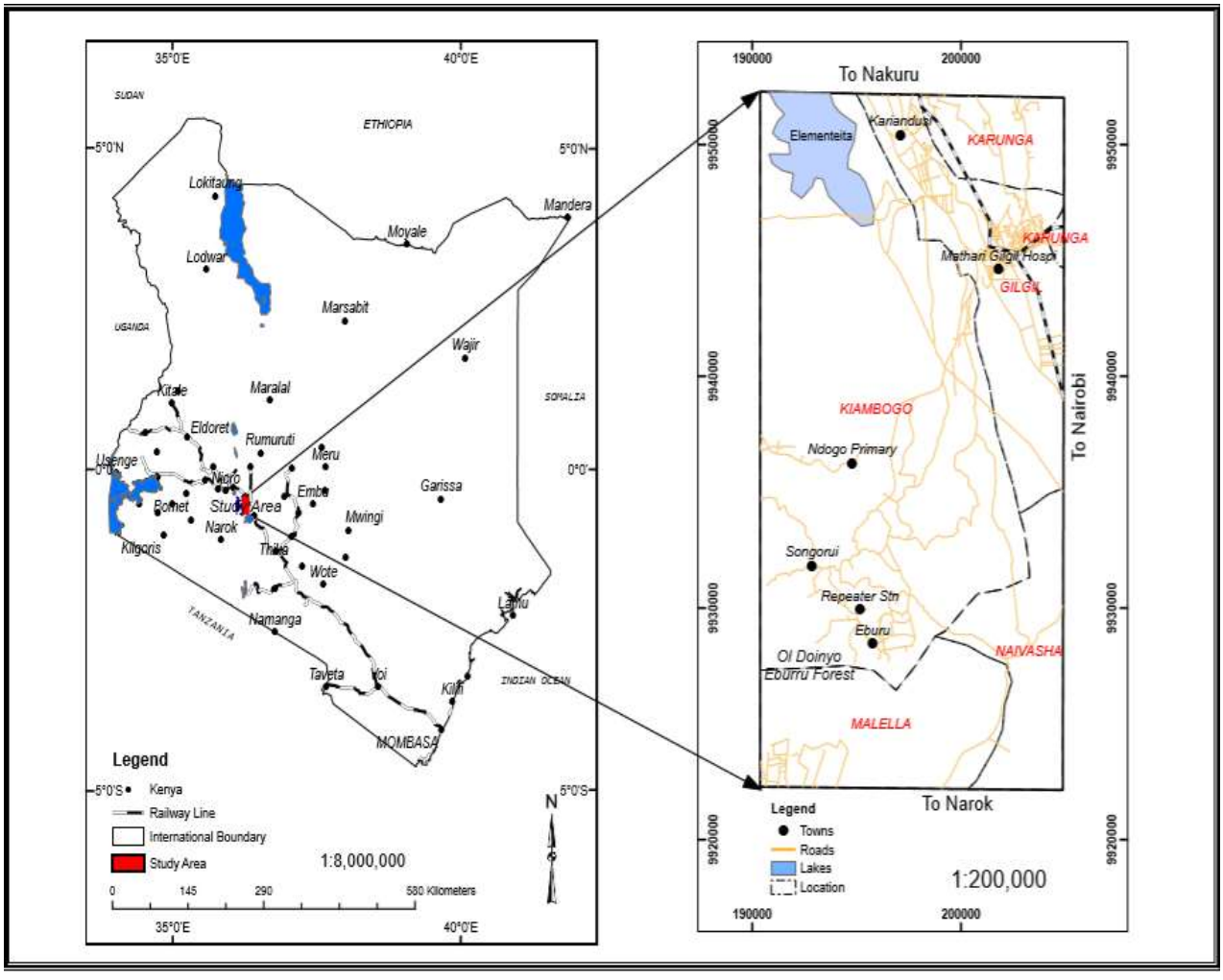

Figure 1.1: Topographical map showing the location of the Eburru study area (Kenya Government, 2005)

It is one of the prospective areas within Kenya's Rift Valley, as shown in Figure 1.2. These areas have shown high potential for geothermal heat source occurrence (Mulaha, 2013). Akira plains separate Olkaria volcano to the South, where geothermal energy has been generated, and Eburru volcano to the North. Eburru area has an East-West trending ridge covering a region of approximately $470\ km^2$ and the highest point at $2850\ m$ above sea level (Kiende & Kandie, 2015). There are hot springs, fumaroles, Sulphur deposits, geothermal grass and steam jets along the recent faults indicating the possibility of geothermal heat sources.

Many geophysical methods can be employed to explore geothermal heat sources (Mariita, 1995; Ndombi, 1981; Simiyu & Keller, 1997). Often, more than one method is used simultaneously in the same survey area to reduce ambiguity arising from the interpretation of results from one method. This is achieved by considering the results of another method. Frequently, the gravity method is employed together with the magnetic method (Mariita, 2011). Therefore, this study employed gravity and magnetic methods alongside the heat flow method to explore geothermal heat sources in the Eburru area and establish their correlation.

Geothermal energy is the natural heat from the Earth's interior in the form of magma which can be used as a renewable energy source. The source of this natural energy is the geothermal heat sources in the Earth. Magma is a hot molten material from the Earth's mantle or melted crustal rocks due to heat transfer from deep hot masses. There is a continuous heat flow from the Earth's interior, which is hot towards the crust, which is cooler due to the temperature gradient. The Earth's crust is made up of tectonic plates with faults and fractures, allowing magma to penetrate and flow to the Earth's surface in the form of a lava flow. But the large part of magma does not reach the surface because it is trapped within the Earth's subsurface in the form of dykes and sills connected to deep hot masses. This possibly forms the geothermal heat sources.

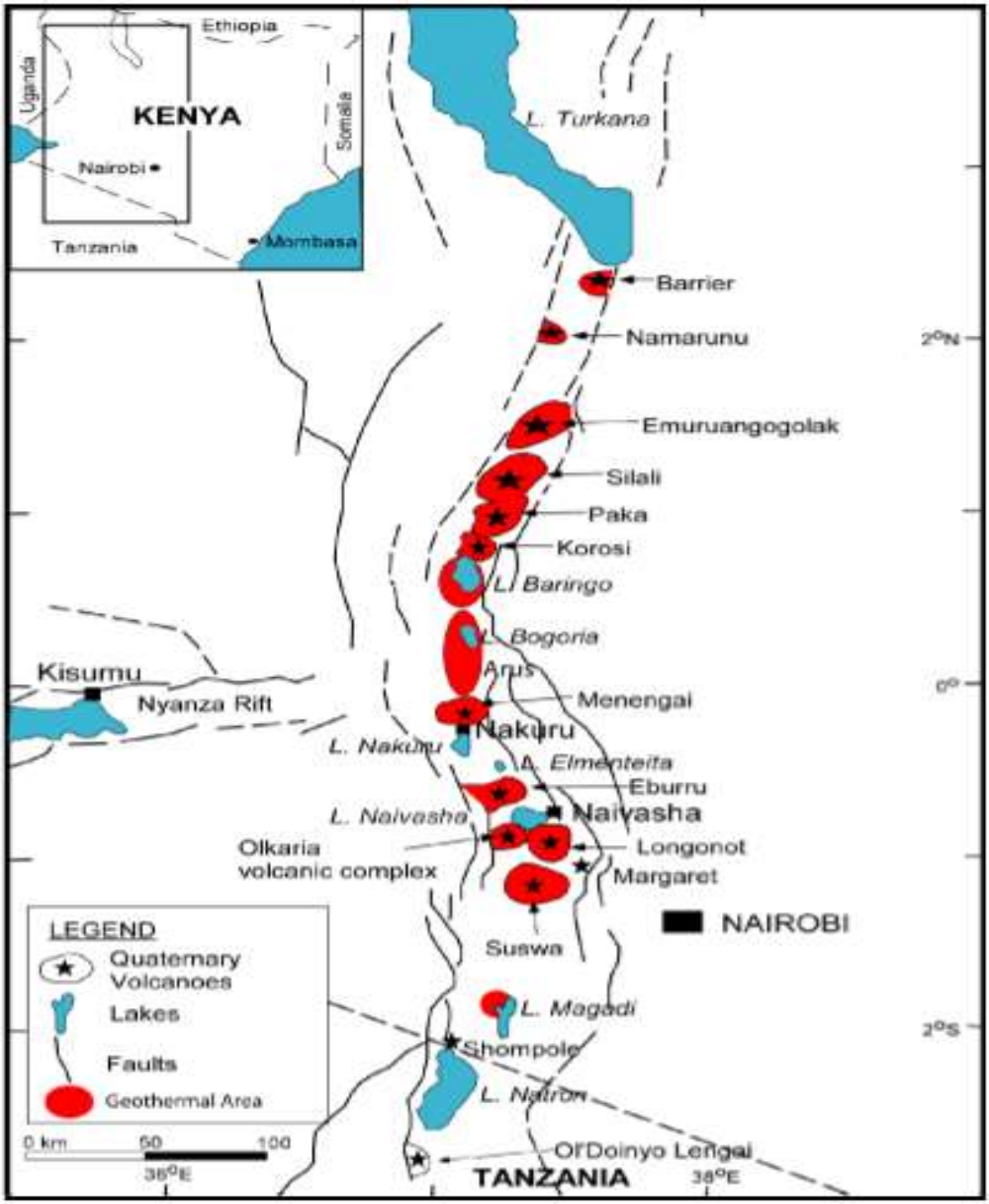

Figure 1.2: Map showing geothermal prospect areas in Kenya (Mwawongo, 2013)

When surface water seeps through the faults and fractured rocks come into contact with the hot magma and nearby heated hot rocks, it gets heated and may come out of the subsurface as a hot spring, geyser, or fumarole if in gaseous form. But when this hot water flows under a layer of impermeable rock, it may get trapped underground and create a geothermal reservoir that can be developed to generate geothermal energy (Manzella, 2017). Therefore, heat source location and characterization are essential in geothermal resource development. The heat flow method revealed areas with elevated geothermal gradient for geothermal heat source characterization. This study applied gravity and magnetic methods to estimate gravity and magnetic field variations within the Earth's subsurface. These geophysical methods located geothermal activities and characterized the permeability structures.

The heat flow method entails the direct acquisition of temperature measurements on the shallow surface of the Earth to determine the geothermal gradient (Xi et al., 2015). Heat varies within the Earth because of conduction due to atomic vibrations and convection, which moves heat by natural circulation of hot and cold masses. Elevated heat flux in a geothermal area can be interpreted to be due to the convection of geothermal fluids and occurs mainly in sedimentary rocks, while in crystalline rock areas, the elevated heat flux is usually due to conduction (Georgsson, 2013). Temperature increases with depth, as observed in mines and boreholes, revealing the presence of heat sources in the interior of the Earth. High local geothermal gradients which are above the average temperature gradient of $0.03\ ℃m^{-1}$ (Mwawongo, 2013) corresponds to elevated local heat fluxes. The possible sources of heat in the Earth's interior include radiogenic heat, core formation, gravitational energy released by thermal contraction, progressive differentiation of the mantle, impacts, and self-compression of the Earth.

Gravity is an indirect method in geothermal exploration that aims at imaging the density of the underlying host rocks within the Earth's subsurface that could be related to the heat source (Georgsson, 2009). The basic principle in gravity surveying is the changes in the Earth's gravitational field arising from the differences in the density of rocks within the

subsurface. A region within the subsurface with a different density from the surrounding masses results in a perturbed gravitational field called a gravity anomaly (Kearey, Brooks, & Hill, 2002). Gravity anomaly can either be positive or negative. Volcanic centres, where geothermal activity is common, are signs of cooling magma or hot rock beneath these areas, as evidenced by the recent volcanic soils, volcanic domes, and hydrothermal activities occurring in the form of fumaroles and hot springs (Mariita, 2011). These volcanic centres are usually mapped with gravity highs. Gravity studies in volcanic areas have effectively demonstrated that this method provides good evidence of shallow subsurface density variation associated with the structural and magmatic history of a volcano (Ndombi, 1981). Gravity highs correspond to volcanic centres, faults, and geothermal heat sources, as evidenced in Olkaria Domes and Suswa geothermal centres which are located on the crest of a gravity high (Mariita, 2011). Therefore, a gravity survey was conducted in the study area to identify and determine the depth of magmatic heat sources.

The purpose of a magnetic survey is to examine the Earth's subsurface geology on the foundations of the changes in the Earth's magnetic field due to the magnetic properties of the underlying masses (Telford, Geldart, & Sheriff, 1990). The magnetic susceptibility of rocks within the subsurface varies depending on the magnetic types of masses present and the Earth's underground activities, such as hydrothermal demagnetization. Dykes, faults, basic intrusions, metamorphic basement, magnetic ores, and lava flow cause an increase in magnetic susceptibility hence magnetic high amplitude. In a geothermal environment, increased temperatures reduce magnetic susceptibility; thus, hydrothermal demagnetization results in low magnetic anomaly amplitudes (Mariita, 2011). Therefore, Magnetic surveys can locate demagnetized masses because of thermal variations, and they can provide complementary structural information about the surveyed region. (Pipan, 2009) concluded that high-resolution aeromagnetic (HRAM) investigations have a resolution in the subnanotesla scale. Magnetic studies are not employed for magmatic rocks but can also be used to map intrasedimentary faults with increased magnetite concentrations that result in minor anomalies. The magnetic content of a mass within the

Earth's subsurface and the temperature at which magnetism disappears depend upon the mass's magnetic composition such as magnetite and hematite (Rivas, 2013). Demagnetized rocks suggest the presence of a hot mass within the Earth's crust, while high susceptibility suggests the presence of dykes, faults, basic intrusions, magnetic ore bodies, and lava flows. Also, hydrothermal fluids circulation results in the destruction of magnetic content in an underground mass, thus causing decreased magnetic susceptibility (Ochieng, 2013). Therefore, this study employed the magnetic method as it can characterize most activities associated with a geothermal heat sources.

Heat flow, gravity, and magnetic techniques have been widely used in geothermal exploration to map and characterize the structures of the possible heat sources and show thermal distribution on the surface of the study area (Mariita, 2011; Mwawongo, 2013). The heat flow technique located sites with high heat flux which possibly indicated a shallow heat source or a good medium of heat transfer from the interior of the Earth. Gravity and magnetic techniques are potential field methods that determined the physical properties of host rocks (for example, gravity figured out changes in density while magnetic checked changes in magnetization) that were used to locate the heat sources. These methods located hidden intrusives, faults, and buried dykes and estimated their depths.

1.1 Geology of Eburru study area

Eburru study area has a topographic rim of the crater formed of trachytes, pantellerites, pyroclastic deposits, and basaltic units (Ronoh, 2015). The area has several eruption centres with some entirely or almost completely buried by later pyroclastics as shown in Figure 1.3. It is characterized by dykes, major faults, eruption fissures, ignimbrites, phonolites, phonolitic trachytes, tuffs, agglomerates and acid lava (Woodhall & Clarke, 1988). Also, volcanic soil and diatomite deposits dominate the Eburru area area with trona impregnated silts bordering Lake Elmenteita (Thompson & Dodson, 1963). Eburru structures are mainly in a North-South direction with few oriented in a Northwest-

Southeast direction (Mwawongo, 2005). The study of rocks in the area shows that rhyolite, trachyte, and basalt are the commonest (Mwawongo, 2005).

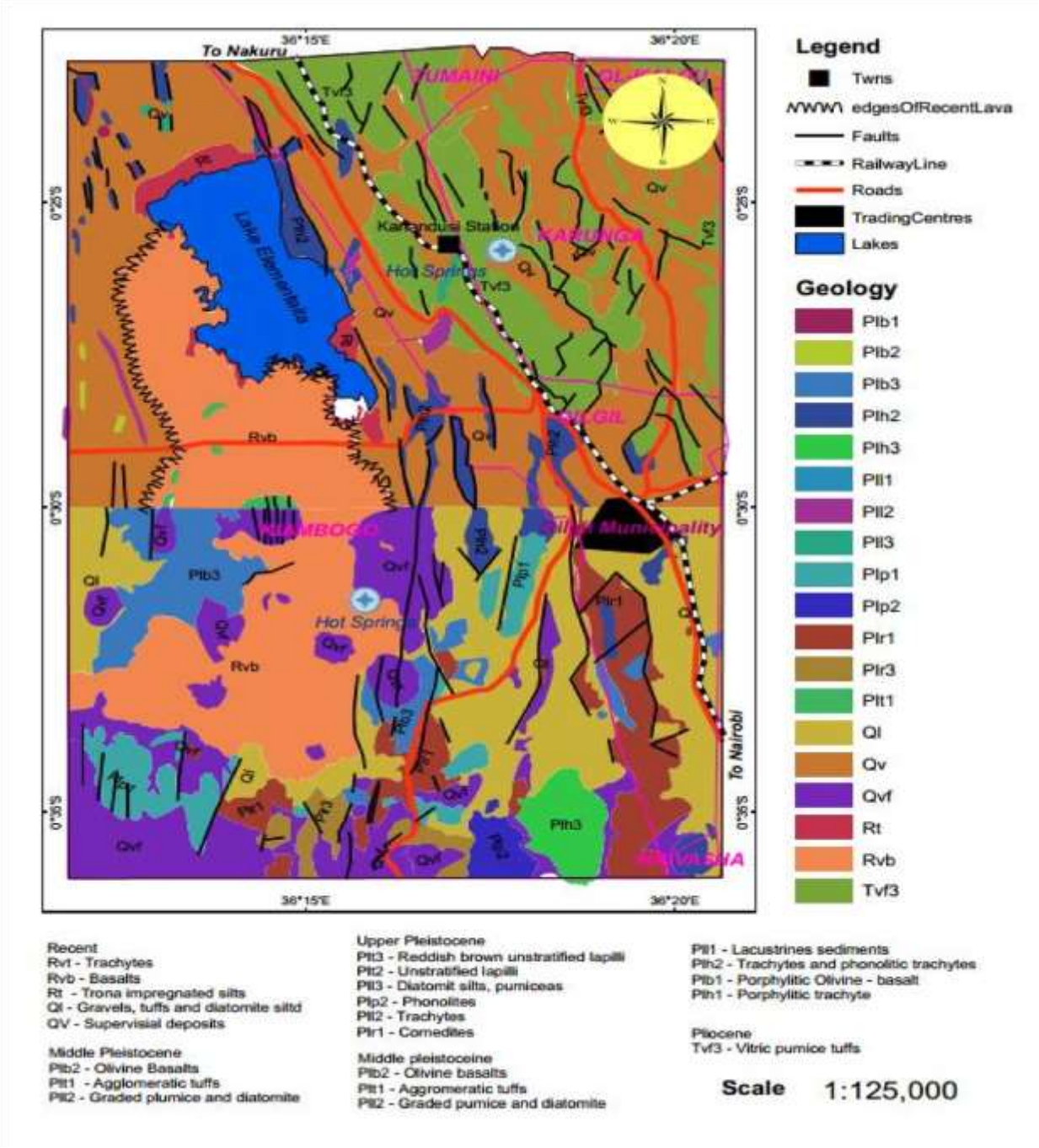

Figure 1.3: Map showing the geology of Eburru study area (Woodhall & Clarke, 1988)

Figure 1.3 displays and summarizes the geology of the Eburru area. The area has trachytes, pantellerites and pyroclastic rock types, and it is associated with a basaltic field just to the North towards Elmenteita basaltic area (Beltran & Manuel, 2003). There is the presence of several faults and fissures, which are very important for controlling recharge and fluid movement within the geothermal system. There is also the presence of altered grounds, hot grounds, active fumaroles area, geothermal grass cover, and hydrothermal deposits in the area. There is a hydrogen sulphide smell at active fissures, indicating the presence of intruding magma within the subsurface in the area (Kiende & Kandie, 2015).

1.2 Previous exploration studies in the Eburru area

Previously, some geophysical studies have been carried out in the Eburru volcanic complex covering an area of approximately $6\ km^2$ (Mwarania, 2014). These studies mainly covered areas within the Eburru caldera due to massive geothermal surface manifestations (Mwawongo, 2005). The temperature of the steam and fumaroles in this area was approximately 90 ℃ (Jica, 1980). Six exploration wells were drilled in the area to an average depth of 2500 m between 1989 and 1991 by the Kenya Power Company for GOK. Preliminary results indicated that the area has temperatures above 300 ℃ at this depth. Out of the six wells drilled, only one generated steam pressure that led to the development of a binary power plant that produces 2.5 MW. The results from the Monte Carlo method that was carried out indicated that the resource should generate a minimum of 11 MW for a period of thirty to fifty years (Mwarania, 2014). The power potential for this well was assessed and approximated to be 25 MW (Omenda et al., 2000), and the power potential for the Eburru caldera was estimated at 50 MW (Mulaha, 2013); hence there was a need for more detailed studies.

The conceptual model for the area was proposed and indicated an up-flow region concentrated within the caldera with a recharge zone from all directions of the surrounding regions (Mwarania, 2014). TEM studies indicated a relatively low resistivity zone at near-surface depths, which could be characteristic of low-temperature rocks (Mwarania, 2014). There was a high resistivity zone beneath this low resistivity zone at the crater, interpreted

as a geothermal resource where the wells should be drilled to tap the heat (Mwarania, 2014). MT soundings at 3000 m.b.s.l imaged a low resistivity anomaly oriented in a Northeast – Southwest direction (Mwarania, 2014). The lowest resistivity in the anomaly was interpreted to be a possible heat source due to intrusive masses from the Earth's mantle. Gravity results for the area analysed using integrated gradient interpretation techniques for edge detection showed the subsurface structures and their corresponding trend (Maithya & Fujimitsu, 2018). Also, it imaged several faults that were assessed with the located faults from the subsurface geology of the area (Maithya & Fujimitsu, 2018). This was interpreted to be possible heat sources.

(Mwangi, 2012) processed and analysed MT and TEM data covering Eburru crater using an ssmt 2000 software from phoenix geophysics. Combined 1D Inversion of TEM and MT data revealed three major resistivity zones. An upper layer revealed a high resistive zone that was interpreted to be unaltered rocks at the surface. There was a low resistive zone which was an indicator of an altered layer and an intermediate zone an indication of a conductive layer which was interpreted to be a smectite zeolite zone (Mwangi, 2012). These MT results revealed a large magma intrusion at the centre of the Eburru crater (Mwangi, 2018). It showed that well 1, which is currently producing 2.5 MW of electricity could be tapping the heat from this intrusion (Mwangi, 2018). (Maithya & Fujimitsu, 2019) used 107 MT soundings in Eburru to map out possible heat sources and fluid flow pathways for the geothermal system. The inverted resistivity information matched the MT data for the area (Maithya & Fujimitsu, 2019). Three dimensional MT models were done and revealed a high conductive layer beneath a high resistivity layer on top. Beneath these layers was a high resistive zone. Resistivity profiles were extracted from these models for resistive structure characterization. Analysis from the profiles indicated a low resistive region at 1km and 4km and was interpreted as geothermal fluid path ways. Comparison of 2D and 3D resistivity models revealed similar results with slight variation in deep 3D models (Maithya & Fujimitsu, 2019).

Therefore, this study covered a larger area for better imaging of deep heat structures using potential field methods. The area covered by this study includes the Eburru crater, Badlands, Gilgil, and Lake Elmenteita in the North of the study area, as shown in Figure 1.1. This study employed heat flow, gravity, magnetic and spectral analysis of ground magnetic data geophysical methods to compare and correlate the outcomes. The heat flow method displayed variation of heat on the Earth's surface. Gravity and magnetic methods imaged subsurface intrusions, probably tapping heat from deep hot masses using Euler deconvolution. Spectral analysis of ground magnetic data was employed in this study to estimate the curie isotherm depth for the area. This was used to show an average depth of hot masses. The joint forward modelling of gravity and magnetic data was done for intrusions imaging and characterization in this area.

1.3 Statement of the problem

Eburru region is one of the geothermal prospect areas in Kenya's Rift Valley, as shown in Figure 1.2 (Mulaha, 2013). The area is characterized by faults and fractures, which probably influence the flow of geothermal fluids within the Earth's subsurface. It has several fumaroles, geysers, Sulphur deposits, hot grounds, geothermal grass, hot springs, and volcanic craters, indicating various activities from the Earth's mantle towards the subsurface, which are usually observed in geothermal resource areas. Previously, some exploration work had been done mainly within the Eburru crater. Six wells with an average depth of 2500 m were drilled within the Eburru crater between 1989 and 1991 by the Kenya Power Company for GOK (Mwawongo, 2005). Only one well out of the six drilled wells was productive, generating 5 MW of electricity. This shows the possibility of a geothermal heat source in the area; hence it was necessary to conduct a detailed study using heat flow, gravity, and magnetic geophysical methods to map and characterize the heat source structures for possible higher geothermal energy production. In order to image the deep structures and estimate the depth of the possible heat sources, there was a need to cover a more extensive study area. This study employed heat flux from heat flow measurements, Euler deconvolution of gravity and magnetic data, spectral analysis of

ground magnetic data, and joint forward modelling of gravity and magnetic data since these techniques have not been attempted in the study area. These geophysical methods are commonly used to study the possibility of a geothermal heat source occurrence; hence there was a need to compare and correlate the outcomes. The heat flow method was embraced as it involves direct temperature measurement, a key parameter in heat source characterization. Ground gravity and magnetic methods are potential field techniques employed due to their ability to image deeper structures primarily associated with heat sources. Spectral analysis of ground magnetic data was employed to determine the curie point isotherm depth which was integrated with the results from Euler deconvolution, heat flux and joint forward modelling.

1.4 Justification of the study.

This study imaged the Earth's subsurface and provided information on the possible occurrence of geothermal heat sources. It was done by integrating heat flow measurements, gravity, and magnetic methods to characterize the geothermal heat sources better. The obtained results from the three methods were compared well. The relationship was explained, leading to a better conclusion. These geophysical methods are cheaper and easier to carry out than drilling, which is expensive and involving. Therefore, it was necessary to apply the three geophysical methods for better imaging of the subsurface and the correlation of their outcomes. Characterization of a geothermal heat source in this area can lead to the development of the resource to provide clean, renewable energy to the national grid. This will solve the problem of energy shortages in the industries which are crucial to the development of the Country. Further, the world is moving from non-renewable environmental pollutant sources of energy toward clean, renewable sources of energy, which is in line with the global goals of the energy sector. Geothermal energy is green energy that does not release carbon dioxide into the atmosphere (Kiruja, 2011). The development of this geothermal energy will provide an alternative energy source to burning fossil fuels, which pollute the environment and affect the ozone layer. The discovery and development of this geothermal resource will create employment

opportunities for those working at the geothermal power plant and open up the Eburru area for investment opportunities. The generation of this geothermal energy will reduce electric power prices, which subsequently reduces the prices of goods and services in the Country. Reduced cost of goods and services will reduce the cost of living and thus improve people's living standards. The geothermal resource can also be utilized directly in heating greenhouses, bathing, and swimming in a spa. This can lead to tourism attraction, a key sector driving the Kenyan economy. This will all aid in achieving Kenya's vision of 2030.

1.5 Objectives

1.5.1 General objective

The main objective of this study was to map and characterize the structures of geothermal heat sources in the Eburru area, Nakuru County, Kenya, using heat flow, gravity, and magnetic geophysical methods.

1.5.2 Specific objectives

The specific objectives of this study were to:

1. Identify high geothermal heat flux areas in the Eburru study area from shallow hole temperature measurements data.
2. Delineate gravity and magnetic anomalies in the Eburru study area from ground gravity and magnetic data.
3. Estimate the curie point isotherm depth in the Eburru study area.
4. Model the causative bodies using gravity and magnetic data to characterize the geothermal heat source.

1.6 Research questions

1. Do high heat flux areas imply an accessible geothermal heat source?
2. How do gravity and magnetic anomalies correlate to high and low heat flux?

3. Can curie point isotherm depth be used to estimate the heat source temperature and its accessibility?
4. What is the correlation between density and magnetic susceptibility of masses in a geothermal heat source area?

CHAPTER TWO

LITERATURE REVIEW

2.0 Introduction

The geophysical techniques employed in this study have been applied widely in the mapping and characterization of geothermal heat sources. This chapter highlights regions where the techniques have been used successfully to explore the Earth's subsurface. The chapter also explains the scientific theory of these geophysical techniques in geothermal heat source studies.

2.1 Previous studies

This section discusses previous applications of heat flow, gravity, and magnetic geophysical methods for mapping and characterization of geothermal heat sources in other potential areas.

A microgravity survey covering 101 gravity stations was carried out at the Bacman geothermal field and its environs in the Philippines to explain and characterize the region around the geothermal reservoir (Monasterial, 2015). Gravity reductions were made to the observed gravity data by Gravos, Gnet, Terra and Terrb computer software which resulted in a Bouguer anomaly. Parasnis concept was used to figure out the standard reduction density (Parasnis, 1952). The data were further processed by removing the regional trend caused by deep underlying rocks to obtain the residual anomaly. Gravity highs in the central part of the area occurred at the Bacman fault zone. They were interpreted to be dense, intrusive bodies, such as diorite, which occurs below this region on the foundations of core samples. Gravity lows in the Southeast of the study area were sedimentary formations. The ones to the Northern parts of the study area were interpreted to be collapse features. The depth of the causative body was determined to be approximately 900 m in depth (Monasterial, 2015).

A gravity study was done at Menengai geothermal field to image the heat sources. The geothermal field showed promising results of a geothermal resource, but the wells drilled did not produce (Kanda & Fujimitsu, 2018). The complexity of area geology prompted the study to figure out the alignment of heat source structures. A total of 1610 gravity stations were covered in an area of approximately 880 km^2. The gravity high observed in the Bouguer anomaly map was interpreted as magma intruding within the Earth's subsurface. This was confirmed by the presence of young volcanic rocks and fumaroles at the same gravity points. Gravity lows were imaged along Rongai plain and Solai graben interpreted to be due to volcanic sediment deposits (Kanda & Fujimitsu, 2018).

(Moghaddam, Oskooi, Mirzaei, & Jouneghani, 2012) conducted ground magnetic survey in the Mahallat region in Iran's centre for geothermal energy investigation and exploration program managed by Arak and Tehran universities. The magnetic survey was conducted for reconnaissance of a possible geothermal heat source in the area. Magnetic data were collected from approximately 4000 observation points covering a ground area of about 250 Km^2. The study was prompted by geothermal indicators in the area such as hot springs, hydrothermal deposits, temperature variations and recent volcanic soils. The observed magnetic field of the Mahallat geothermal study area was corrected for diurnal variations and geomagnetic corrections. These corrections generated magnetic anomalies. The Euler method was used to process the data before it was subjected to three-dimensional modelling. The resulting models were analyzed and revealed that the deep source of heat alterations had generated a wide magnetic anomaly within the depths of approximately 1200 m beneath the Earth's surface. According to the geology of the study area, it appeared that hot igneous rocks create the confer heater for the geothermal complex of the study area. It was also found that the faults and cracks in the area acted as underground conduits

through which water flows down to the hot igneous rocks, gets heated and returns to the surface in form of hot springs in the area.

(Schermerhorn et al., 2017) carried out a geothermal investigation of Mount Baker hot springs using magnetic and gravity survey techniques simultaneously. This study aimed to gather geological, magnetic, and gravity information to help understand the spatial variations in the Earth's subsurface structures and geology that could explain the heat source for a geothermal reservoir in the area. A total of 93 km of line magnetic information was recorded. Gravity data was observed at 495 gravity points covering a surface area of approximately 150 km^2. Magnetic and gravity reductions were applied to magnetic and gravity data, respectively. This resulted in magnetic and gravity anomalies further subjected to Oasis Montaj computer software for gridding and filtering. The data was then transferred to the GM-SYS computer software for 2D modelling. Gravity results showed horizontal changes in the density of underlying rocks used to reveal subsurface geology and structure information (Santos & Rivas, 2009). Gravity highs covering a distance of about 9.3 km along with Baker Lake's western show and exactly east of Baker Lake, about 9 km in length, were imaged. The magnetic susceptibility model results revealed a lengthy region vertical in the direction of high magnetization that is oriented in a North-Northeast direction. The Northern end of this high magnetization area was found underneath the hot springs and proceeds to about 1.7 km to the South of the Baker hot springs. The top of the high magnetization area lies less than a few hundred meters below the surface and extends to about 1 km depth at its deepest point. The area showing a rise in magnetic susceptibility was interpreted as a mafic intrusion that penetrated underneath and to the south of the hot springs. The edges of this intrusive body could probably make vertical, permeable conduits for the ascending heated fluids that sustain the hot springs in the area.

Gravity and aeromagnetic data in Xiongxian geothermal field were analysed, and interpretation was done simultaneously using the Euler deconvolution method (Hong, Jianbao, Hui, Pengfei, & Sinopec Geophysical Research Institute, 2017). This was done to assess the area geology for geothermal heat source characterization. From gravity analysis, the fault structure of Niutuozhen was imaged. Magnetic analysis imaged magnetic zones of igneous rock concentration. These are in the Niutuozhen fault and the Xiongxian fault. Faults provide boundary controls of underground fluids together with secondary fractures within the system (Hong et al., 2017). The location of igneous rocks is important as it images the regional heat source which can be transferred to the Earth's subsurface.

Shallow temperature surveys for geothermal exploration in the Great Basin, USA, and shallow aquifer heat loss estimation were conducted (Coolbaugh, Sladek, Zehner, & Kratt, 2014). Shallow temperature measurements of about $1-2$ metres revealed an average of 9 MWt heat loss at Nevada. This was taken to be a minimum estimate because several anomalies are within areas of shallow cold water, which interferes with the temperatures. These anomalies were caused by less deep thermal fluid from plumes.

Determination of curie point depth (CPD) for the Guangxi area in China was done to explain the lithospheric magnetic structure, thermal activity and seismicity. The power spectrum analysis was done using the aeromagnetic anomaly data to determine the curie point depth (CPD). The results indicated curie point depth in Guangxi varies from 19 km to 40 km. It was noted from the outcomes that there is a weak inverse correlation between the curie point depth and heat flow, but the relation between them is nonlinear (Zhi et al., 2018). This means that the deeper the curie point depth, the lower the heat flow and vice versa. It was also revealed that the distribution of faults and igneous rocks influences the variation of curie point depth.

Therefore, the three geophysical methods can be used to map and characterize the geothermal heat structures in the Eburru study area. The methods have been used in other areas to map and characterize geothermal heat sources. The heat flow method is a highly effective and efficient geophysical method as it involves the measurement of temperature that directly determines the geothermal activity (Georgsson, 2013). Gravity and magnetic geophysical techniques have been widely used for geothermal exploration (Chen & Zhuozhou, 2019). The methods can locate intrusive rocks in the form of dykes associated with the heat source (Shah et al., 2015). The gravity method can also map faults and alterations caused by thermal effects. The magnetic method can locate regions of reduced magnetization, which can be interpreted to be caused by hydrothermal activities. Gravity and magnetic methods explore the physical parameters of the host rock that can be used to locate and characterize the heat source (Georgsson, 2009).

2.2 Theoretical review

This section explains the principles and theories behind the methods employed in this study. The section explains and describes the fundamental concepts of the methods and processing procedures employed.

2.2.1 Heat flow method

The heat flow method entails heat loss measurements on the Earth's surface to map anomalous areas. It is based on temperature measurements with depth which is then used to determine the heat flux of the study area. Heat flux values are plotted to generate a thermal contour map showing the heat loss distribution in the study area. The thermal contour map shows high and low heat flux areas within the study area.

Heat flow measurement involves the direct acquisition of temperature in the shallow subsurface of the Earth. Heat varies within the Earth because of conduction due to

atomic vibrations and convection, which moves heat by natural circulation of hot and cold masses. Elevated heat flow in a geothermal resource area can be interpreted to be due to the convection of geothermal fluids and occurs mainly in crystalline rocks, while in sedimentary areas, the elevated heat flow is usually due to conduction (Georgsson, 2013). Temperature increases with depth, as noticed in mines and boreholes, showing that there are heat sources in the interior of the Earth. An elevated temperature gradient probably indicates a shallow heat source and a good heat transfer mechanism within the area's subsurface (Mwawongo, 2013). Also, the elevated temperature gradient could be due to the thinning of the Earth's crust because of continental rifting or the presence of radioactive elements on the near-surface of the Earth. The possible sources of heat in the Earth's interior include radiogenic heat, core formation, gravitational energy released by thermal contraction, progressive differentiation of the mantle, impacts, and self-compression of the Earth (Parasnis, 1986).

In a shallow hole shown in Figure 2.1, thermal gradient M gives a variation of temperature with depth as expressed in Equation 2.1 (Nurhandoko et al., 2013).

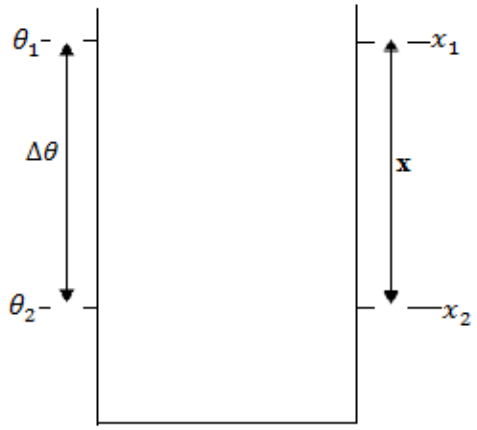

Figure 2.1: Shallow hole for temperature measurement

$$M = \frac{\theta_2 - \theta_1}{x_2 - x_1} = \frac{\Delta\theta}{x} \quad 2.1$$

Where θ_2 is the temperature at x_2, θ_1 is the temperature at x_1 and $\Delta\theta$ is the change in temperature between x_2 and x_1 as shown in Figure 2.1. x is the distance between the points x_2 and x_1 of a shallow hole.

Equation 2.2 gives an expression for the rate of heat flow

$$\frac{Q}{t} = kAM \quad 2.2$$

Where Q is the quantity of heat, t is the time, k is the thermal conductivity, and A is the area.

Equation 2.3 expresses heat flux q, which is the rate of heat flow per unit area. It is derived from Fourier's first law, which shows that practical observation of heat flow is linearly proportional to the thermal gradient (Nurhandoko et al., 2013).

$$q = kM \quad 2.3$$

Thermal conductivity k for the study area is 2 $Wm^{-1}°C^{-1}$ (Hochstein & Kagiri, 1997; Mburu, 2006; Mwawasi, 2012; Sippel et al., 2017). Thermal conductivity k is the ease at which solid masses within the Earth's crust transfer heat energy (Batir, Blackwell, & Richards, 2015). It is determined by a divided bar experiment in which heat supplied by the needle probe is measured as it travels through the sample (Batir et al., 2015). With a known geothermal gradient, thermal conductivity can be determined using equation 2.3. High local thermal gradient, which is above the normal temperature gradient of 0.03 $°Cm^{-1}$ (Mwawongo, 2013) corresponds to elevated local heat fluxes and indicates a possibility of occurrence of a shallow heat source.

2.2.2 Gravity method

The gravity method is a geophysical technique that involves the measurement of the Earth's gravitational field. The gravitational field variation in the Earth is recorded for imaging the underlying structures within the subsurface (Kearey et al., 2002). It is preferred because of its non-invasive nature, relatively cheap, no energy needed to be put to the ground to acquire data, and well suited in a populated setting (Dickerson, 2004).

2.2.2.1 Theory of gravity method

In the gravity method, the study area is investigated based on changes in the Earth's gravitational field resulting from changes in the density of present rocks within the subsurface. The basic principle is locating and describing the causative body with a different density from the host rock that perturbs the Earth's gravitational field resulting in gravity anomalies. Earth's gravitational field varies from one point to another. This is due to the lithology of the underlying masses, where the density changes both laterally and vertically. The gravity method measures the gravitational field variation and determines the possible underlying densities of rocks causing the variation. This results in imaging the Earth's subsurface in terms of density distribution. The gravity method is based on Newton's law of universal gravitation and Newton's second law of motion. Newton's law of universal gravitation states that two masses in the universe attract each other with force directly proportional to the product of their masses and inversely proportional to the square of the distance between them (Kearey et al., 2002). Figure 2.2 displays the mass m on the Earth's surface to illustrate Newton's law of universal gravitation.

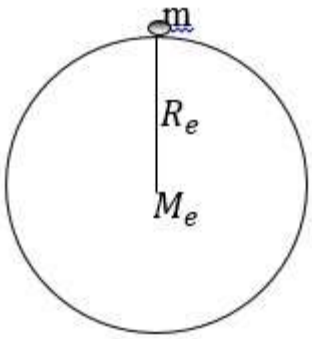

Figure 2.2: Mass m on Earth's surface

Equation 2.4 is derived from Newton's law of universal gravitation.

$$F \propto \frac{mM_e}{R_e^2}$$

$$F = \frac{GmM_e}{R_e^2} \qquad 2.4$$

Newton's second law of motion states that the product of mass and acceleration of a body equals the force acting on that body, as expressed in equation 2.5.

$$F = ma \qquad 2.5$$

Acceleration is the gravitational field's vertical component; therefore, equation 2.5 can be rewritten as equation 2.6.

$$F = mg_z \qquad 2.6$$

Equating equations 2.4 and 2.6, then,

$$F = \frac{GmM_e}{R_e^2} = mg_z$$

This means that the vertical component of gravity g_z is given by equation 2.7.

$$g_z = \frac{GM_e}{R_e^2} \quad 2.7$$

Gravitational potential V is the work done against the gravitational force for a unit mass to leave the gravitational field of a body, as expressed in equation 2.8.

$$w = Fdr \quad 2.8$$

Equation 2.9 is determined by substituting equation 2.4 in equation 2.8.

$$W = \frac{GMm}{r^2}\, dr \quad 2.9$$

Integrating equation 2.9, as shown in equation 2.10, gives the expression for gravitational potential in equation 2.11 (Kearey et al., 2002).

$$\frac{W}{m} = \int \frac{GM}{r^2}\, dr \quad 2.10$$

$$V = -\frac{GM}{r} = \text{Gravitational potential} \quad 2.11$$

2.2.2.2 Gravity data corrections

Gravity data corrections entail processing raw gravity data to obtain gravity anomalies. It is necessary because it corrects the effects on the gravitational field, which do not arise from the underlying structures in the Earth's crust. The result is a gravity anomaly that is either positive or negative. A positive gravity anomaly is a gravity high which indicates a dense underlying body, while a negative gravity anomaly is a gravity low which implies a less dense underlying body. After gravity reduction, the

outcome reveals only the effect on the gravitational field caused by the density of underlying structures within the Earth's subsurface which are of economic interest (Lowrie, 2007). The following corrections are done to gravity data.

i. Instrumental drift correction

This is done because the gravimeter reads different values at the same station at different times. This is because of the gravitational effect of the sun and the moon, attraction due to tides, expansion, contraction and creeping of the spring. The instrumental drift is addressed by repeating the measurements at the base station at the beginning and the end of any day data acquisition. The drift curve is plotted from base station readings, and consecutive plotted points are joined by a straight line, as shown in Figure 2.3. The instrumental correction of the gravity stations is done by checking the drift value when the reading was taken. It is added to the observed value if the drift is below the horizontal line and subtracted if it is above the horizontal line (Kearey et al., 2002).

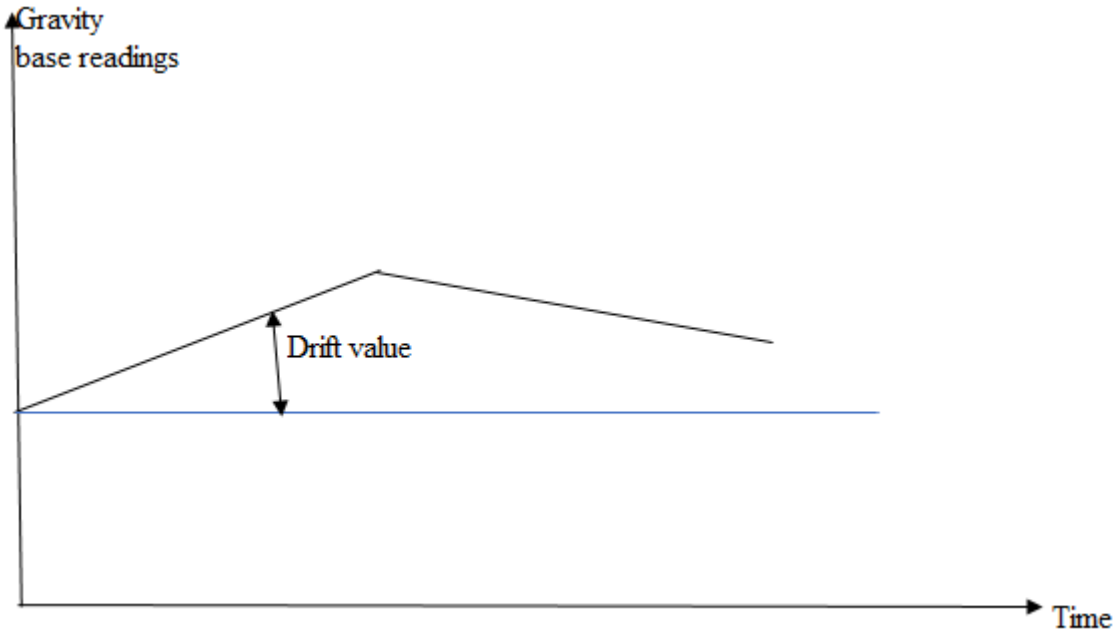

Figure 2.3: Instrumental drift graph

$$\text{Corrected gravity value} = \text{Observed gravity value} \mp \text{Drift value} \qquad 2.12$$

ii. Latitude correction

The gravitational field varies between the latitudes of the Earth. This is because the Earth is not spherical and the angular velocity of a point on the Earth's surface decreases from the equator toward the poles. Angular velocity is maximum at the equator and decreases towards the poles. The latitude correction reduces the observed reading to the geoid to easily compare gravity values between the stations. It accounts for the Earth's elliptical shape and rotation. The Latitude correction is given by Clairaut's formula (Kearey et al., 2002) expressed in equation 2.13.

$$LC = 978032.68(1 + 0.005278895\sin^2\theta + 0.000023462\sin^4\theta)\ \text{mGals} \qquad 2.13$$

Where θ is Latitude. Latitude correction gives the predicted value of gravity at sea level at any point on the Earth's surface. It is corrected by subtracting it from the observed gravity reading.

iii. Free air correction (FAC)

Gravity is a function of mass, and as the distance from the centre of mass increases, gravity decreases. Therefore, gravity decreases as height increases. Free Air Correction is applied by addition to the observed gravity value to account for the decrease. FAC takes into account only the presence of air between the observation point and the geoid (Lowrie, 2007). Gravity at a point on the Earth's surface is given by equation 2.14, assuming the Earth is spherical.

$$g = \frac{GM_e}{R_e^2} \tag{2.14}$$

The rate of gravity decrease with height is obtained by differentiating equation 2.14 and substituting the constants, as shown in equation 2.15.

$$\frac{\partial g}{\partial R_e} = -2\frac{GM_e}{R_e^3} = -2\frac{g}{R_e} = -0.3086 \text{ mGal/m} \tag{2.15}$$

To correct a point with a height h above the geoid, Free Air Correction is given by equation 2.16, whereby its magnitude should be added to the observed gravity. The negative sign in equation 2.16 explains the reduction of gravity due to height.

$$FAC = -0.3086h \text{ mGals} \tag{2.16}$$

iv. Bouguer correction (BC)

FAC assumes no mass between the observation point and the geoid, which is not the case. There could be mass between the observation point and the geoid. Bouguer correction accounts for the presence of these masses. The BC takes into consideration this outcome by taking the rock layer below the observation point to an indefinitely large flat material of height equivalent to the elevation of the observation point above sea level. These masses increase the gravity value observed at a point hence corrected by taking it away from the observed gravity value (Kearey et al., 2002). It is expressed by equation 2.17, where G is Earth's universal gravitational constant, ρ is the average density of crustal rocks, and h is the elevation of observation points above sea level.

$$BC = 2\pi G\rho h = 0.1119h \text{ mgals} \quad 2.17$$

v. Terrain correction (TC)

The Bouguer correction assumes that the terrain near observation points does not have altitude variations (Parasnis, 1986). It assumes a horizontal slab which is not usually the case. There can be a hill or a valley close to the observation point, which causes a decrease in the gravity value recorded. A hill applies an upward attraction around the observation point, reducing gravity, and this effect is restored by adding the TC value. A valley was assumed to contain mass during BC correction, which was removed and must be restored by adding TC values. TC is based on a hammer chart which is divided into several sections. The hammer chart is laid on a topographic map with its centre on the observation point. This is used to determine the average elevation n of each section. Then the expression in equation 2.18 is used to determine TC values (Kearey et al., 2002).

$$TC = G\rho\theta\left\{\sqrt{(r_1^2 + n^2)} - \sqrt{(r_2^2 + n^2)} + r_2 - r_1\right\} \quad 2.18$$

Where θ is the angle subtended by radius r_1 and radius r_2 enclosing the said section. n is the average elevation of the section under consideration. Terrain correction is applied by adding its values to the observed gravity value.

vi. Complete Bouguer anomaly (CBA)

The Complete Bouguer Anomaly is obtained using equation 2.19.

$$\text{CBA} = \text{Observed value} \pm \text{Drift correction} - \text{LC} + \text{FAC} - \text{BC} + \text{TC} \quad 2.19$$

2.2.3 Magnetic method

The magnetic method is a potential field method that involves measurements of the variation in Earth's magnetic field due to the underlying magnetic properties of the present masses. The variation is used to determine the magnetic anomaly which is compared to the magnetic susceptibility of causative bodies during interpretation that may be of economic interest (Mohamed & Saibi, 2017).

2.2.3.1 Theory of magnetic method

The Earth's magnetic field begins from the Earth's core up to space, where there is a flow of charged particles coming out of the sun (Lowrie, 2007). During the magnetic survey, magnetic anomalies are obtained, which are caused by an underlying resource within the Earth's subsurface. Bodies within the Earth's subsurface produce magnetic anomalies due to their effect on the geomagnetic field. Magnetic anomalies are obtained after applying corrections to the observed magnetic value. A freely hanging magnetic material will rest in the direction of the ambient geomagnetic field at any place on the Earth's surface. This is usually at an angle to the vertical and geographic

North. To portray the magnetic field vector, the geomagnetic elements in Figure 2.4 are used (Kearey et al., 2002).

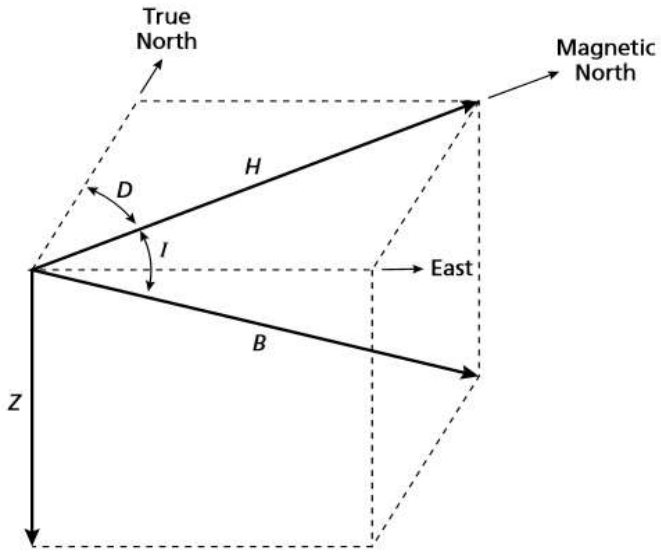

Figure 2.4: The geomagnetic elements

B → Total geomagnetic field.

Z → Vertical geomagnetic component.

H → Horizontal geomagnetic element.

I → The dip of B.

D → Horizontal angle between geographic and magnetic North.

The total geomagnetic field vector B has a vertical geomagnetic component Z and a horizontal geomagnetic component H in the direction of magnetic North. The dip of B is the inclination I of the field, and the horizontal angle between geographic and magnetic North is the declination D (Kearey et al., 2002). The expression gives the force between two magnetic poles in equation 2.20.

$$F = \frac{m_1 m_2}{4\pi\mu r^2} \qquad 2.20$$

Where μ is the magnetic permeability of the medium separating the poles, m_1 and m_2 are the pole strengths and r is the distance separating the poles. The expression gives magnetic flux density B in equation 2.21 (Parasnis, 1986).

$$B = kH \qquad 2.21$$

Where k is the magnetic susceptibility and H is the magnetizing force. Magnetic susceptibility is the ease at which materials within the Earth's crust become magnetized by the Earth's magnetic field (Parasnis, 1986). Therefore, magnetic susceptibility is the parameter used to interpret magnetic data.

2.2.3.2 Magnetic data reduction

The raw magnetic data must be corrected to take away outcomes of magnetic changes except those emerging from the magnetic effects of the rocks within the Earth's subsurface (Telford et al., 1990). After the magnetic data reductions have been done, the magnetic anomaly is obtained, which is interpreted with the study area geology. The following magnetic reductions to the observed magnetic data are diurnal variation correction and geomagnetic correction (Lowrie, 2007).

i. Diurnal variation correction

Diurnal corrections consider the effect of daily variation in the Earth's geomagnetic field. It arises from the variations in the strength of the geomagnetic field during the magnetic data collection at the field. These variations occur because of the ionosphere and solar wind interactions, which is a constant stream of ionized gas with a weak magnetic field (Lowrie, 2007). This correction is done by having a stationary magnetometer at the base station throughout the data collection day. This stationary

magnetometer records magnetic field values at intervals of every five minutes throughout the day. These values determine diurnal correction by evaluating the difference between the magnetic reading at a particular time and the first reading of the day (Kearey et al., 2002). To correct diurnal variation for a station, the time the reading was taken is used to record the corresponding diurnal correction and then subtracted from the observed magnetic reading at the station expressed in equation 2.22.

$$\text{Corrected value} = \text{Observed value} - \text{Diurnal correction} \quad 2.22$$

ii. Geomagnetic correction

Geomagnetic corrections consider the effect of latitude and to a lesser extent, longitude. This correction takes away the effect of the Earth's theoretical magnetic field. The International Geomagnetic Reference Field (IGRF) gives the unperturbed geomagnetic field at any location on the Earth and accounts for secular variation (Telford et al., 1990). Geomagnetic correction is done by subtracting International Geomagnetic Reference Field (IGRF) from the diurnal corrected value to obtain the magnetic anomaly expressed in equation 2.23 (Lowrie, 2007). Magnetic anomaly is due to variations in the magnetic content of the underlying rocks within the Earth's subsurface.

$$\text{Magnetic anomaly} = \text{Diurnal corrected value} - \text{Geomagnetic correction} \quad 2.23$$

2.2.3.3 Spectral analysis of ground magnetic data

Spectral analysis of ground magnetic data is based on Fast Fourier Transform (FFT). Oasis Montaj magmap generates a radially averaged energy spectrum. Fast Fourier Transform (FFT) converts the space domain grid data to the Fourier wavenumber domain (Fedi & Mastro, 2018). Magmap applies filters in the Fourier wavenumber

domain. Mathematically, the Fourier transform of space domain function f(x, y) is defined in equation 2.24:

$$\bar{f}(\mu, v) = \int_{-\infty}^{\infty} \int_{-\infty}^{\infty} f(x, y). e^{-i(\mu x + vy)} \, dxdy \qquad 2.24$$

The space domain function is expressed in equation 2.25:

$$f(x, y) = \frac{1}{4\pi^2} \int_{-\infty}^{\infty} \int_{-\infty}^{\infty} \bar{f}(\mu, v). e^{i(\mu x + vy)} \, d\mu dv \qquad 2.25$$

Where μ and v are wavenumbers in the x and y directions measured in cycles per metre. A given potential field function in the space domain has a single and unique wavenumber domain function and vice versa. The 2D function of energy against wavenumber and direction is called the energy spectrum. Spectra explains the variation of energy as a function of wavenumber. The power spectrum $\left|\bar{f}(\mu, v)\right|^2$ and its total energy E_T are related by the expression in equation 2.26:

$$E_T = \frac{1}{2\pi} \int_{-\infty}^{\infty} \left|\bar{f}(\mu, v)\right|^2 d\mu dv \qquad 2.26$$

Where μ and v are wavenumbers in x and y directions. Geophysical potential data is collected with defined boundaries within the study area, unlike the infinite area assumed in mathematical equations 2.24, 2.25, and 2.26. The study area should be large and radially averaged energy spectrum produced because isotherm depth involves imaging deeper structures. The radially averaged energy spectrum is a function of wavenumber only. It is determined by averaging the energy for all directions for the same wavenumber. Wavenumber k is the spatial frequency of a wave measured in cycles per unit distance. The Nyquist wavenumber N is the largest wavenumber that has been sampled by the grid which is the highest frequency that it

is possible to measure given a fixed sample interval as expressed in equation 2.27 (Fedi & Mastro, 2018).

$$N = \frac{1}{2d} \tag{2.27}$$

Where d is the sample interval, the expression in equation 2.28 determines the depth of a statistical ensemble of sources.

$$h = -\frac{s}{4\pi} \tag{2.28}$$

Where h is depth and s is the five-point average of the slope of the energy spectrum (Spector & Grant, 1970). The basal depth z_b which is assumed to be the curie point depth (Okubo, Graf, Hansen, Ogawa, & Tsu, 1985) is expressed in equation 2.29 (Fedi & Mastro, 2018).

$$z_b = 2z_0 - z_t \tag{2.29}$$

Where,

z_0 is mean depth to the deep source body, z_t is mean depth to the shallow source body and z_b is the Curie point depth.

Curie point isotherm is the depth at which magnetism of materials disappears due to high temperatures, and the temperature at this point is called curie temperature. Minerals exhibit variation in curie temperatures, resulting in rocks having different curie point temperatures due to different minerals present in their composition. In the lithosphere, magnetite is the most abundant magnetic mineral and its curie temperature is approximately 578 ℃. The depth corresponding to curie temperature is referred to

as curie point isotherm depth, and minerals below it do not influence the magnetic field in the lithosphere (Jiao & Lei, 2019).

The circular movement of electrons around the nucleus and their spin causes magnetic moments in atoms (Parasnis, 1986). From quantum theory, two electrons spinning in opposite directions can be in the same electron state, and such two electrons are called paired electrons. The paired electrons generate zero magnetic moments because individual magnetic moment contributions cancel out. When there is an external magnetic field such as the Earth's geomagnetic field, the spin magnetic moments of neighbouring atoms are aligned uniformly, thus generating overall magnetisation.

There are no unpaired electrons in diamagnetic minerals such as halite hence all the electron shells are complete (Kearey et al., 2002). The magnetisation is induced when an external magnetic field is introduced, for example, the Earth's geomagnetic field. Negative magnetic susceptibility arises because electrons revolve in a manner that produces a magnetic field that resists the applied field.

There are unpaired electrons in paramagnetic minerals for example fayerite, amphiboles, pyroxenes, olivines, garnets and biotite (Reynolds, 1998). This results in incomplete electron shells that generate unbalanced spin magnetic moments among atoms of paramagnetic minerals. When an external magnetic field such as the Earth's geomagnetic field is introduced, the magnetic moments organise themselves in line with the direction of an applied magnetic field. This produces a weak positive anomaly that reduces as the materials' temperature increases. This is in agreement with the Curie-Weiss law (Reynolds, 1998). During spectral analysis of magnetic data, paramagnetic materials generate a bigger anomaly than diamagnetic rocks.

The temperature and the strength of the applied magnetic field affect the magnetic susceptibility of ferromagnetic minerals. Interaction among the neighbouring atoms

and overlap of electron shells causes the spin moments of unpaired electrons to join together magnetically. These results in magnetic moments being aligned parallel or antiparallel. The magnetic coupling can be in such a way that the magnetic moments are aligned either parallel or antiparallel.

Ferromagnetic minerals such as cobalt, nickel, and iron (Reynolds, 1998) do not occur commonly but can be found in some areas. These ferromagnetic minerals have a parallel arrangement of magnetic moments. When the temperature of a ferromagnetic mineral rises above the curie temperature T_C, the dipoles are disorganised and the mineral ceases to exhibit ferromagnetic properties thus showing Paramagnetic behaviour.

The magnetic moments of antiferromagnetic minerals are antiparallel to one another, for example hematite (Telford et al., 1990). The overall magnetic moment of antiferromagnetic mineral is zero because the magnetism of dipoles in opposite directions cancel each other. The dipoles in ferrimagnetic minerals are antiparallel and unequal, generating a resultant magnetisation. Common ferrimagnetic minerals are magnetite, titanomagnetite, and Ilmenite (Parasnis, 1986). Ferrimagnetic minerals are characterised by spontaneous magnetisation and large magnetic susceptibilities, for example, pyrrhotite. Above the curie temperature, ferrimagnetic minerals cease to possess magnetic behaviour and do not contribute to the magnetic field of the Earth's crust (Jiao & Lei, 2019). Common magnetic rocks occurring within the Earth's crust are either ferrimagnetic or antiferromagnetic.

2.2.4 Instrumentation

2.2.4.1 CG-5 Gravimeter

The CG-5 gravimeter is used for relative gravity measurements on the Earth's surface. This instrument provides the relative measurement of gravity between two different

locations on the Earth's surface. It has a reading resolution of 0.001 mGal and repeatability accuracy of 0.005 mGal (Scintrex, 2012). The CG-5 gravimeter is designed to level itself before the reading is taken. The CG-5 gravimeter operates based on the principle of a fused quartz elastic system. The instrument uses minimal electrostatic recovering force and spring to neutralize gravitational force on proof mass. The changes in gravity beneath the Earth's surface caused by underground mass distribution affect the location of the mass. The gravimeter contains a transducer system used to detect the proof mass. Once identified, the mass is reset to its original location by an automatic setup that feeds a DC signal to the recovering force. The signal sent back to the control system measures gravity variations within the Earth's subsurface at the gravity station. The signal is then changed into digital data and sent to the information section of the gravimeter for recording (Scintrex, 2012).

The fused quartz system has natural and stretchable features with controlled movements near the proof mass, allowing the device to be used without holding it firmly. The CG-5 gravimeter is also connected to an impact absorber which protects it from external forces and can level itself. The CG-5 gravimeter can be used in detailed geophysical and regional reconnaissance studies. This is because the device's system detects and sends signals of gravity of over 8000 mGals without resetting to the original value. The instrument also uses a minimal noise digital pattern with an exact analogue to digital changer generating a degree of fineness of 0.001 mGal. The CG-5 gravimeter contains inbuilt tilt devices used to automatically correct errors in values obtained. The error arises because the device cannot balance on the fluctuating ground. The CG-5 gravimeter uses a system to take data from a gravity station without unsettling the meter (Scintrex, 2012).

Figure 2.5: CG-5 gravimeter

2.2.4.2 Proton precession magnetometer

The proton precession magnetometer measures the size of the Earth's magnetic field. It works based on a sensor that contains hydrogen atoms like kerosene and water covered in a coil, as shown in Figure 2.6. The protons within the hydrogen atoms function have small dipoles and appear parallel to the ambient geomagnetic field B_e Figure 2.6 (b). A current is passed through the coil Figure 2.6 (a) to generate a magnetic field B_p Figure 2.6 (c) should be $50 - 100$ times larger than the geomagnetic field and in a different direction, causing the protons to realign in this new direction. The current to the coil is then cut to remove the polarizing field very fast. The protons return to their original alignment with B_e by spiralling Figure 2.6 (d) in phase around

this direction with about 0.5 ms, taking one to three seconds to achieve their original orientation (Kearey et al., 2002).

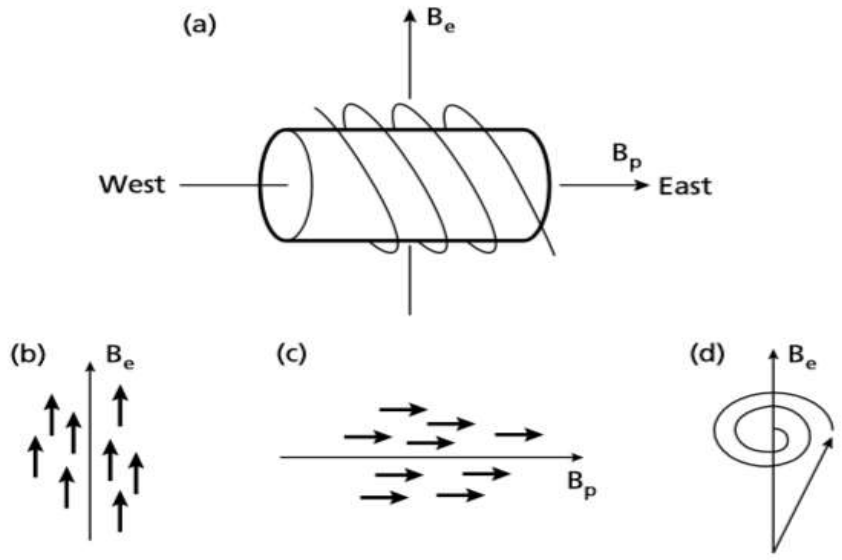

Figure 2.6: Proton precession magnetometer

The formula for the frequency *f* of this spiralling is expressed in equation 2.30 (Kearey et al., 2002).

$$f = \frac{\gamma_p B_e}{2\pi} \qquad 2.30$$

Where γ_p is an accurate constant value that represents the gyromagnetic ratio of the proton. The value of f, about 2 kHz, is obtained by measuring the alternating voltage of the same frequency stimulated to flow in the coil by precessing protons. As a result, f gives the precise measuring of the magnetic field (Kearey et al., 2002). The strength of the total field can be measured to an accuracy of 0.1 nT. The sensor is set at a high angle with the Earth's magnetic field. Rapid changes measuring above 600 nT/m in the magnetic field affect the position of the cylindrical sensor and, as a result lower the value of readings obtained (Telford et al., 1990). For example, this may arise when the sensor is placed near a magnetic material.

2.2.5 Euler deconvolution

2.2.5.1 Introduction

Euler deconvolution method provides location and depth estimates of anomaly sources within the Earth's subsurface (Nyakundi, Githiri, & Ambuso, 2017). It locates the causative body and determines its depth from the observation level. It generates a map that exhibits the positions and depths of the observed gravity anomaly sources. Euler deconvolution does not adopt any geologic model (Pawan, Ramprasad, Ramana, Desa, & Shailaja, 2007); thus can be applied for the interpretation of gridded gravity and magnetic data even when the geology of the study area cannot be represented by a particular model such as a prism (Thompson, 1982).

2.2.5.2 Euler deconvolution theory

Euler deconvolution is a potential field data analysis technique for estimating the depth and position of a causative body (Hong et al., 2017). The technique combines the potential field and its gradient components to locate the potential anomalous source, with the strength of homogeneity implied as a structural index, and it is a suitable method for figuring out anomalies resulting from isolated and multiple sources (Dawi, Tianyou, Hui, & Dapeny, 2004). The technique relates the potential field, for example, gravity or magnetic field and its gradient components, to the location of the source of an anomaly with a degree of homogeneity expressed as a structural index (Nyakundi et al., 2017).

Euler deconvolution is based on the Euler equation of homogeneity (Reid & Thurston, 2014) expressed in equation 2.31;

$$(x - x_0)T_{zx} + (y - y_0)T_{zy} + (z - z_0)T_{zz} = n(B_z - T_z) \qquad 2.31$$

Where T_z is a vertical component of potential field anomaly source with the degree of homogeneity n, (x_0, y_0, z_0) is the coordinate of the field anomaly source in the Earth's crust to be determined while (x, y, z) is the measured co- ordinate. Parameters (T_{zx}, T_{zy}, T_{zz}) are the determined gradients in the x- , y- and z- directions, n is the structural index and B_z is the regional potential field value to be approximated (Melo & Barbosa, 2018).

The Euler deconvolution method first determines the analytic signal, finds peaks in the analytic signal then uses these peak locations for Euler deconvolution with appropriate window size (Castro, Oliveira, deSouza, & Ferreira, 2019). The analytic signal grid is calculated and displayed from derivative grids. Analytic signal grid expression shown in equation 2.32 is the square root of the sum of the squares of the derivatives in the x, y and z directions (Thompson, 1982).

$$A = \sqrt{(\partial x \times \partial x) + (\partial y \times \partial y) + (\partial z \times \partial z)} \qquad 2.32$$

where A is the analytic signal grid.

This technique is preferred as solutions are only determined over-identified analytic signal peaks, the window size varies according to anomaly size and the final solution involves only a few more accurate depth estimates (Beard & Szidarovszky, 2018).

2.2.5.3 Structural index

An appropriate structural index is applied when performing Euler deconvolution analysis (Castro et al., 2019). In the regional interpretation of gravity data, structural indices of 0.5, 1.0 and 2.0 are common for fault, contact, sill, dyke and sphere location (Felipe & Valeria, 2017) while structural indices of 0.5, 1.0, 2.0 and 3.0 are common

for thick step, sill or dyke, pipe and sphere respectively for magnetic data interpretation (Beard & Szidarovszky, 2018). A structural index is a measure of the rate of change of potential field with distance. The basic principle of the structural index is Euler's homogeneity equation (Reid, Allsop, Granser, Millett, & Somerton, 1990) expressed in equation 2.33.

$$x\frac{\partial f}{\partial x} + y\frac{\partial f}{\partial y} + z\frac{\partial f}{\partial z} = nf \qquad 2.33$$

For potential field data analysis, the expression in equation 2.33 is rewritten as equation 2.34 (Melo & Barbosa, 2018).

$$(x - x_0)\frac{\partial T}{\partial x} + (y - y_0)\frac{\partial T}{\partial y} + (z - z_0)\frac{\partial T}{\partial z} = N(B - T) \qquad 2.34$$

where (x_0, y_0, z_0) is the position of anomaly source whose vertical component of potential field T is measured at (x, y, z). N is the structural index, and B is the regional value of the potential field (Reid & Thurston, 2014). A structural index is calculated by determining how many infinite dimensions are present in a geologic representation (Thompson, 1982). The structural representation index is the infinite dimension number taken away from the maximum structural index for the field. The maximum structural index for gravity field is two because the gravity field from a point source dies off as $1/r^2$ (Kearey et al., 2002) while it is three for a magnetic field because the magnetic field from a point dipole falls off as $1/r^3$. A structural index of zero suggests that the potential field does not vary with distance from the anomaly source, which is not true in real experience.

2.2.6 Forward modelling

2.2.6.1 Introduction

Forward modelling of gravity and magnetic data entails the determination of the size, shape, and physical parameters of the field anomaly source from the potential field measurements (Telford et al., 1990). It involves quantitative interpretation, which entails an iteration process where the anomaly generated by the constructed computer model is compared with the measured residual anomaly (Abdelfettah et al., 2020). It is based on a starting model postulated from the study area's geology (Aziz, Miller, Giraldo, & Carigali, 2019). This is used to construct and constrain the computer models. The model parameters are varied, and the anomaly calculation is carried out. This is repeated until there is a fit between the calculated and measured residual anomalies. However, this does not provide the only outcome as several models can result in the same anomaly (Kearey et al., 2002).

2.2.6.2 Theory of forwarding modelling for gravity data

In a two-dimensional case, it is postulated that the causative body is infinitely long parallel to its cross-section surface. Suppose line elements that are parallel to the strike are considered to replace the cross-sectional shape. In that case, each line element contributes to the vertical component of gravity at the source, as shown in Figure 2.7. By summing up the effect of all these line elements, the gravity anomaly of the causative body can be determined (Lowrie, 2007). This is an integration over the end surface of the causative body, and the gravity anomaly is given by equation 2.35. Therefore, forward modelling of gravity data determines the gravitational field produced by the causative body underlying within the Earth’s crust (Hirt, 2015).

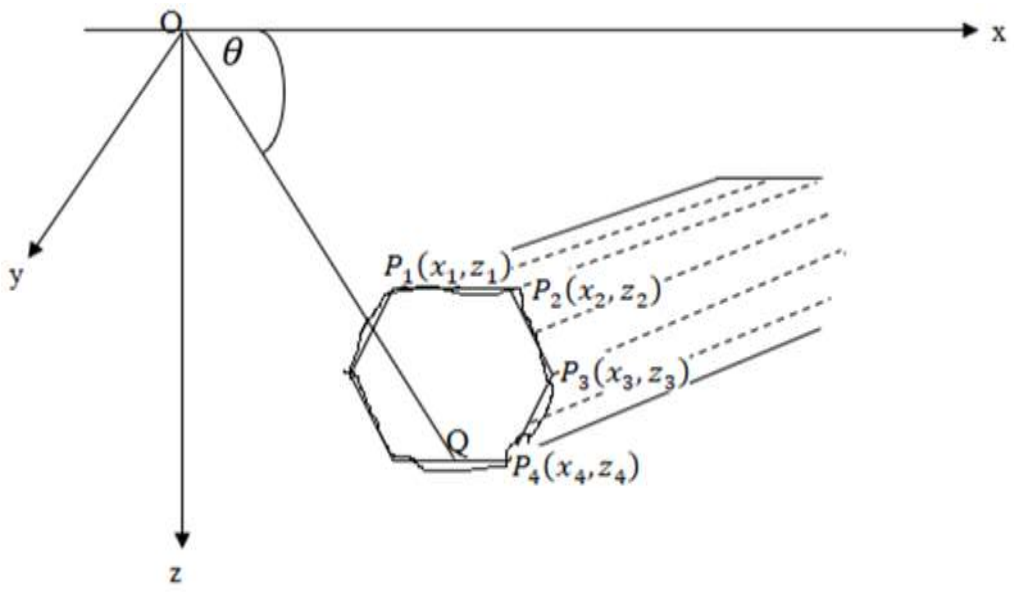

Figure 2.7: Gravity anomaly of the irregular body using a multi-sided polygon

$$\Delta g_z = 2G\Delta\rho \oint z d\theta \qquad 2.35$$

Where θ is the angle between the x-axis and the line from the origin to the gravity anomaly source, g_z is the vertical gravitational field, G is the universal gravitational constant, and z is the depth to the source, as shown in Figure 2.7. The integration over the end surface is converted to an integration around its boundary. The computer algorithm for calculating this integral is done by replacing the original cross-sectional shape with an n-sided polygon, as shown in Figure 2.7. The polygon corners position (x, z) and density contrast is used to compute the gravity anomaly. If the source is shifted to the next position along with the profile, the x-coordinate of the polygon corners vary. This is repeated until the computed anomaly of the gravity model fits with the measured residual anomaly (Lowrie, 2007).

2.2.6.3 Theory of forwarding modelling for magnetic data

Forward modelling of magnetic data involves the construction of the starting model based on the geology of the study area and its calculated anomalies. The calculated magnetic anomaly is compared to the observed anomaly. This calculation is repeated until the computed and observed anomaly fit. In two-dimensional magnetic modelling, the cross-sectional shape of the causative mass is assumed to be of a polygon. The magnetic anomaly of the polygon is determined by summing up the individual contributions of infinite slabs with sloping edges corresponding to the sides of the polygon, as shown in Figure 2.8. The horizontal magnetic field ΔH, vertical magnetic field ΔZ, and total magnetic field ΔB anomalies in nanotesla of the slab displayed in Figure 2.8 are given by equations 2.36, 2.37, and 2.38, respectively (Kearey et al., 2002).

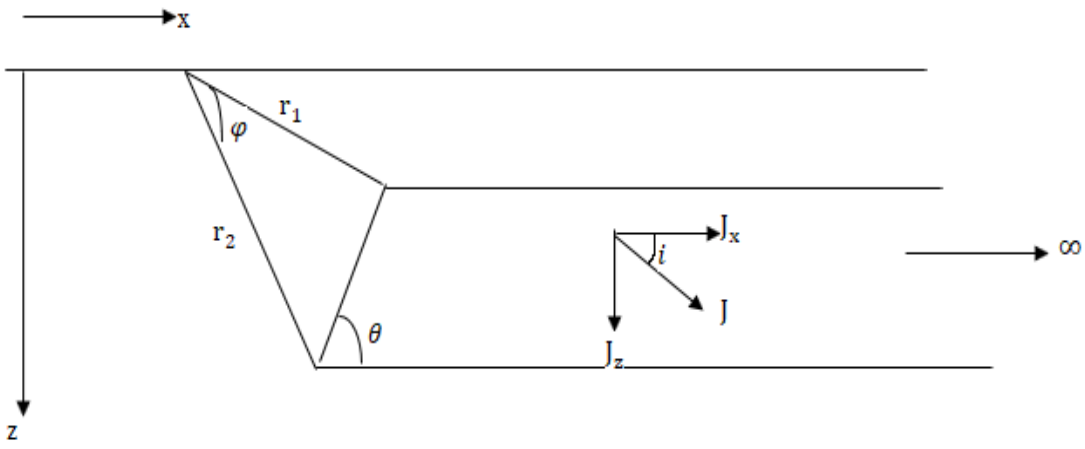

Figure 2.8: Magnetic anomaly of a slab with a sloping edge.

$$\Delta Z = 200 \sin\theta \left[J_x\{\sin\theta \log\left({}^{r_2}/_{r_1}\right) + \varphi\cos\theta\} + J_z\{\cos\theta \log\left({}^{r_2}/_{r_1}\right) - \varphi\sin\theta\}\right] \quad 2.36$$

$$\Delta H = 200\ \sin\theta\ [J_x\ \{\varphi \sin\theta - \cos\theta \log\ (^{r_2}/_{r_1})\}\ +\ J_z\{\varphi \cos\theta\ +$$
$$\sin\theta \log(^{r_2}/_{r_1})\}]\ \sin\alpha \qquad 2.37$$

$$\Delta B = \Delta Z \sin I\ +\ \Delta H \cos I \qquad 2.38$$

where the angles are given in radians. $J_x = J\cos i$ and $J_z = J\sin i$ is the horizontal and vertical components of the magnetization J, and a is the horizontal angle between the direction of the profile and magnetic North. I is the inclination of the geomagnetic field (Kearey et al., 2002).

CHAPTER THREE

METHODOLOGY

3.0 Introduction

This section describes and explains the materials and methods used to collect the geophysical data in this study. It describes heat flow, gravity, and magnetic data collection procedures. The chapter also explains the scientific methods used to process, analyse and interpret the collected geophysical data.

3.1 Instrumentation

These are devices used for measurement during data collection. Heat flow data was collected using a spike mechanical tool and a thermocouple thermometer. Spike mechanical tool was used for hole digging, and a thermocouple was used for temperature measurement. The magnetic field was measured using a proton precession magnetometer G-856 model. GPS was used to locate station coordinates. The gravity field was measured using the CG-5 gravimeter, giving relative gravity measurements in milligals between the stations. CG-5 gravimeter has an inbuilt GPS used to locate gravity station coordinates.

3.2 Data acquisition

3.2.1 Acquisition of heat flow data

A total of 228 stations were established based on surface manifestations in the study area covering approximately $420\ km^2$. Holes of 1-metre depth were bored in each station for temperature measurements. The spike mechanical tool was used to drill the holes. Temperature measurements were taken at $50\ cm$ and $100\ cm$ depth using a thermocouple thermometer. A thermocouple thermometer consists of two different

wires connected. One end was placed where the temperature was measured, while the other was maintained at a relatively lower temperature. The temperature difference caused an electromotive force equivalent to the two ends' temperature and was used to generate the reading on a temperature scale. Temperature readings near the Earth's surface were not taken due to climatic effects such as the heat from the sun and drought, which might have interfered with the values. The global positioning system GPS was used for each hole station's latitude, longitude, and altitude measurements. Heat flow data was collected and recorded as shown in appendix I.

Heat flow data was used to determine the geothermal gradient, which subsequently determined the heat flux for the study area. The heat flux values were used to generate a heat flux contour map that displays thermal distribution and heat loss within the Earth's subsurface in this study area. It precisely exhibits areas of elevated temperature gradients and reduced temperature gradients. For instance, in station 1, the following processing procedure was done. Recorded temperature at 50 cm depth $= 48.2$ ℃ and at 100 cm depth $= 58.2$ ℃. From equation 2.1,

Thermal gradient $\mathrm{M} = \frac{58.2℃ - 48.2℃}{0.5} = 20\ ℃\mathrm{m}^{-1}$

Applying equation 2.3, heat flux $\mathrm{q} = \mathrm{k} \times \mathrm{M} = 2\ \mathrm{Wm}^{-1}℃^{-1} \times 20\ ℃\mathrm{m}^{-1} = 40\ \mathrm{Wm}^{-2}$

These thermal gradients and heat flux calculations were done for all the study area measuring stations, as displayed in appendix I. The result was used to identify profile locations for forward modelling using gravity and magnetic data to better delineate and characterize a possible geothermal heat source in the Eburru area.

3.2.2 Acquisition of gravity data

Gravity data were collected from 195 observation points based on heat flow results using a CG-5 gravimeter. The daily instrumental drift was addressed by repeating the measurements at the base station at the beginning and the end of any day data acquisition. The time of occupation, northing, easting, altitude, and gravity value in milligals was recorded for every observation point. Gravity data were collected and recorded as shown in appendix II.

A gravity survey aimed to image the changes in the density of the underlying masses within the Earth's subsurface, resulting in a gravity anomaly. All variations which do not result from the effects of underlying masses were removed to determine gravity anomaly. This process is called gravity reduction. There would be no gravity anomaly if the density of the underlying masses was constant. Gravity anomaly was either positive when the density of the underlying causative mass was higher than the host rocks, or negative if the density of the underlying causative body was less than the host rocks. The following gravity data corrections were done.

3.2.2.1 Instrumental drift correction

The daily instrumental drift was addressed by repeating the measurements at the base station at the beginning and the end of any day data acquisition. This correction was done because the gravimeter reads different values in the same station at different times. The drift curve was plotted from the base station readings as shown in appendix V to determine the drift correction value. For instance, instrumental drift for station 1 was -0.023, as shown in appendix V.

$$\text{Corrected gravity reading} = 1770.864 - -0.023 = 1770.887 \text{ mGals}$$

This was done for all the other gravity stations, as shown in appendix II.

3.2.2.2 Latitude correction (LC)

Latitude correction gave the predicted theoretical value of gravity at any point on the Earth's surface at sea level. It was done by applying Claraut's formula in equation 2.13. The absolute value of gravity at a station with co-ordinates $(196658.299\ \text{E}, 9937021.505\ \text{N})$ was 977367.542 mGals. The gravity reading at this station was 1843.163 mGals. This was used to generate absolute gravity values for the other stations, as shown in appendix II. This was done by adding the difference between the gravity readings of the stations and 1843.163 mGals. For example, the absolute value of gravity in station 1 was given by;

$$\text{The absolute value of gravity} = 977367.542 + (1770.888 - 1843.163) = 977295.267\ \text{mGals}.$$

This was done for all the other stations to generate absolute gravity values, as shown in appendix II. Latitude correction was done by applying Claraut's formula in equation 2.13. For example, Latitude Correction for station 1 was given by;

$$\text{Latitude Correction for Station 1} = 978032.68\{1 + 0.005278895\sin^2(-0.62113841) + 0.000023462\sin^4(-0.62113841)\} = 978033.2839\ \text{mGals}$$

This was done for all the other gravity stations. Latitude correction was performed by subtracting these values from the determined absolute gravity values. For example, in station 1,

$$\text{Latitude corrected value} = \text{Absolute value} - \text{Latitude correction} = 977295.267 - 978033.2839 = -738.0169\ \text{mGals}$$

This was done for all the other gravity stations, as displayed in appendix II.

3.2.2.3 Free Air Correction (FAC)

Free air correction was done to account for the decrease in gravity with height. The distance from the centre of mass of the Earth increases with height, thus reducing the gravitational field strength. This was corrected by adding the Free air correction value, which is positive for observations above sea level and negative for observations done below sea level. This study area is above sea level, and all the Free Air Correction values were positive and hence were added to the observed gravity. For instance, in station 1 the following calculation was done by applying equation 2.16.

$$\text{FAC} = 0.3086 \times \text{Elevation} = 0.3086 \times 2315.327 = 714.5099 \text{ mGals}$$

This calculation was done for all the 195 stations, as shown in appendix II.

3.2.2.4 Bouguer Correction (BC)

Bouguer correction removes the effect on the Earth's gravitational field by the presence of rocks between the observation point and the sea level. Nettleton's method was used to estimate the average density of crustal rocks between the observation point and the geoid in the study area.

BC was subtracted from the observed gravity as the study was carried out above sea level. It was done by applying the formula in Equation 2.17. For example, station 1 BC was calculated as follows.

$$\text{BC} = 0.04191\rho h = 0.04191 \times 2.67 \times 2315.327 = 259.0844 \text{ mGals}.$$

Where ρ is 2.67 gcm^{-3} and h is the height above sea level. This was repeated for all the other stations, as displayed in appendix II.

3.2.2.5 Terrain Correction (TC)

Terrain correction was done using the Oasis Montaj computer programme as discussed in section 2.2.2.2. It was based on the hammer chart theory and digital elevation model DEM. The DEM was run for the study area, which computed terrain correction values as displayed in appendix II. This correction was done by adding TC values to the observed gravity.

3.2.2.6 Complete Bouguer Anomaly (CBA)

Complete Bouguer Anomaly CBA was the outcome of all gravity corrections. It was determined after all the gravity corrections had been applied to the observed gravity data, as shown in Equation 3.1.

$$\text{CBA} = \text{Absolute gravity value after drift correction} - \text{LC} + \text{FAC} - \text{BC} + \text{TC} \quad (3.1)$$

For example, in station 1,

$$\text{CBA} = 977295.267 - 978033.2839 + 714.5099122 - 259.0843967 + 0.560443239 = -282.031 \text{ mGals.}$$

This was done for all the 195 stations, as displayed in appendix II.

3.3.3 Acquisition of magnetic data

Magnetic data were collected from a total of 229 stations based on heat flow results. Two proton precession magnetometers G-856 model, were used. One magnetometer

was positioned at the base station to take readings after every 5 minutes throughout the data collection day for diurnal variation correction. The other magnetometer was moved to stations for data collection. Occupation time, easting, northing, and magnetic reading were recorded at each station. The magnetic data were collected and recorded, as shown in appendix III.

All variations which do not result from structures within the Earth's subsurface were removed before the raw magnetic data was interpreted. This process is called magnetic data reduction, resulting in a residual magnetic anomaly. It shows lateral variations in the magnetic susceptibility of rocks within the Earth's subsurface. This enabled imaging of causative bodies resulting in the observed residual magnetic anomaly. The following magnetic data reduction was done.

3.3.3.1 Diurnal variation correction

Diurnal variation correction was addressed by positioning a stationary magnetometer at a base station to read magnetic field values every five minutes throughout the data collection day. The readings from the stationary magnetometer B were used to plot a diurnal curve, as shown in appendix VI. The diurnal curve was used to determine the diurnal correction values by getting the difference between the magnetic reading at a particular time and the first reading of the data collection day. This determined the diurnal correction at the time of occupation in a specific station. This was done for all the other occupation times in the other stations. These diurnal correction values were used to correct for diurnal variations in other measuring stations throughout the day. This was done by subtracting the diurnal correction value when the reading was taken in a particular station. For instance, in station 1, the diurnal correction was -1.8 nT. This was done for all the magnetic stations, as displayed in appendix III.

3.3.3.2 Geomagnetic correction

A geomagnetic correction was done after the diurnal variation correction. It was done using the International Geomagnetic Reference Field (IGRF) online calculator. It gave magnetic field theoretical values of every station, as shown in appendix III. The IGRF values were subtracted from the diurnal variation corrected values to obtain residual magnetic anomaly, as shown in equation 3.2.

$$B_{\text{res anomaly}} = B_{\text{obs}} - \text{DC} - \text{IGRF} \tag{3.2}$$

Where $B_{\text{res anomaly}}$ is the residual magnetic anomaly, B_{obs} is observed magnetic field, and DC is the diurnal correction.

For example, in station 1, the residual magnetic anomaly was determined by applying equation 3.2.

$$\text{Residual magnetic anomaly} = 33594.2 - 1.8 - 33546 = 46.4 \text{ nT}.$$

This was done for all the magnetic stations to generate residual magnetic anomalies, as shown in appendix III.

3.4 Upward continuation

An upward continuation of 500 m was applied to the gravity and magnetic data. This was done to increase the height of observation points. This enhances the effect of deep structures of interest.

3.5 Fast Fourier Transform

It was done to remove the regional trend from the observed anomalies to generate residual anomalies. This was achieved by converting the space domain grid data to wavenumber domain grid data using equation 2.24. The filters were applied to the wavenumber domain grid. It was converted back to the space domain grid data using equation 2.25.

3.6 Euler Deconvolution

Euler deconvolution method was used to locate and estimate the depth to the top of the anomaly sources for gridded magnetic and gravity data. It was done using Oasis Montaj geosoft software by first calculating the analytic signal grid. The analytic signal grid was calculated from x-, y- and z-derivative grids. Peak identifying algorithm was applied to the analytic signal grid to locate peaks and display them as symbols on a map. Euler deconvolution identified only those windows which circumnavigate peak-like structures in the data. A peak identifying procedure was carried out, which located peaks and estimated a window size using the positions of adjacent points. These locations and window sizes were then used to define the windows for Euler deconvolution. This technique was preferred as solutions were only determined over-identified analytic signal peaks, and the window size varied according to anomaly size. Structural index of 0.5 and 1.0 was done for gridded gravity data as it corresponds to a geometrical shape of a ribbon and pipe, respectively. These geometrical shapes were used to calculate and estimate the location of dyke like structures intruding within the Earth's subsurface. Structural index of 0.5, 1.0, and 2.0 was done for gridded magnetic data as it corresponds to a geometrical shape of a contact, ribbon, and pipe, respectively. These shapes were used to calculate and estimate the location of fault, sill, and dyke structures in the Earth's crust. A higher structural index resulted in deeper solutions, while a lower structural index resulted in

shallow solutions (Reid et al., 1990); hence it was necessary to run the related structural indices for better imaging of the anomaly sources.

3.7 Forward Modelling

Joint forward modelling of gravity and magnetic data was carried out to image the possible causes of the observed anomalies. It imaged the size, shape, and depth of the causative bodies within the Earth's subsurface in the study area. The selected profiles for forward modelling were chosen based on heat flux information. Forward modelling of gravity and magnetic data for the profiles was done jointly using Gm-sys in the oasis montaj geosoft computer programme. It entailed an iteration process where the anomaly generated by the constructed computer model was compared with the observed residual anomaly (Abdelfettah et al., 2020). The starting model was postulated based on the structural geology of the study area (Aziz et al., 2019). The geology of the Eburru study area is of volcanic origin dominated by basalt, andesite, granite, rhyolite, trachyte, tuff, ignimbrites and pyroclastic flow (Kiende & Kandie, 2015). This was used to construct and constrain the computer models. The model parameters were varied, and calculations were performed. This was repeated until there was a good match between the calculated anomaly and the observed anomaly.

CHAPTER FOUR

RESULTS AND DISCUSSION

4.0 Introduction

This chapter discusses the study results and their interpretation. The study results are displayed in the form of maps. The results were interpreted using qualitative and quantitative methods. Qualitative method of interpretation involved visual inspection of the maps to describe and explain variation in physical quantities within the Earth's crust. The quantitative method of interpretation involved estimating the size, shape, and depth of the anomalous mass in the Earth's crust.

4.1 Topography of Eburru study area

Figure 4.1 is the elevation map of the Eburru study area. It shows the terrain of the study area in heights above the sea level which ranges from the lowest at approximately 1792 m to the highest point at approximately 2689 m. It displays the highest point to the South in OlDoinyo Opuru at approximately 2519 m and the lowest point to the North of the study area towards Lake Elmenteita at approximately 1810 m. Generally, the elevation map exhibits a highland in the Southern parts of the study area towards the Eburru crater in OlDoinyo Opuru, and altitude decreases Northwards toward Lake Elmenteita, as shown in Figure 4.1. The volcanic activity in the area probably resulted in increased elevation to the South due to mantle materials pushing towards the Earth's crust. Gravity high and reduced magnetic susceptibility in these parts could indicate geothermal heat sources because hot, dense materials from the mantle have reduced magnetism penetrated the Earth's crust.

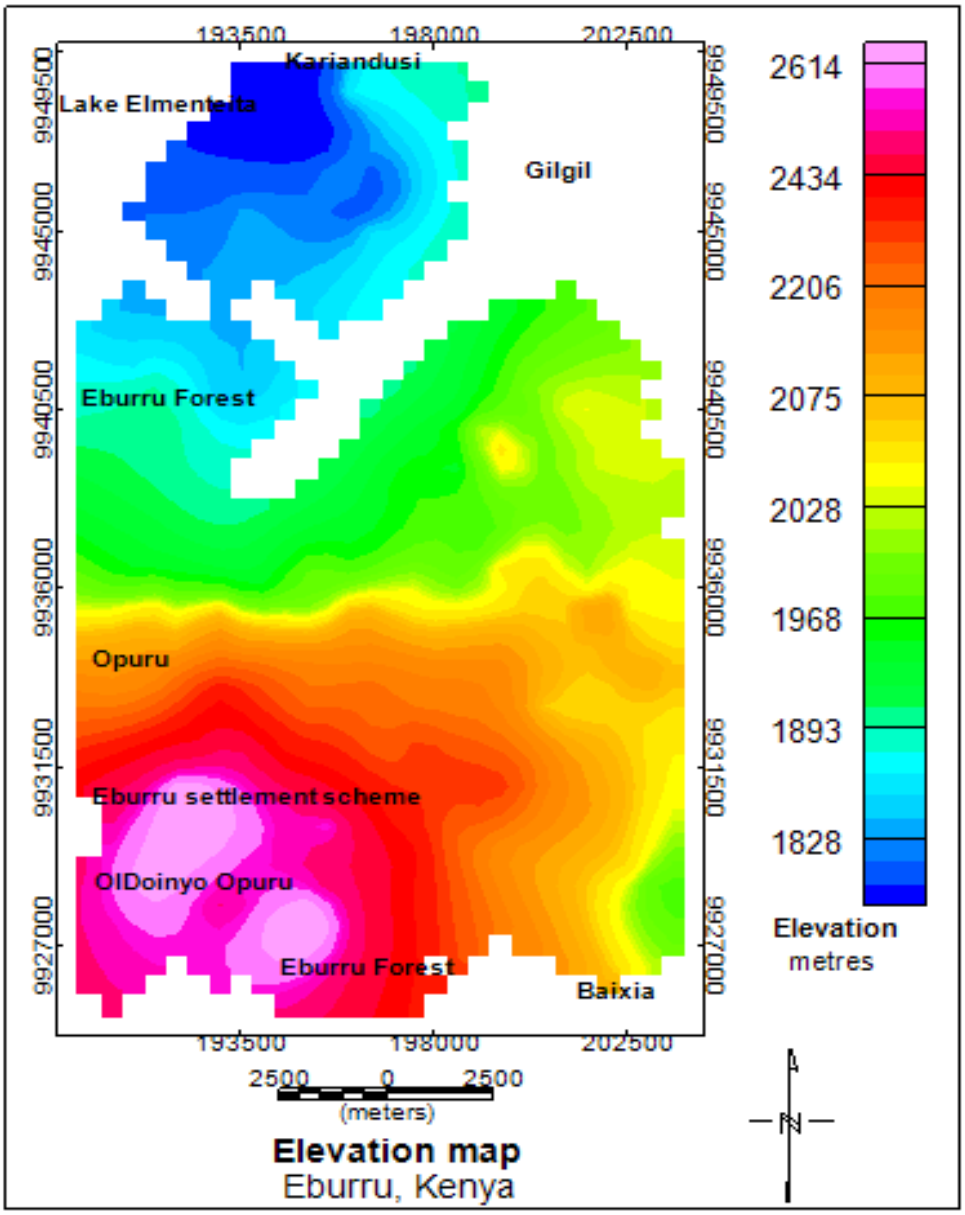

Figure 4.1: Elevation map for Eburru study area

4.2 Heat flow results and interpretation

Heat flow data points were distributed in the study area based on surface heat source manifestations, as displayed in Figure 4.2. The station spacing was 500 m apart. The blank area was occupied by a thicket cover with hard rock, making it impossible to

dig holes for heat flow data measurement. Temperature, temperature gradient, and heat flux contour maps displayed the heat flow results. The heat flux contour map displays thermal distribution and heat loss in the Earth's crust within the study area. It precisely exhibits areas of high-temperature gradients and decreased temperature gradients. Gravity and magnetic data were forward modelled to explain the heat flux variation in the area. This resulted in better delineation and characterization of possible geothermal heat sources in the Eburru study area.

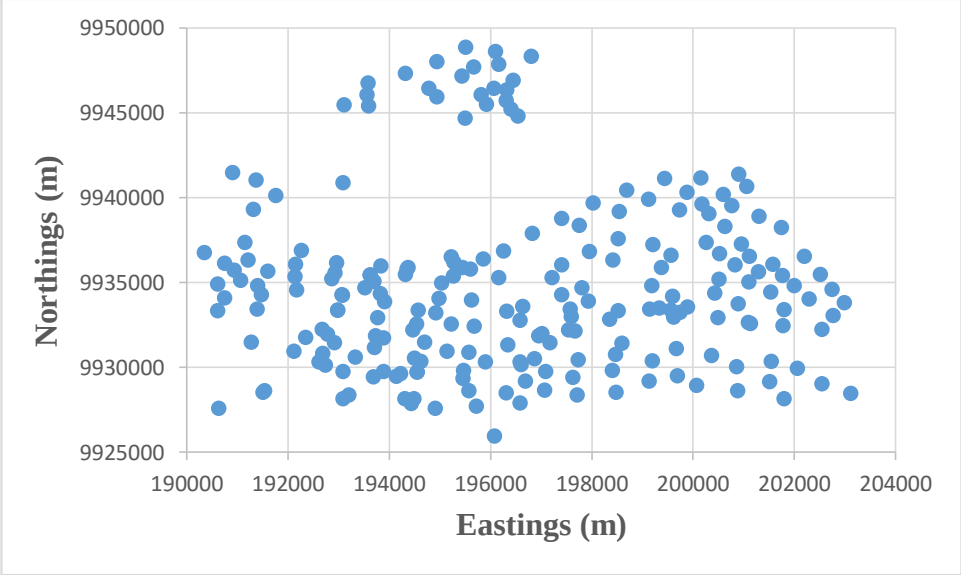

Figure 4.2: Distribution of heat flow stations

Figure 4.3 shows temperature variation at 1-metre depth within the study area. Surface temperature measurements were not considered due to climatic effects like drought, heat from the sun, and wind. Variation of temperature at 1-metre depth was plotted to show its distribution because it has minimum effects from climatic conditions of the atmosphere. It images temperature variation due to the heat within the host rocks at that depth. Temperatures at 1-metre depth in this study area vary between 13.8 ℃ to 94.2 ℃, with a mean temperature of 39.75 ℃. Figure 4.3 shows a relatively low-temperature area trending in a North-South orientation. It begins from the North near

Lake Elmenteita through Eburru Forest, Opuru, OlDoinyo Opuru to the South of the study area. Areas greater than 40 ℃ isotherms were considered thermally active grounds (Mburu, 2006; Mwawasi, 2012). From Figure 4.3, it is observed that active thermal ground is to the central south of the study area and oriented in a North-South direction. It cuts through the Eburru crater at OlDoinyo Opuru in a North-South direction. This trend reveals that possibly the structures in this study area are trending in a North-South direction, hence associated with rifting.

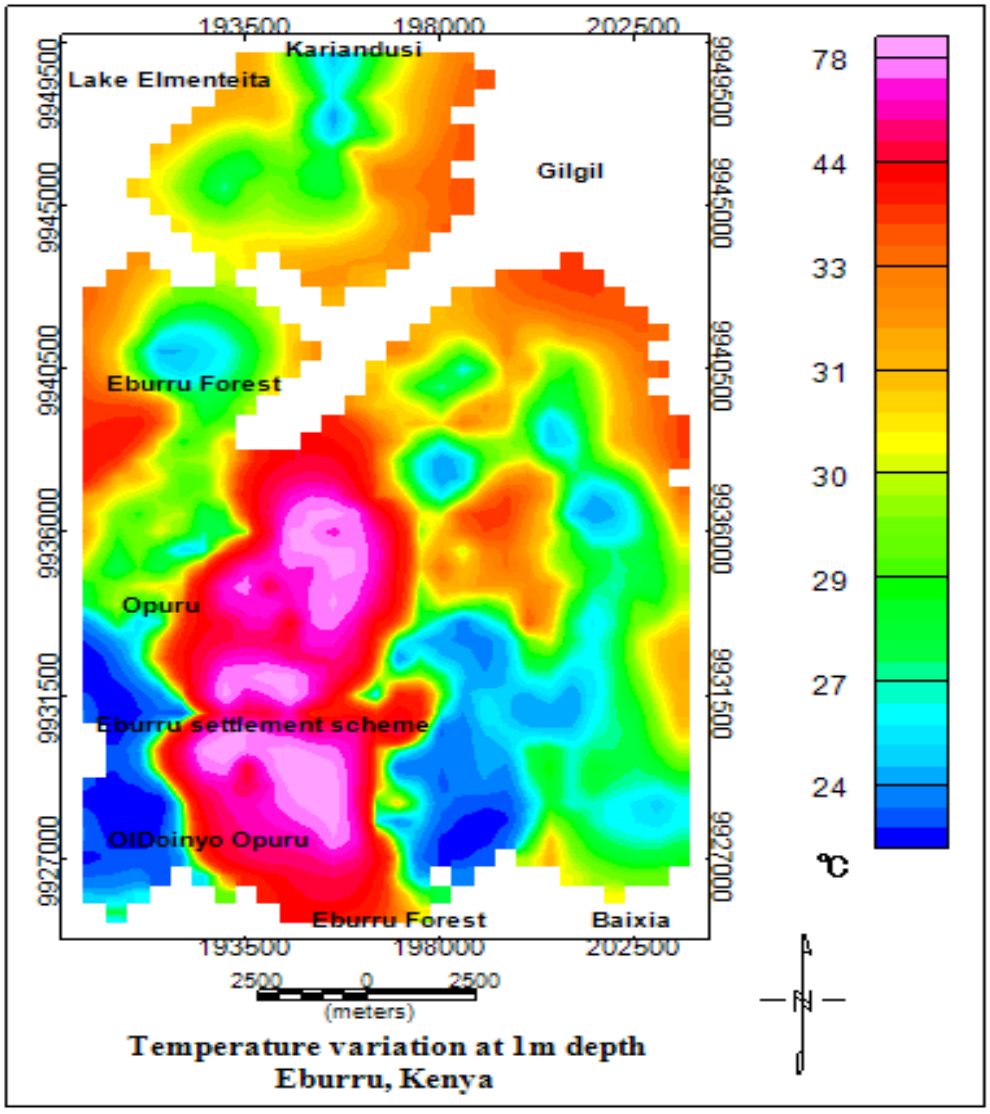

Figure 4.3: Temperature distribution map at 1 m depth

Figure 4.4 shows the geothermal temperature gradient in degrees Celsius per metre for the study area. The geothermal temperature gradient in Figure 4.4 is the rate of temperature increase from 50 cm depth to 100 cm depth. The surface temperature readings were not taken into account because of the effect of climatic conditions. The geothermal gradient in this area varies from $0.01\,°\mathrm{Cm}^{-1}$ to a maximum of $46.4\,°\mathrm{Cm}^{-1}$. The mean geothermal gradient was determined to be $5.03\,°\mathrm{Cm}^{-1}$. The low-temperature gradient implies temperature increases at a slower rate with depth. This could be due to the presence of cold fluids within the subsurface. For instance, water from Lake Elmenteita in the Northeast of the study area could be seeping down, resulting in a low-temperature gradient. Also, a low-temperature gradient could be caused by a geothermal reservoir usually surrounded by cooler rocks that are hydraulically connected to the cold mass of water. This water may flow to the heat source, get heated, and then be trapped within the Earth's subsurface to form a geothermal reservoir. This system usually acts as a recharge to the geothermal reservoir. The high-temperature gradient implies temperature increases at a higher rate with depth toward the possible heat sources at deep depths. Figure 4.4 shows a high-temperature gradient towards the central-southern part of the study area, which is above the normal conductive gradient of $0.03\,°\mathrm{Cm}^{-1}$ (Mburu, 2006; Mwawongo, 2013). It cuts through the Eburru settlement scheme towards OlDoinyo Opuru. This area is considered thermally active and was modelled using gravity and magnetic data to image the underlying rock structures. Modelling was also done in some low-temperature gradient areas to image the possible geothermal reservoir recharge structures.

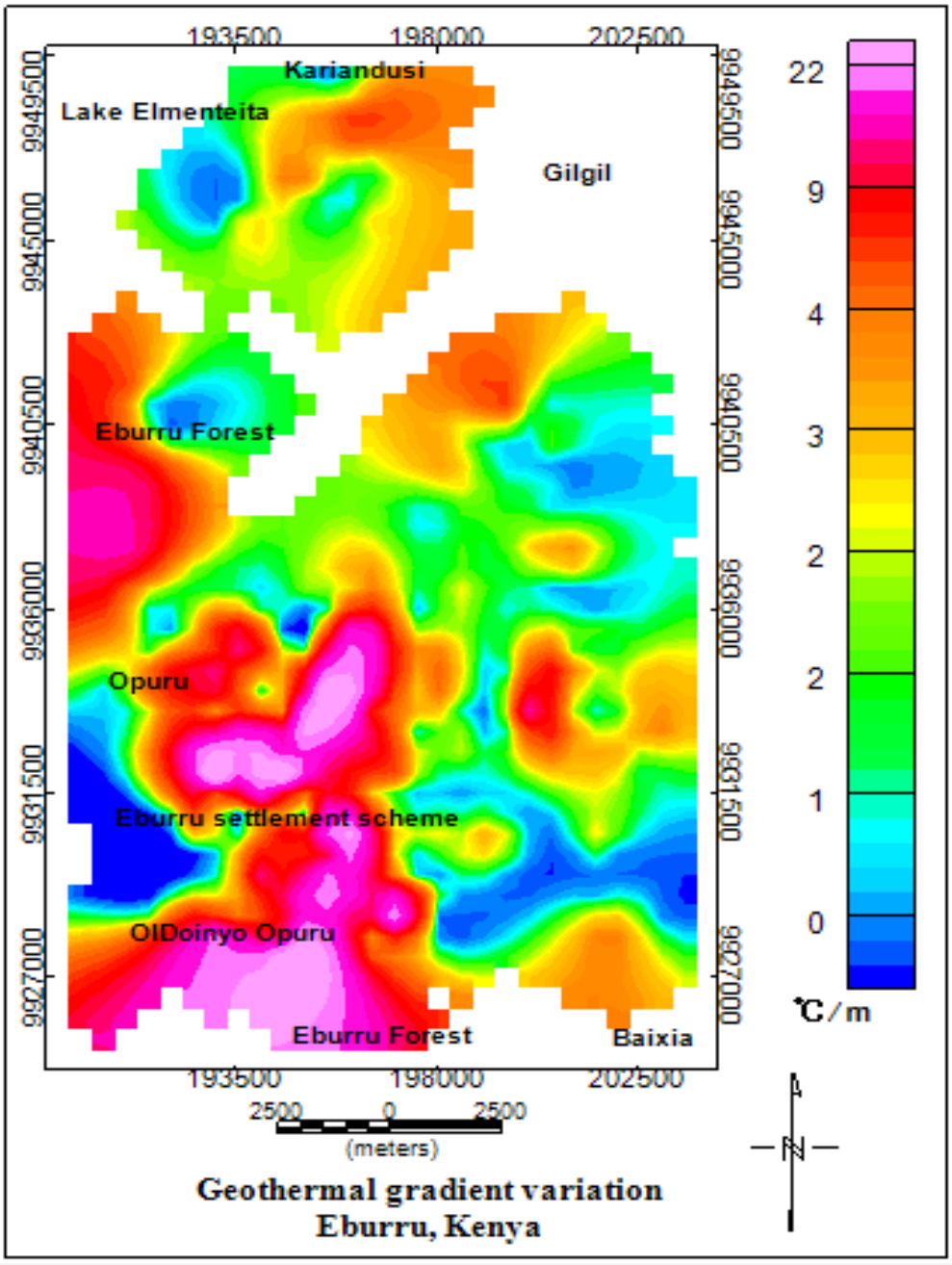

Figure 4.4: Geothermal gradient distribution map

Figure 4.5 shows the heat flux contour map for Eburru study area in Kenya. Heat flux values range from a minimum of 0.02 W/m^2 to a maximum of 92.8 W/m^2. The mean heat flux was determined to be 10.06 W/m^2. Heat flux is the rate of heat flow per unit

area. Heat flow is associated with heat loss within the study area. The region with high heat flux indicates high heat loss. High heat loss implies a good heat transfer mechanism to the surface. This means enough energy may be trapped at accessible depths in the Earth's crust hence could be a geothermal heat source. From Figure 4.5, there are areas with elevated heat loss, indicating that the geothermal heat source could be within the accessible depths that can be accessed for geothermal resource development. The high heat flux area is mapped to the Southern part of the study area through the Eburru settlement scheme towards Oldoinyo Opuru. The Figure also shows areas with decreased heat loss which may be due to poor heat transfer mechanism to near-surface or deep heat sources. These areas are oriented in a North-South direction. Gravity and magnetic data shown in Figure 3.10 and Figure 3.11 was modelled in these areas to image and characterize the causative structures. From Figure 4.5, the Southern parts indicate high heat flux areas; hence were modelled using gravity and magnetic data. Generally, there is a North-South trend in the heat flux variation, possibly due to a North-South rock structure in the area.

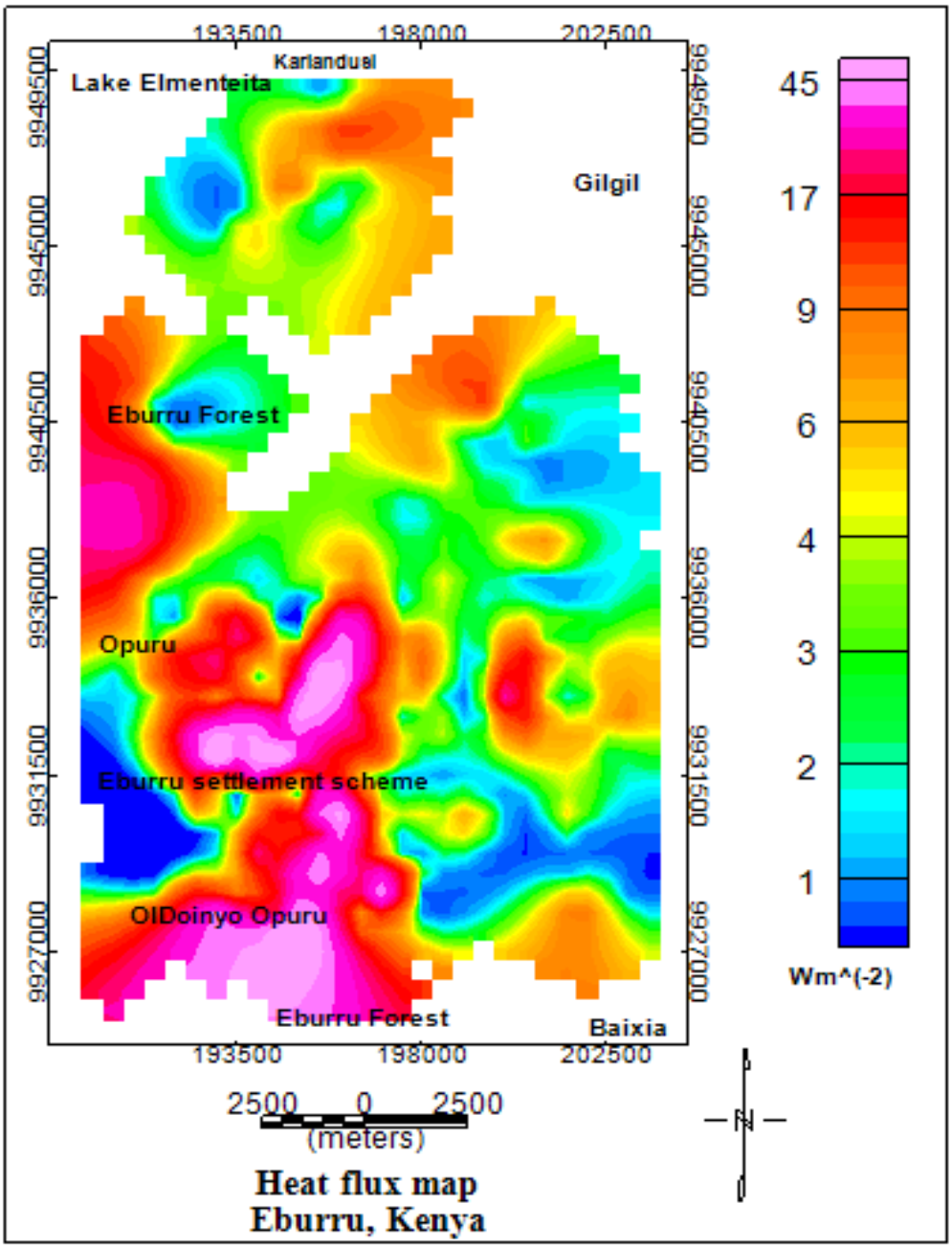

Figure 4.5: Heat flux contour map

4.3 Gravity results and interpretation

4.3.1 Gravity data stations

Gravity data was collected based on heat flux results in the study area. The gravity station spacing was 500 m apart and distributed as shown in Figure 4.6.

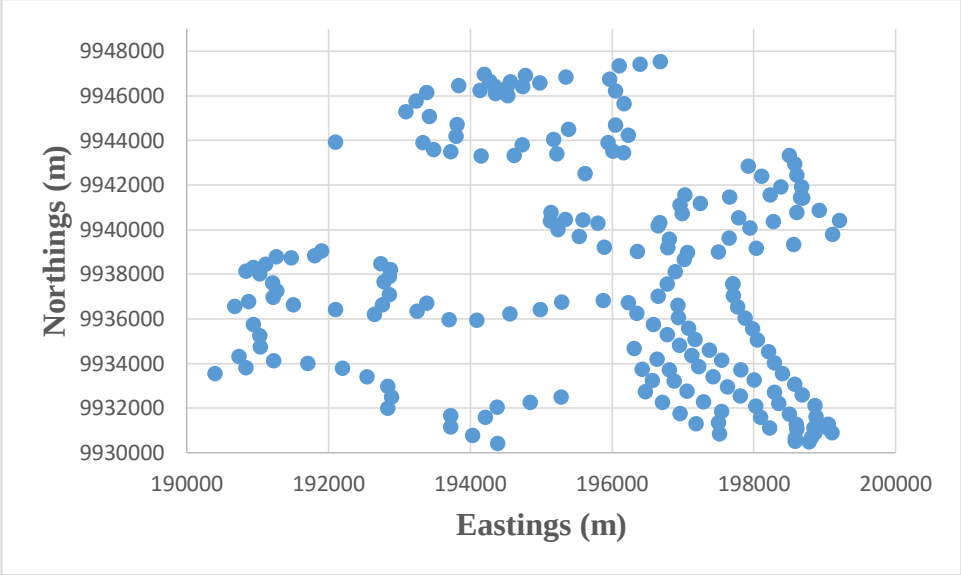

Figure 4.6: Distribution of gravity stations

4.3.2 Bouguer density

Nettleton's method was used to estimate the average density of crustal rocks between the observation point and the geoid in the study area. It is an indirect method that attempts to correlate the relationship between the Bouguer anomaly and height above the geoid. A profile was plotted in a North-South direction (Figure 4.7) as the structures in the Eburru study area show a trend in this direction. Bouguer anomaly was calculated using different densities, as shown in Figure 4.8. A density of 2.67 gcm^{-3} show the least correlation between the Bouguer anomaly (Figure 4.8) and the topography of the area (Figure 4.9). This means that the average crustal density of

rocks between the observation point and the geoid is 2.67 gcm^{-3}. This was further justified by the average density of the rocks between the Earth's surface and the geoid in the Earth's crust and was used for Bouguer correction (Hinze, 2003).

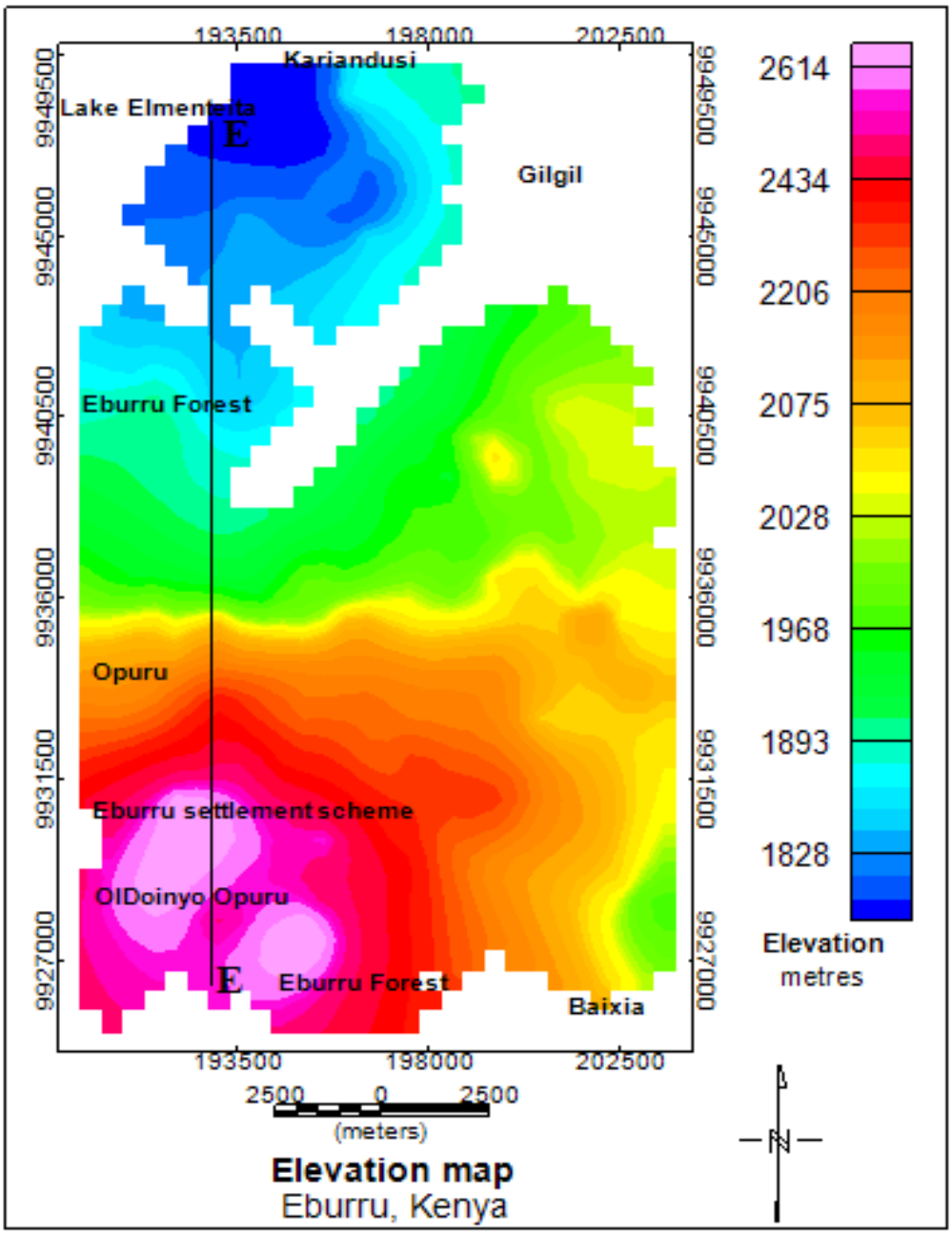

Figure 4.7: Profile EE on elevation map for average crustal density determination

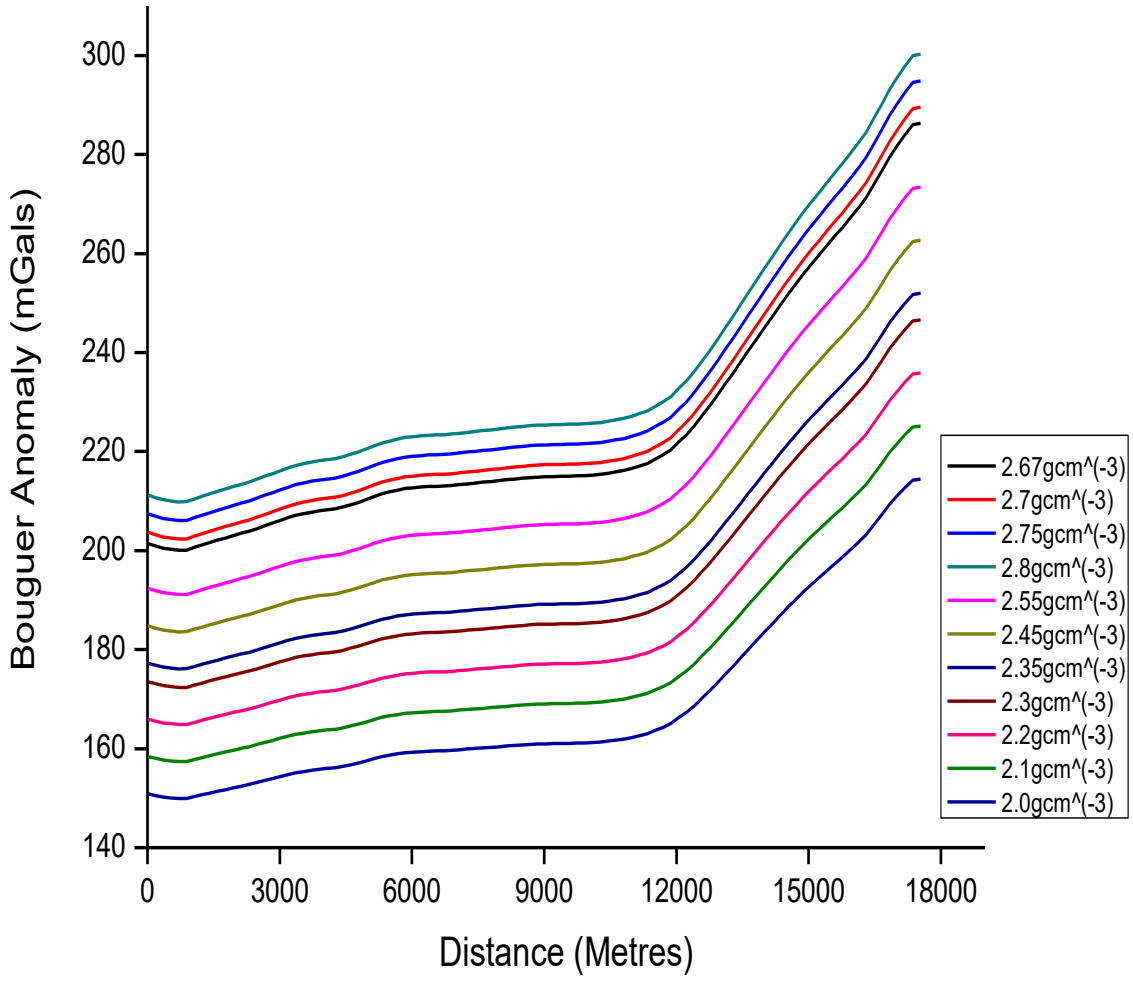

Figure 4.8: Bouguer anomalies along Profile EE.

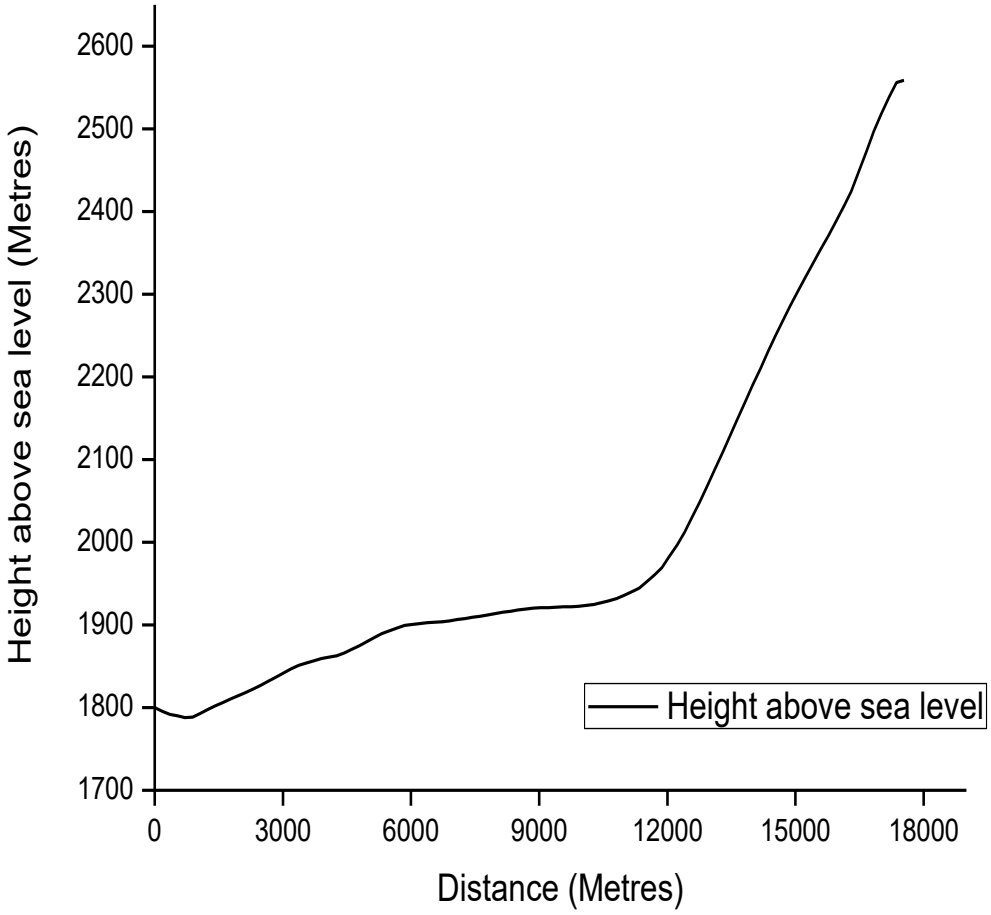

Figure 4.9: Cross-section showing topography along profile EE.

4.3.3 Complete Bouguer anomaly (CBA

Complete Bouguer anomaly (CBA) was calculated after the gravity corrections were done on the collected raw gravity data. The complete Bouguer anomaly would be zero if the density of rocks in the Earth's crust was constant, which was not the case.

Figure 4.10 shows a complete Bouguer anomaly map for the Eburru study area. The CBA values range from a gravity high of -269.50 mGal to a gravity low of -290.17 mGal. The variation of density in the underlying rocks within the Earth's crust results in a very small change in the Earth's gravitational field. This generates the Earth's gravitational field variation, leading to gravity anomaly (Kearey et al., 2002). In this study area, there is a 20.67 mGal gravity anomaly variation in the Earth's gravitational field between the highest density causative material and lowest density causative material.

The qualitative interpretation was attempted using the CBA map in Figure 4.10, which entailed a visual inspection of the map to identify areas of gravity highs and gravity lows. This reveals the variation in the density of underlying masses. Gravity high indicates denser underlying masses, while gravity low implies the presence of less dense masses than host materials in the Earth's crust.

Northern parts of the study area towards Lake Elmenteita show a high gravity region with small sections of gravity lows. There is a high gravity region in the central part of the study area bounded by coordinates (194200, 9944700) and (193300, 9936800). It is oriented in a Northeast - South direction with an average CBA of -280 mGal. This gravity high separates a gravity low, possibly indicating a fault (Yehuwalashet & Malehmir, 2018). Eastern parts of the map show a low anomaly and a high anomaly to the west. To the Southern part, there is generally a low gravity region bounded by coordinates (193500, 9934000) and (192500, 9929500) oriented in a North-South direction with some few spots of gravity highs. These gravity highs could be dykes in the form of high-density materials intruding from the mantle. To the Northeast, the map reveals gravity highs with few gravity lows. An intruding mass from the mantle has a density range of $2.7\ \mathrm{gcm}^{-3} - 3.2\ \mathrm{gcm}^{-3}$ which is a positive anomaly (Kearey et al., 2002). The heat source could be identified with a positive gravity anomaly as masses intruding are denser. The temperature of the Earth increases from the Earth's

surface towards its interior, and therefore intruding materials from the mantle have an elevated temperature. Due to the temperature gradient, there is continuous heat flow towards the Earth's crust through the intruding materials. Therefore, regions with high gravity anomaly imply denser masses in the Earth's crust which could be heat sources.

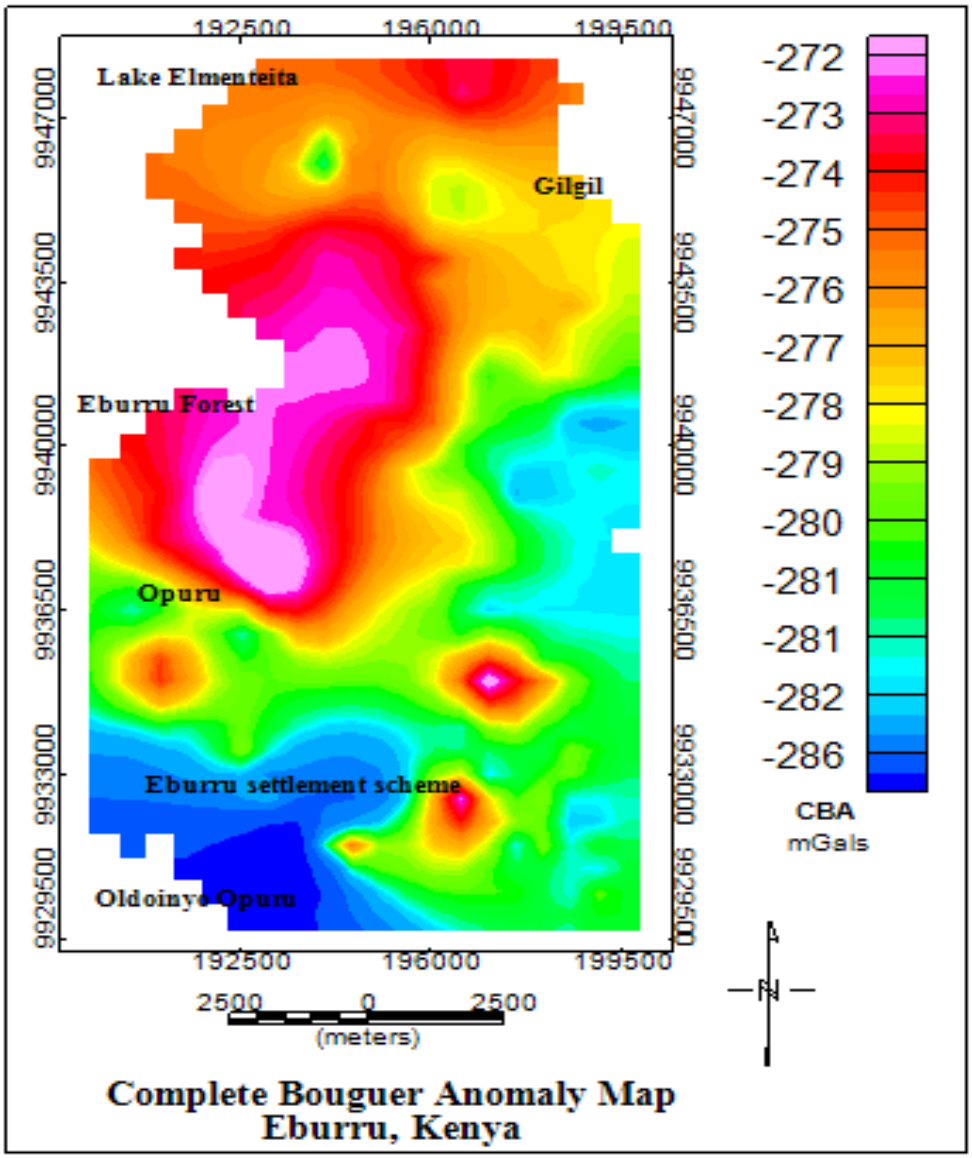

Figure 4.10: Complete Bouguer Anomaly Map for Eburru study area

4.3.4 Residual Bouguer anomaly

Residual Bouguer anomaly is the effect of density variation of near-surface masses of interest. Geothermal wells are typically done to approximately 3000 m depth (World Energy Council, 2013); hence deep heat sources beyond 10000 m may not be of interest. Shallow masses less than 500 m in depth increase the amplitude of gravity anomaly due to their short wavelength and high frequency thus generating noise to the result. Shallow masses are not of interest as geothermal heat cannot be trapped at these depths because elevated temperatures and pressure will erupt to the Earth's surface. Therefore, in this study, the effect of shallow masses less than 500 m depth and deep masses beyond 10000 m depth were removed to enhance features of interest between the bandpass. This was done by applying a bandpass filter in Oasis Montaj geosoft software by placing long-wavelength cutoff in-ground units at 10000 m and short-wavelength cutoff in-ground units at 500 m.

Figure 4.11 shows a residual anomaly map. The effect on the Earth's gravitational field from masses deeper than 10000 m and shallow masses less than 500 m depth was removed from the complete Bouguer anomaly. The Figure displays the enhanced effect of mass distribution between 500 m and 10000 m depth bandpass within the Earth's subsurface. It displays a series of positive and negative gravity anomalies. The residual gravity anomaly amplitude ranges from the highest at 5.34 mGal to the lowest at -4.65 mGal. This shows that the study area has alternating high and low densities masses. There is a large positive gravity anomaly at the central part of the study area between coordinates (194400, 9945000) and (193000, 9936500) in the Eburru Forest and Opuru area. This could be due to a series of intruding masses from the mantle into the Earth's subsurface with higher density than the host rocks in the Earth's crust. Also, a large negative gravity anomaly is bounded by the coordinates (198400, 9941600) and (192700, 9929600) in the Eburru settlement scheme towards the South of the study area. This results in the observed positive and negative gravity anomalies.

This also possibly indicates the presence of underground faults and fractures that direct hydrothermal fluids' movement in this study area.

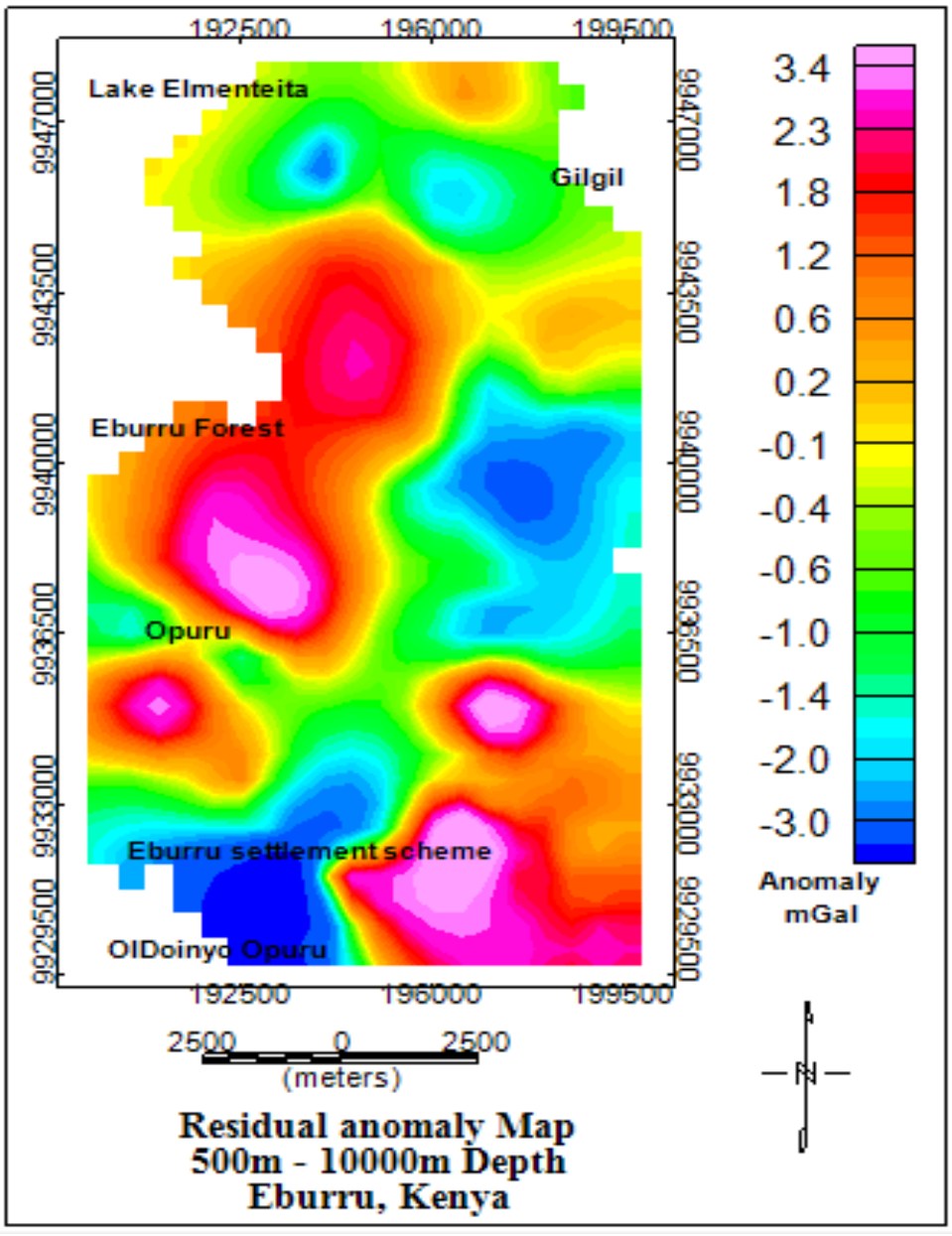

Figure 4.11: Residual gravity anomaly map

4.3.5 Euler deconvolution results.

A structural index of 0.5 generally indicates ribbon-like structures, thus implying either a fault or sill-like structure in the locations with estimated depths, as shown in appendix IV. The structural index of 0.5 generated five solutions at a depth range of 433 m – 2271 m occurring on gravity highs, as displayed in Figure 4.12. The Figure exhibits the deepest Euler solution 5 occurring in the North of the study area at a depth of 2271 m on a gravity high with an amplitude of 5.34 mGal. These could be hot dense materials from the mantle trapped at this depth in the Earth's crust. The shallowest Euler solution 1 occurs in the South of the study area at a depth of 433 m also on a high gravity amplitude of 5.34 mGal. The depth is shallow because the solution occurs towards the Eburru crater, where dense materials appear to have been pushed from the mantle until they came out of the surface in form of a lava flow.

The structural index of 1.0 indicates pipe-like structures, implying a dyke intrusive in the locations, as shown in appendix IV. These intrusives may be emanating from either a batholith structure at deep depths in the Earth's crust or directly from the Earth's mantle. Usually, they are hot dense bodies explaining their upward movement. This structural index of 1.0 generated five solutions at a depth range of 801 m – 1433 m occurring on gravity highs, as displayed in Figure 4.13. The Figure exhibits solution 5, the deepest Euler solution occurring in the North of the study area at a depth of 1434 m on a high gravity amplitude of 2.3 mGal. Deeper anomaly sources have large wavelengths with small signal amplitude, indicating reduced energies. These could be hot dense materials in the geological shape of a pipe from the mantle trapped at this perpendicular distance in the Earth's crust. Solution 1 is the shallowest Euler solution which occurs to the South of the study area at a depth of 801m on a high gravity amplitude of 3.4 mGal.

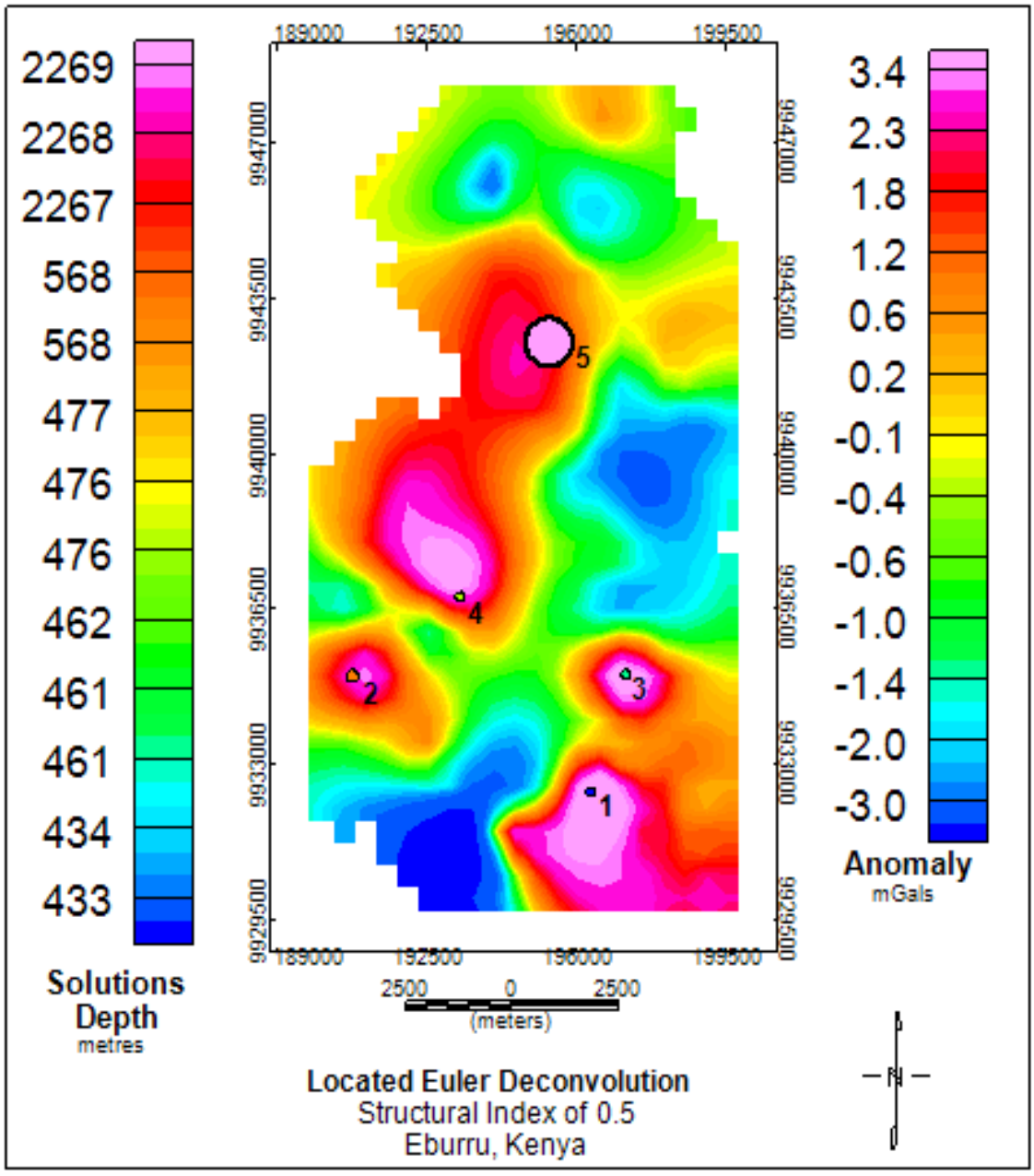

Figure 4.12: Euler deconvolution results for a structural index of 0.5

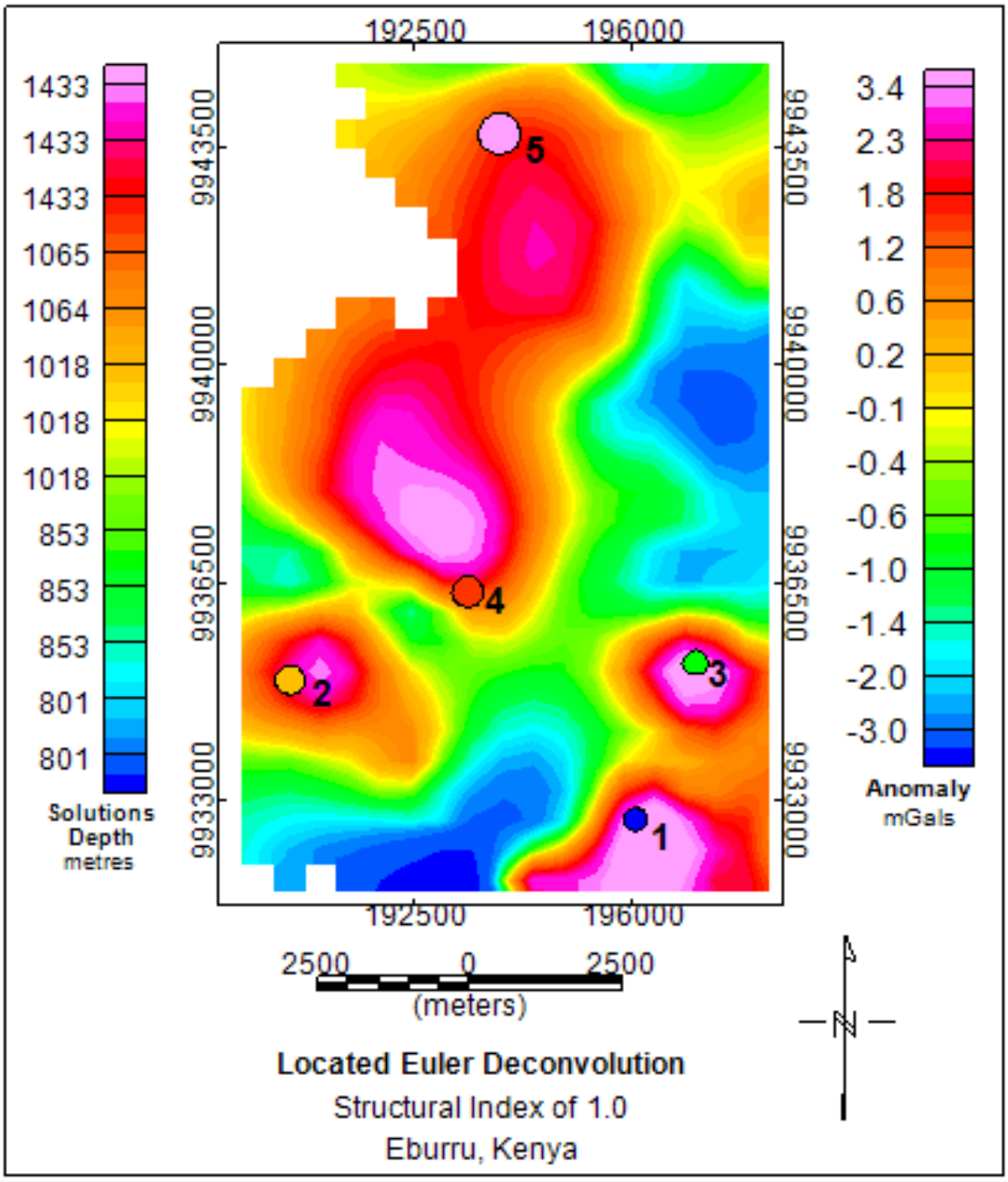

Figure 4.13: Euler deconvolution results for a structural index of 1.0

4.4 Magnetic results and interpretation

4.4.1 Magnetic data stations

Magnetic data stations were established based on heat flux results in the study area. Figure 4.14 shows the distribution of magnetic data points in the study area with a station spacing of 500 m.

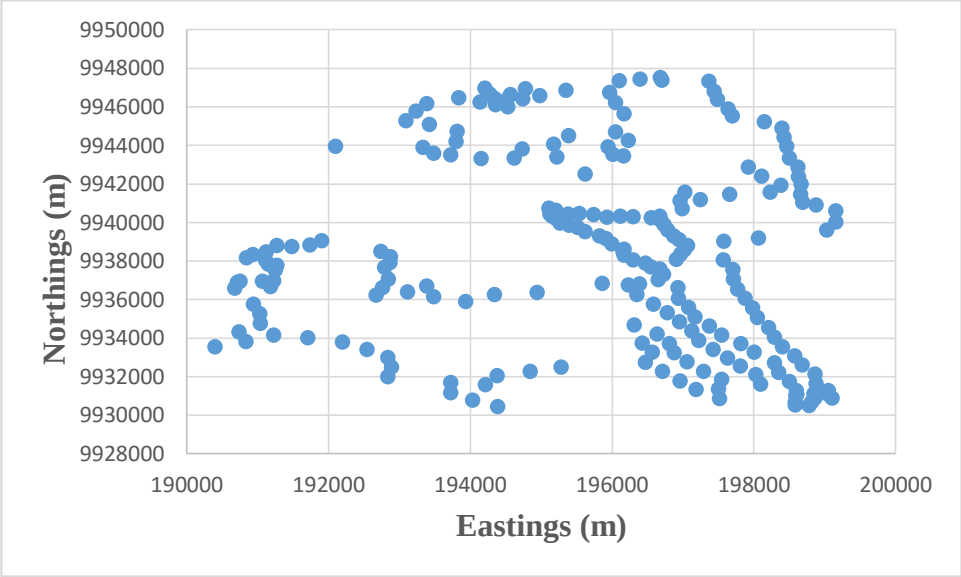

Figure 4.14: Distribution of magnetic stations

4.4.2 Residual magnetic anomaly

Figure 4.15 shows the residual magnetic anomaly map between 500 m and 10000 m bandpass depth. It was obtained after geomagnetic and diurnal corrections were applied to the raw magnetic data. Residual magnetic anomaly is due to the effect on the Earth's magnetic field by the masses present between the bandpass indicated. The Figure images the distribution of negative and positive magnetic anomaly poles within the study area. To the Northern parts of the study area, there is a positive pole end and a negative pole end indicating a body or structure oriented in a North-South direction.

These could be intruding masses from either the Earth's mantle or from a batholith structure at deep depths towards the Earth's subsurface. It is interpreted as deep because it has a longer wavelength with a shorter amplitude. At the centre of the study area towards Opuru and the Southeast part of the study area, there is a positive pole and a negative pole indicating a body or structure oriented in a North-South direction. Generally, the residual magnetic anomaly map in Figure 4.15 shows a North-South trend of magnetic anomalies implying the area has an underlying structure in this direction. This structure could be faults and fractures oriented in a North-South direction within the Earth's subsurface.

In a geothermal environment, a magnetic anomaly with high magnetic amplitude is considered basic igneous masses of high magnetic susceptibility intruding the Earth's crust. These masses probably do not have elevated temperatures because they do not have reduced magnetic susceptibility and hence may not be geothermal heat sources. Low magnetic anomaly identified by low magnetic amplitude is interpreted to be caused by hydrothermal demagnetisation of masses by hot geothermal fluids or demagnetisation due to high temperatures of the intrusive. This indicates that there are fluid channels such as faults and fractures within the Earth's subsurface that allow geothermal fluids' movement. Furthermore, a magnetic anomaly with low magnetic amplitude indicates basic igneous intrusions in the Earth's subsurface that have reduced magnetic susceptibility. These anomalies suggest low magnetic susceptibility materials due to high temperatures; hence could be possible geothermal heat sources. Therefore, low magnetic amplitudes are sites of interest when locating heat sources. The residual magnetic anomaly map in Figure 4.15 reveals massive basic igneous intrusions in the form of dykes and sills within the Earth's subsurface, indicating recent volcanic activity. The Figure also images the presence of underground conduits that influence fluid movement beneath the Earth's surface, which is paramount in characterizing a geothermal resource. This enables surface and underground water to reach heat sources and gets heated to form a geothermal reservoir. The availability of

these conduits within the study area also reveals a lot of underground convectional movement of hot fluids shown by reduced magnetic susceptibility. These hot fluids may be trapped at a depth to form a geothermal reservoir.

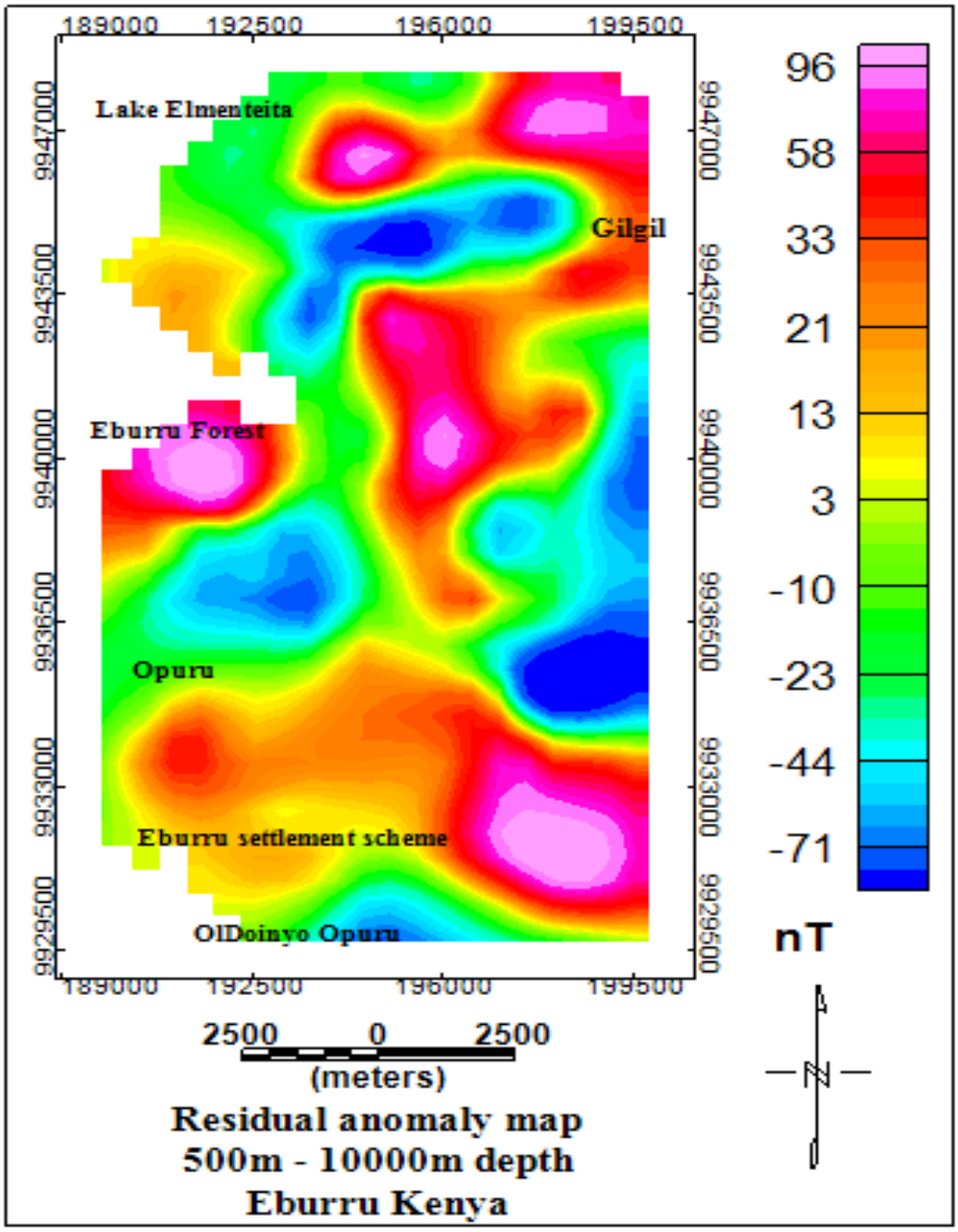

Figure 4.15: Residual magnetic anomaly map

4.4.3 Euler deconvolution results

A structural index of 0.5 generally indicates a thick step structure, as shown in appendix IV. It generated four solutions at a depth range of 1090 m to 1546 m, as displayed in Figure 4.16. Solution 1, shown in the Figure, is the deepest and occurs at approximately 1546 m depth to the South of the study area. It occurs on a positive magnetic anomaly pole indicating massive basic igneous intrusive. Solution 4 is the shallowest and occurs at approximately 1090 m depth to the North of the study area on a negative magnetic anomaly pole. Solutions 2 and 3 in Figure 4.16 occur between a magnetic anomaly's positive and negative poles. This could be basic igneous intrusive within the Earth's subsurface. There is a region of low magnetic amplitude between the solution locations, indicating the possibility of the occurrence of high-temperature masses.

Figure 4.17 shows Euler deconvolution results for the structural index of 1.0. A structural index of 1.0 is associated with a sill or dyke like geological shape in the Earth's crust, as shown in appendix IV. It generated five solutions at a depth range of 1655 m to 2355 m. Solution 1 as shown in Figure 4.17 is the deepest and occurs at a depth of approximately 2355 m to the South of the study area. This could be a basic igneous intrusion in the form of a sill or dyke with high magnetic susceptibility. Solution 4 is the shallowest and occurs at a depth of approximately 1655 m to the West of the study area. Solutions 2, 3, and 5 appear on negative magnetic anomaly poles at depths of about 2115 m, 2209 m, and 1842 m, respectively.

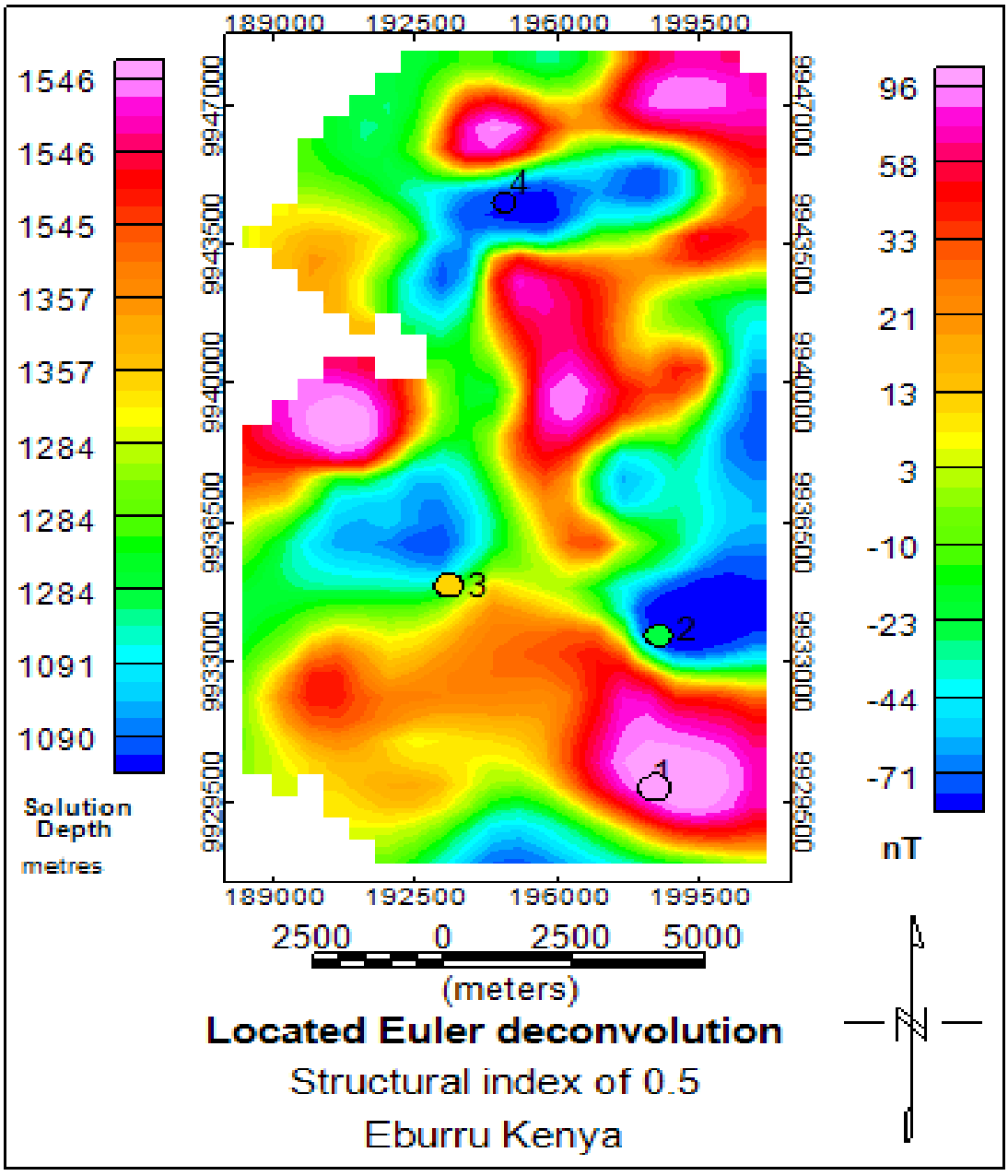

Figure 4.16: Euler deconvolution results for a structural index of 0.5

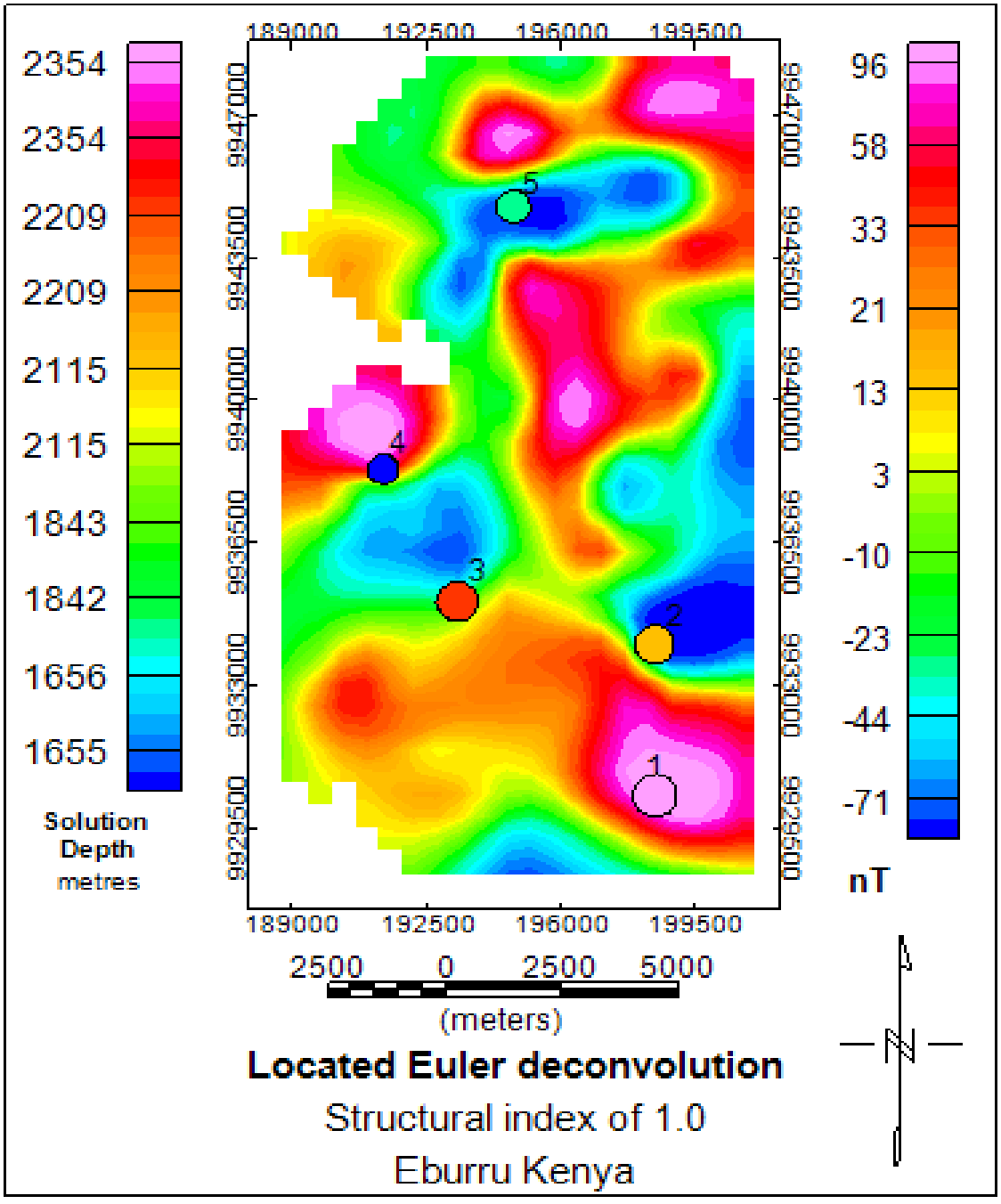

Figure 4.17: Euler deconvolution results for a structural index of 1.0

Figure 4.18 shows Euler deconvolution results for a structural index of 2.0. A structural index of 2.0 indicates a pipe-like geological shape in the Earth's crust as shown in appendix IV. It generated four solutions at a depth range of 3186 m – 3973 m. Solution 1 in Figure 4.18 is the deepest and occurs at a depth of approximately 3972 m on a positive magnetic anomaly pole to the South-East of the study area. This could be due to pipe-like basic igneous intrusive of higher magnetic susceptibility than the host rocks. Solution 3 is the shallowest and occurs at approximately 3186 m depth. Solution 3 occurs between a positive magnetic anomaly pole and a negative magnetic anomaly pole indicating a high magnetic susceptibility body. Solutions 2 and 4 occur on a negative magnetic anomaly pole at depths of approximately 3778 m and 3346 m, respectively. These could be a pipe-like basic igneous intrusive from the mantle or batholith structure at deep depths. Generally, the high positive and negative amplitude shown is probably due to shallow structures with high magnetic susceptibility, while the low amplitude could be due to deep structures.

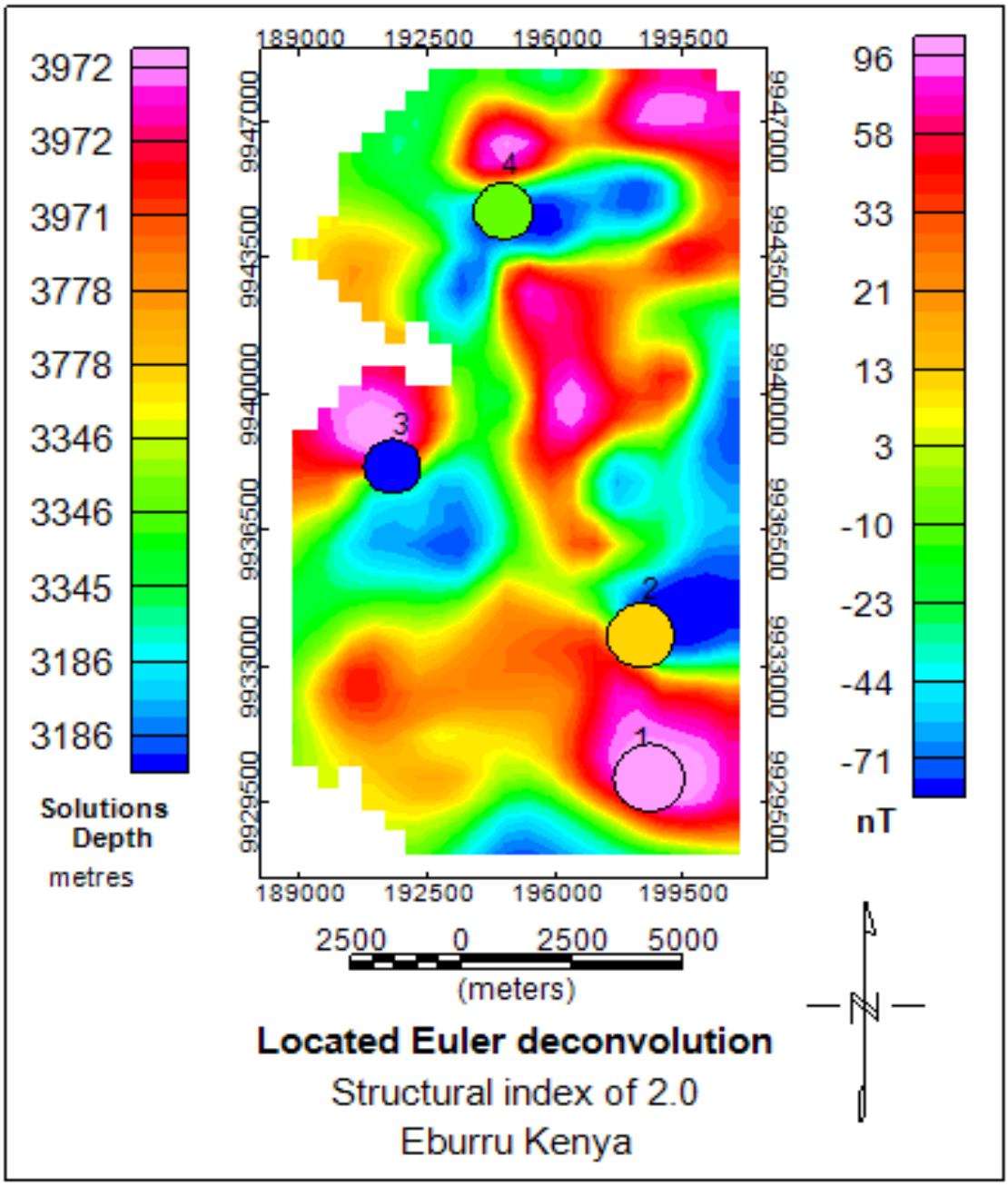

Figure 4.18: Euler deconvolution results for a structural index of 2.0

4.4.4 Spectral analysis of ground magnetic data

The study area was taken as one block and radially averaged energy spectrum produced because isotherm depth involves imaging of deeper structures. The radially averaged energy spectrum was a function of wavenumber only. It was determined by averaging the energy for all directions for the same wavenumber. Wavenumber, k was the spatial frequency of a wave measured in cycles per unit distance. The Nyquist wavenumber, N, was the largest wavenumber sampled by the grid, which was the highest frequency possible to measure given a fixed sample interval. Applying equation 2.27, N was given as

$$N = \frac{1}{2\times d} = \frac{1}{2\times 0.5} = 1$$

Where d is the sample interval.

Wavenumber, k ranges between 0 and 1, as shown in Figure 4.19. The Nyquist frequency was 1. The depth axis was in multiples of grid cell size, which was 0.5 km for this study. The depth of a statistical ensemble of sources was determined by equation 2.28. Where h was depth and s was the five-point average of the slope of the energy spectrum (Spector & Grant, 1970). There was a spectral peak between wavenumbers of $0\ \text{cycles/metre}$ and $0.0002\ \text{cycles/metre}$. This was due to contribution from deep-seated sources at a depth of approximately 1600 m from the depth estimate graph in Figure 4.19. The spectral peak between wavenumbers $0.0006\ \text{cycles/metre}$ and $0.0008\ \text{cycles/metre}$ was due to shallow near-surface sources contribution at a depth of approximately 250 m. From Figure 4.19,

Mean deep source depth $= 1.61$ km
Mean shallow source depth $= 0.25$ km

The basal depth z_b Which was assumed to be the curie point depth (Okubo et al., 1985), and was calculated using equation 2.29.

$$z_b = (1.61 \times 2) - 0.25$$
$$= 3.22 - 0.25$$
$$= 2.97 \text{ km} = 2970 \text{ m}$$

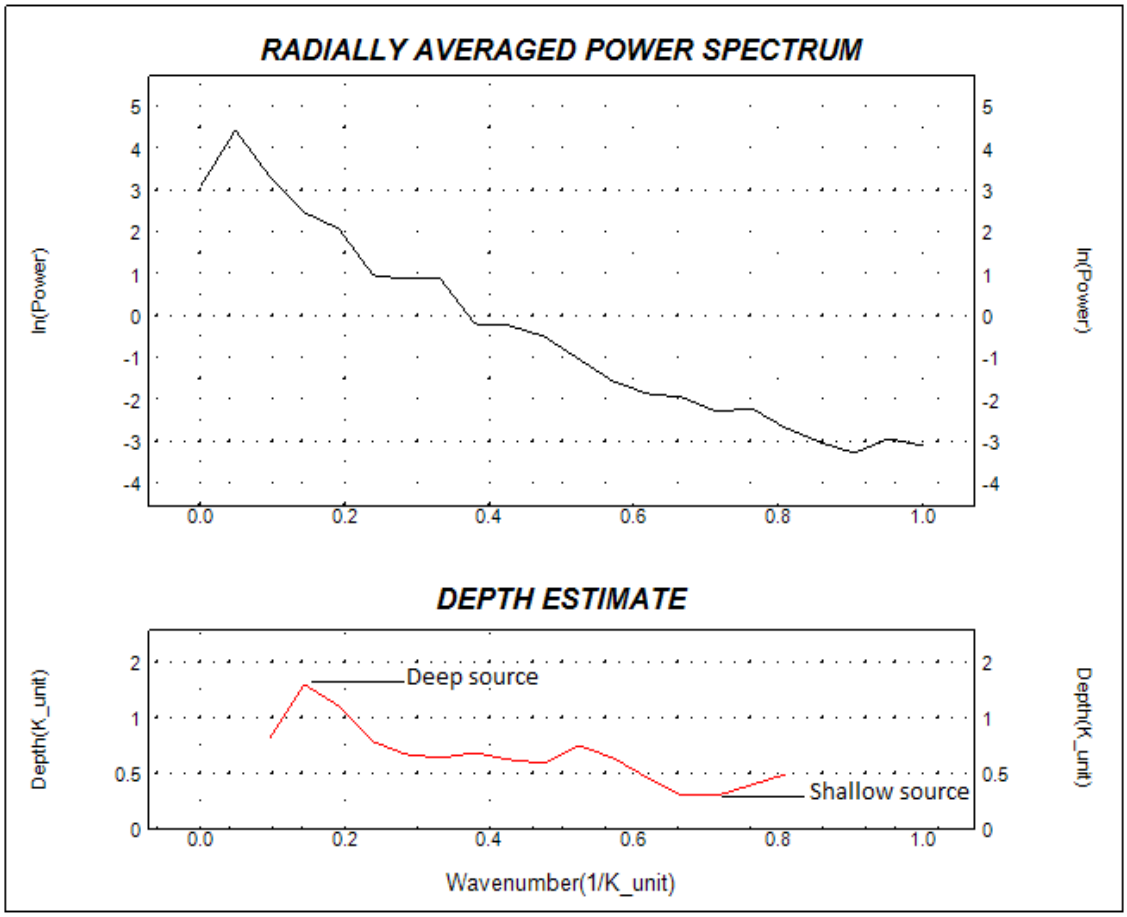

Figure 4.19: Spectral power distribution as a function of spatial frequencies

Therefore, the curie point isotherm depth for this study area was approximately 2970 m. Curie point isotherm depth is the depth at which magnetism of materials disappears due to high temperatures (Kearey et al., 2002). The temperature at which

materials cease to exhibit magnetic behaviour is called curie temperature. Minerals exhibit variation in curie temperatures, resulting in rocks having different curie point temperatures due to different minerals present in their composition. There is a high potential for a high-temperature geothermal heat source in this study area. If the curie point isotherm depth is approximately 2970 m, then the temperatures at this depth must be above 130 ℃ (Reynolds, 1998). For example, the curie temperature for titanomagnetite varies from 463 ℃ to 580 ℃ in an area occupied mainly by granite rhyolite rocks (Reynolds, 1998). For an area mostly occupied by ilmenite hematite rock, the Curie temperature varies from 130 ℃ to 220 ℃ (Reynolds, 1998).

Oxidation of iron titanium oxides which are abundant in the Earth's crust, usually causes an increase in curie temperature (Reynolds, 1998). The intensity of magnetisation reduces when oxidation occurs at lower temperatures for example, temperatures less than 300 ℃. Titanomagnetite converts to titanmagnemite, then finally to magnetite with a curie temperature range of 550 ℃ – 580 ℃ because of oxidation and decrease in intensity of magnetisation (Reynolds, 1998). In this study area, the temperature at curie point isotherm depth of approximately 2970 m could be in the range of 550 ℃ – 580 ℃ if complete oxidation took place to change titanomagnetite mineral to magnetite mineral. If complete oxidation did not occur, the curie point isotherm depth temperatures could be less than 550 ℃. Minerals are made up of atoms, and if these atoms are chemically stable, oxidation cannot occur.

Hematite has a very high curie temperature which ranges from 650 ℃ to 680 ℃ and the lowest intensity of magnetisation (Parasnis, 1986). In this study area, there is low magnetisation intensity which could be due to the alteration of high magnetic intensity minerals to hematite with the lowest intensity of magnetisation because of oxidation and hydrothermal alteration. These areas with high temperatures could be geothermal heat sources.

Spectral analysis of ground magnetic data in this study area estimated the geothermal isotherm depth at 2970 m which translated to a geothermal gradient of 0.19 ℃/m. The geothermal gradient of 0.19 ℃/m was arrived at by considering a temperature of 578 ℃, which is the curie temperature of magnetite (Telford et al., 1990). Magnetite was used as it is the most abundant magnetic material in the Earth's crust. From heat loss measurements, the average temperature gradient within 0.5 m depth and one-metre depth was determined to be 5.03 ℃/m which was far higher than the value from the spectral analysis of ground magnetic data. This means that the geothermal gradient was not constant and probably decreased with depth. This is because the geothermal gradient within the 1-metre depth and 0.5 m depth from heat flow measurements was 5.03 ℃/m which decreased to a mean of 0.19 ℃/m considering a depth of 2970 m from spectral analysis of ground magnetic data. This could be attributed to different layers of rocks within the Earth's crust with different heat transfer rates. Also, it could be that when the heat source is approached, the temperature of a hot mass of rock becomes constantly high hence decreasing the geothermal gradient. Possibly a permeable rock could explain this on top of a heat source which prevents heat transfer by conduction; thus, the geothermal gradient becomes constant when the heat source is approached. High geothermal gradient near the Earth's surface, which corresponds to high heat flux on the surface, is possibly due to either the hot body is near the surface, good heat transfer mechanism in the area from the heat source or the thinning of the Earth's crust due to continental rifting (World Energy Council, 2013). This study reveals a high heat flux area in the central-southern part of the study area in the Eburru settlement scheme to Oldoinyo Opuru.

4.5 Forward Modelling

Figure 4.20 shows selected profiles on a heat flux map for joint forward modelling of gravity and magnetic data shown in Figures 4.21 and 4.22. The profiles were selected based on heat flux values within the study area. They are cutting through high and low

heat flux areas. This was done to explain the relationship between heat flux values, density, and magnetic susceptibility for the area. High heat flux indicates an elevated geothermal gradient, while low heat flux indicates reduced heat at the Earth's surface. Forward modelling of gravity and magnetic data was done jointly along these profiles, as shown in Figure 4.21 and Figure 4.22, for correlation and image the possible causes of the observed heat flux values in the Earth's crust.

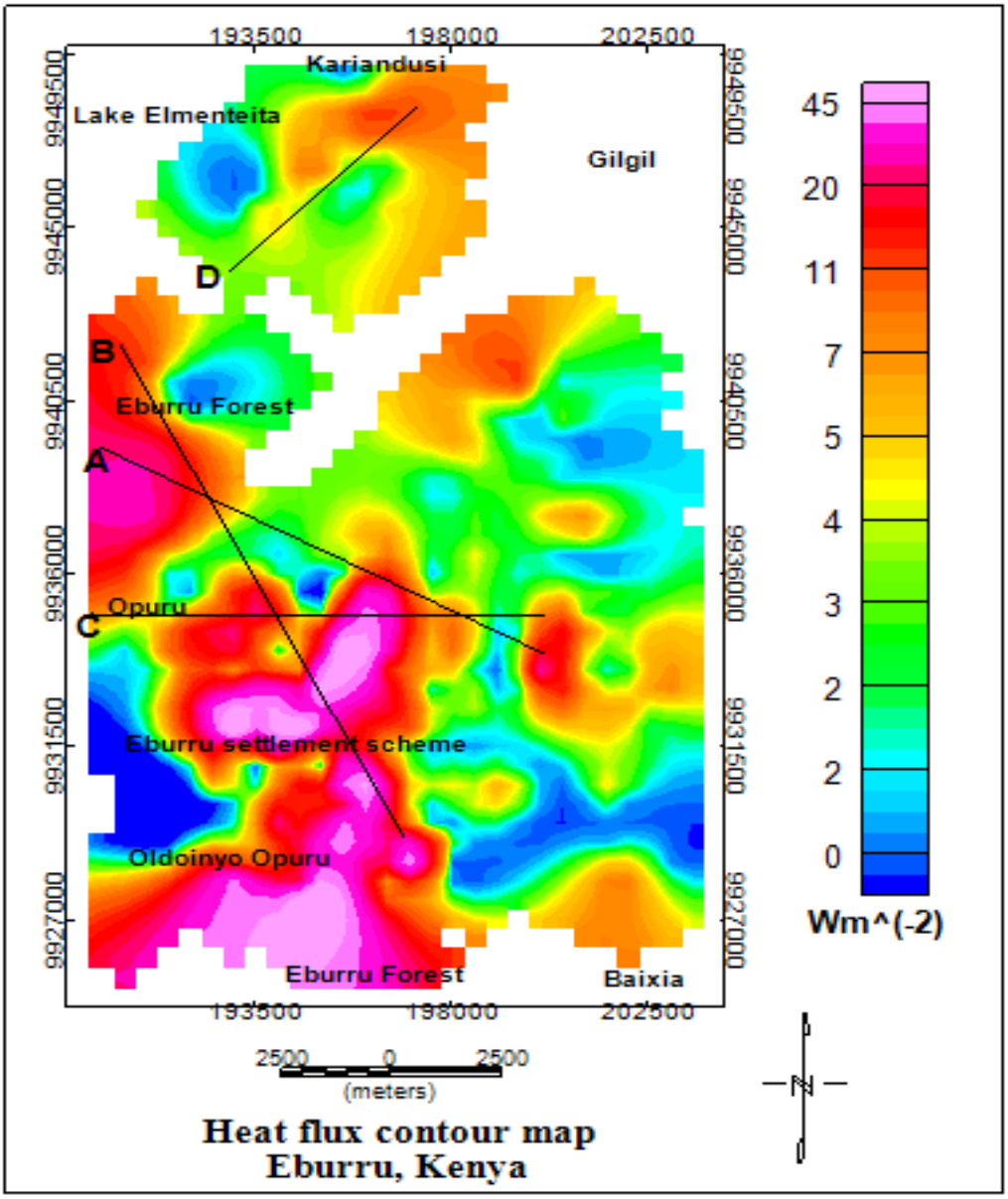

Figure 4.20: Heat flux map showing selected profiles for forward modelling

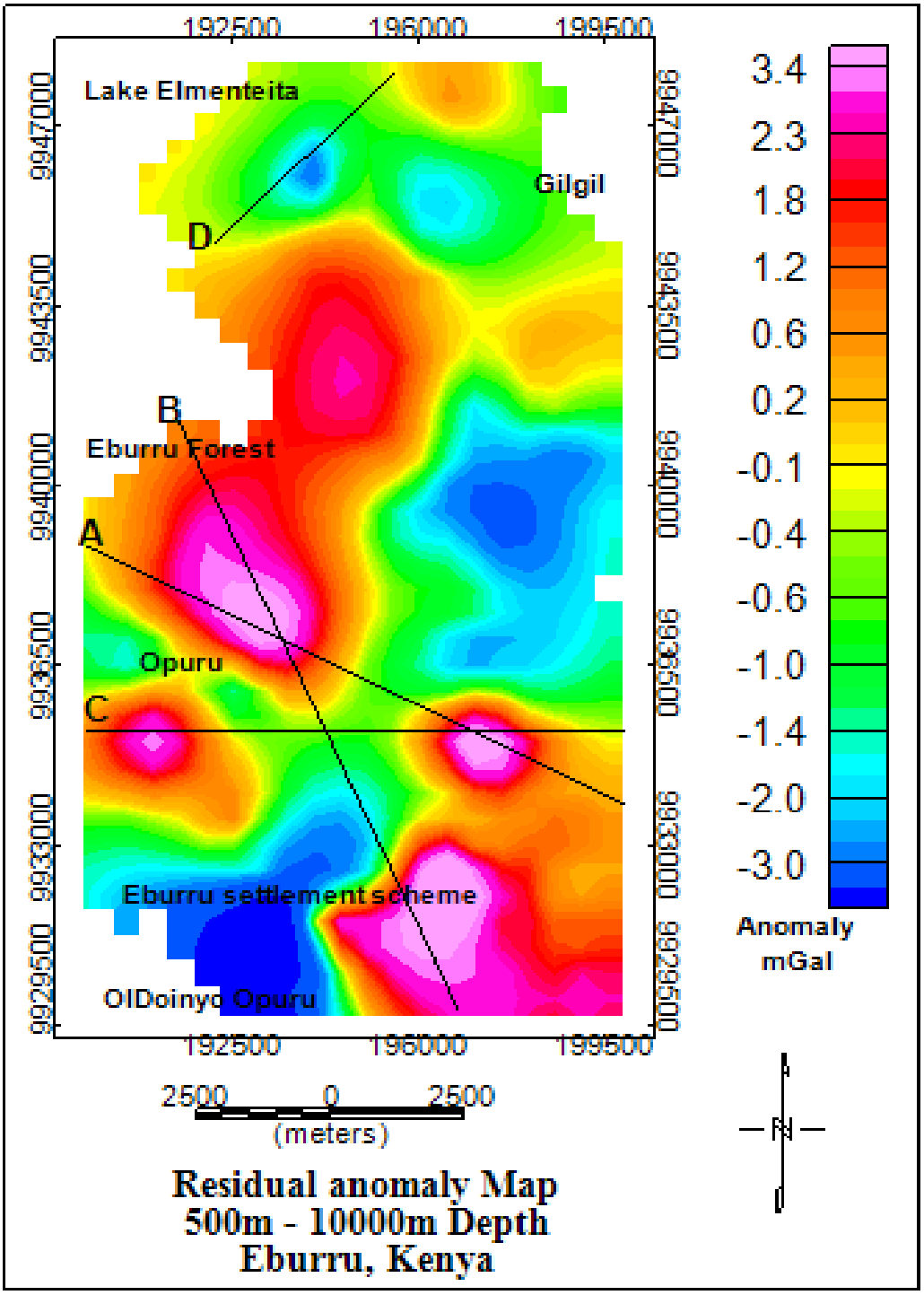

Figure 4.21: Gravity anomaly map showing selected profiles for forward modelling

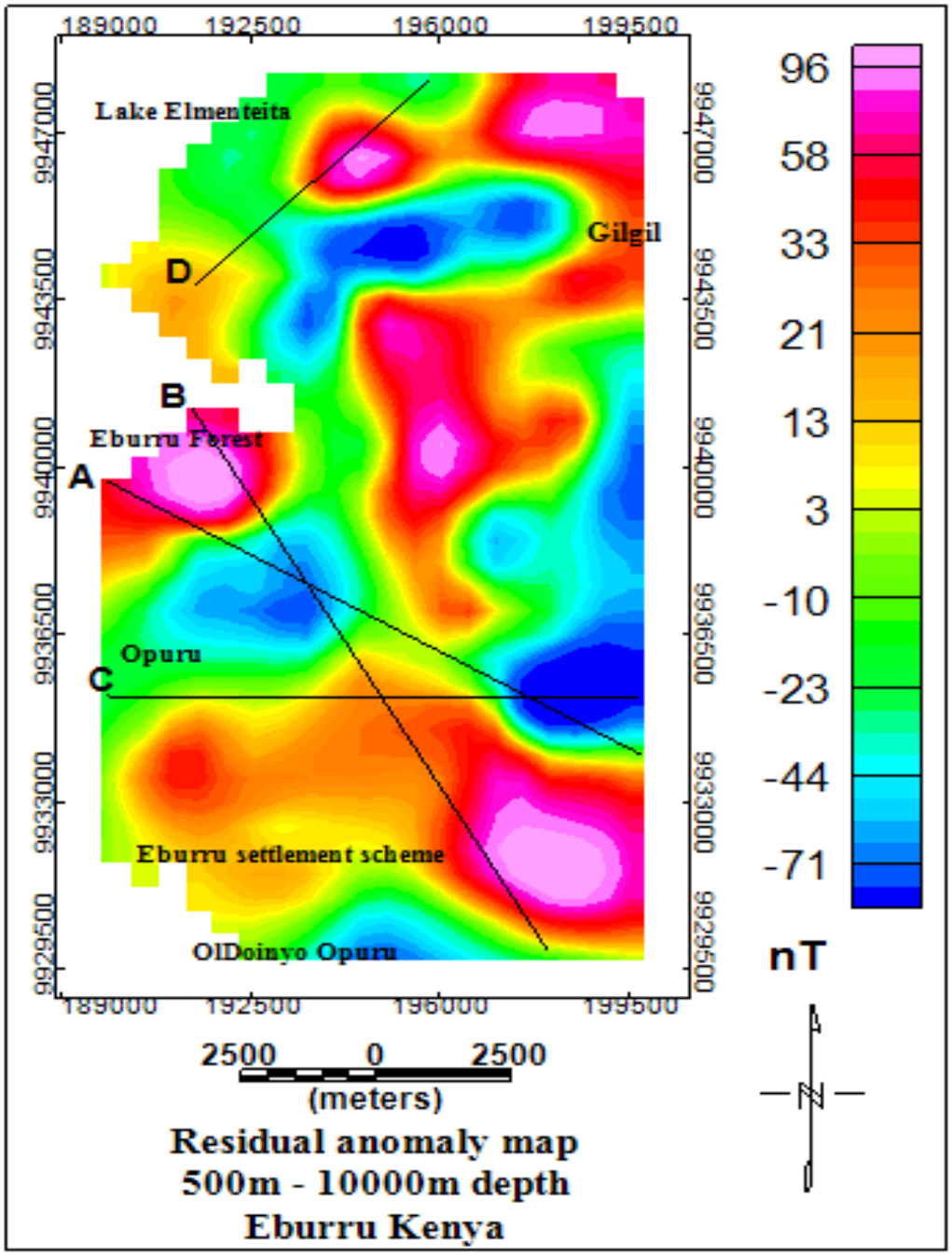

Figure 4.22: Magnetic anomaly map showing selected profiles for forward modelling

Figures 4.23, 4.24, 4.25, and 4.26 display the outcome of the calculated gravity and magnetic anomaly and its comparison with the observed residual anomaly. They also display the determined depth, density, and magnetic susceptibility of causative bodies. Interpretation of these models was based on the volcanic geology of the study area and its association with geothermal heat sources.

Figure 4.23 shows model A in the central part of the study area. Model A was constructed from profile A, as shown in gravity and magnetic anomaly maps in Figure 4.21 and Figure 4.22. It begins from a high heat flux region near Eburru Forest and trends in a Northwest-Southeast direction of the study area, as displayed in a heat flux map in Figure 4.20. It cuts across a high heat flux region in the middle and a low heat flux region to the Southeast part of the study area. Gravity and magnetic data were modelled jointly along this profile to image the possible underlying causative sources. The starting model was postulated from the Euler deconvolution depths. The model was constrained using stratigraphy data from the existing wells and the geology of the study area. The model revealed a first intrusion at a distance range of $6466\ \text{m} - 7009\ \text{m}$ along the profile, which was interpreted to be of basaltic rock origin at a depth range of $2248\ \text{m} - 2290\ \text{m}$. There is a second intrusive at a distance of $474\ \text{m} - 3302\ \text{m}$ along the profile occurring at a depth range of $3556\ \text{m} - 5187\ \text{m}$ deep, with a peak intrusion of $3556\ \text{m}$ deep occurring at $1905\ \text{m}$ along the profile. These intrusions are covered by a layer of less dense andesitic origin rock at $2145\ \text{m}$ deep. There are anomaly sources at the top interpreted to be trachyte, rhyolite, tuff, ignimbrites, and pyroclastic volcanic rocks origin as displayed in Figure 4.23. The intrusions have a density of $3.2\ \text{gcm}^{-3}$ and magnetic susceptibility of 0. Magnetic susceptibility of zero implies a high temperature at this depth that has destroyed the magnetism of the host rock (Telford et al., 1990). Considering magnetite, the most abundant magnetic rock within the Earth's crust, the temperature at this depth could be greater than $578\ ℃$ (Reynolds, 1998). Volcanic deposits near the surface showed a magnetic susceptibility range of $0.008\ \text{cgs} - 0.03\ \text{cgs}$ implying temperatures are

lower than the Curie point temperature. The variation of density and magnetic susceptibility images the Earth's subsurface faults and fractures that influence the movement of geothermal fluids. These intrusions were interpreted to be originating from a basement batholith and then intrude up in the form of dykes.

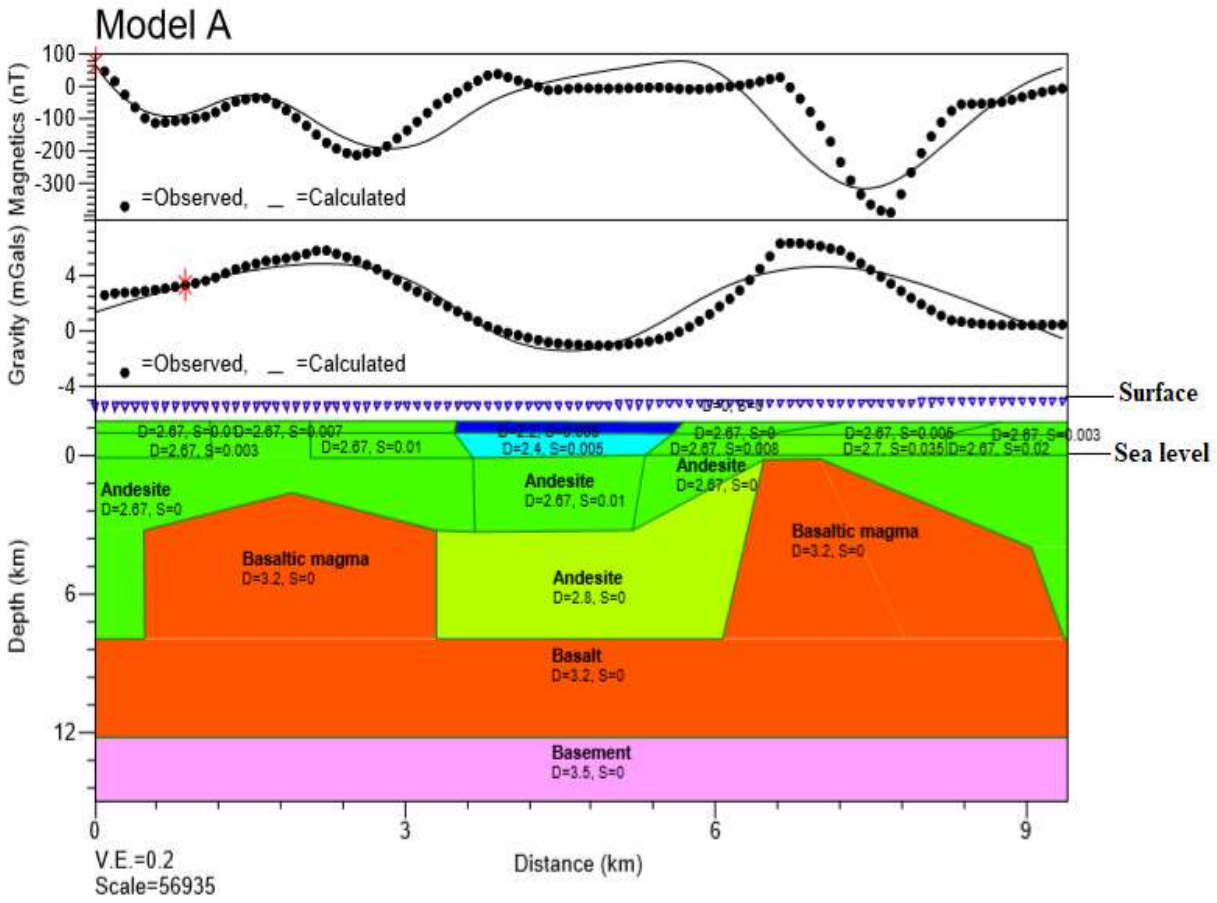

Figure 4.23: Model A constructed from profile A

Figure 4.24 shows model B constructed from profile B shown in gravity and magnetic anomaly maps in Figure 4.21 and Figure 4.22. Profile B runs in a Northwest-Southeast direction of the study area cutting through the Eburru settlement scheme to Oldoinyo Opuru in the South. The geothermal gradient is low in the Northwest part of the profile and becomes very high in the Southeast part of the profile, as shown in Figure 4.20.

The start model was postulated from Euler deconvolution depths. The model was later constrained during modelling based on stratigraphy data from existing wells and the geology of the study area. Model B reveals basaltic magmatic intrusions as shown in Figure 4.24. The first intrusion occurs at a distance range of $207\ \text{m} - 5177\ \text{m}$ along the profile with the depth to the top of the intrusion ranging between $1714\ \text{m} - 3160\ \text{m}$. The intrusion appears to be caused by hot magma rising from the mantle resulting in basaltic magma. The second intrusion occurs at a distance range of $9105\ \text{m} - 12144\ \text{m}$ along profile B, having a depth to the top of the source ranging between $1595\ \text{m} - 3521\ \text{m}$. The model in Figure 4.24 images shallow magma sources, possibly indicating rhyolitic magma due to basaltic-andesite magma releasing heat to the crustal rocks causing their melting. This generates new crustal magma that may be rich in silica and low iron content resulting in zero magnetic susceptibility or a reduction in magnetic susceptibility. The density of the anomaly sources was modelled to be $3.2\ \text{gcm}^{-3}$ which is higher than the crustal rocks' average density, indicating a high gravity. This shows that possibly the masses causing the gravity anomaly intruded from the mantle resulting in basaltic magma. The magnetic susceptibility of the intrusions was modelled to be zero. This implies the intrusions have higher temperatures that interfere with the magnetic properties of the rocks. The model shows the basaltic sources intruding between the andesitic rocks. The top layer was modelled to be a trachyte rock of density $2.67\ \text{gcm}^{-3}$ overlying the basalt intrusions and andesite. Trachyte is covered with a series of rhyolite, tuff, and pyroclastic volcanic materials with a density of $2.67\ \text{gcm}^{-3}$. The volcanic rocks at the top show magnetic susceptibility ranging between $0.001 - 0.009\ \text{c.g.s}$ units implying temperatures have dropped to the level of supporting magnetism.

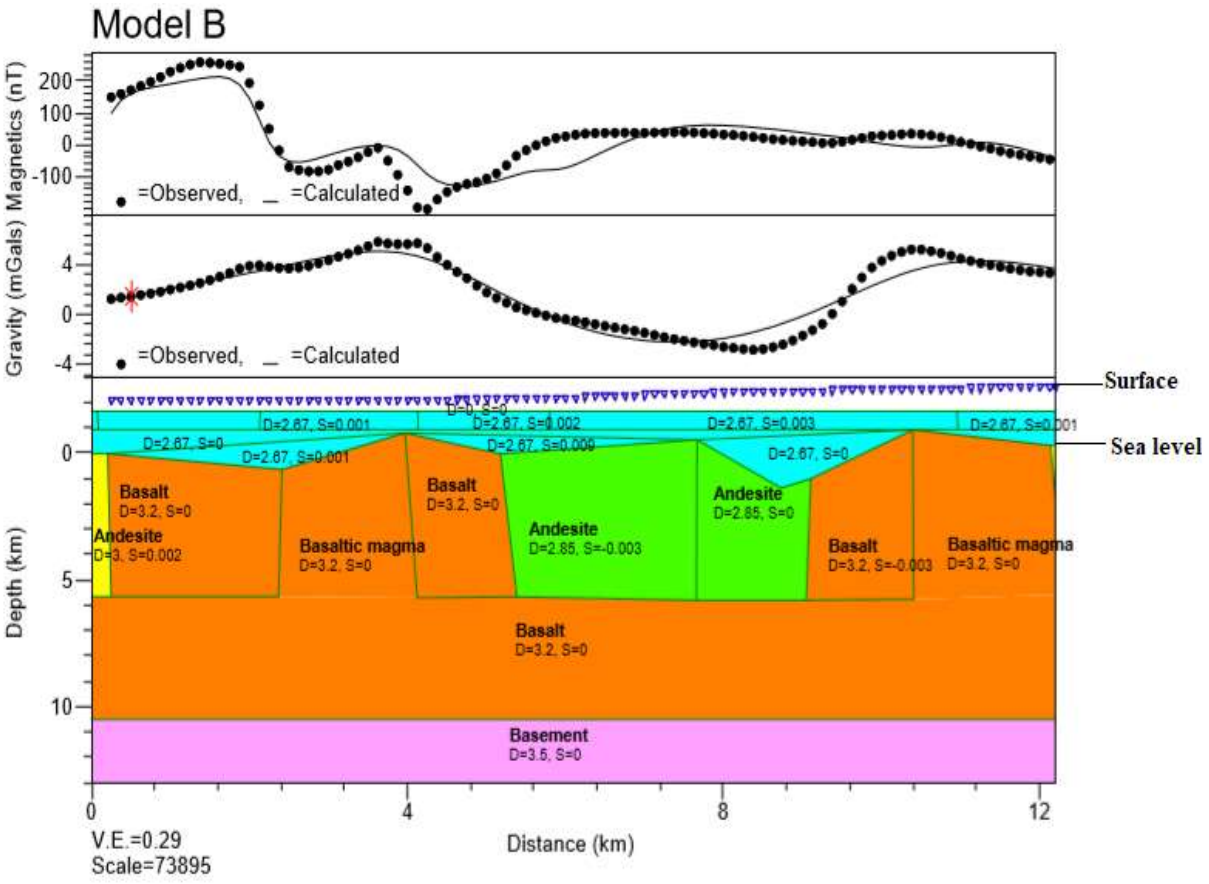

Figure 4.24: Model B constructed from profile B

Figure 4.25 shows model C constructed from profile C, as shown from gravity and magnetic anomaly maps in Figure 4.21 and Figure 4.22. The profile cuts across a high heat flux region through Opuru in the East-West direction of the study area, as displayed by the heat flux map in Figure 4.20. There is a high heat flux region in the middle of the profile with a low heat flux region to the East and West of the profile. The start model was postulated from Euler deconvolution depths. The model was constrained using the stratigraphy data of the existing wells and the geology of the study area. Model C in Figure 4.25 reveals a zone within the subsurface with few intrusions sources. The first intrusion occurs at a distance of 0 m – 951 m along the profile, having a depth of 1984 m to the top of the anomaly source. This source occurs at a relatively low heat flux region. The second intrusive occurs at a 5834 m –

7284 m along the profile with a depth range of 739 m – 1211 m to the top of the anomaly source. The peak is imaged at a distance of 6531 m along the profile with a depth of 739 m to the top of the intrusive source. The density of the intrusions ranges between 3.0 gcm^{-3} and 3.2 gcm^{-3} indicating a gravity high. This implies possibly the anomaly source emanated from the upwelling of magmatic materials from the mantle, thus resulting in a denser basaltic intrusion than crustal rocks. The magnetic susceptibility of the intrusions was modelled to be zero, indicating higher temperatures than the curie temperature at this depth. There are volcanic deposits of rhyolite, tuff, pyroclastic, and ignimbrites at 0 m – 1211 m depth. The magnetic susceptibility ranges between −0.005 cgs and 0.015 cgs, indicating low temperatures that can support the magnetism of rocks at this depth.

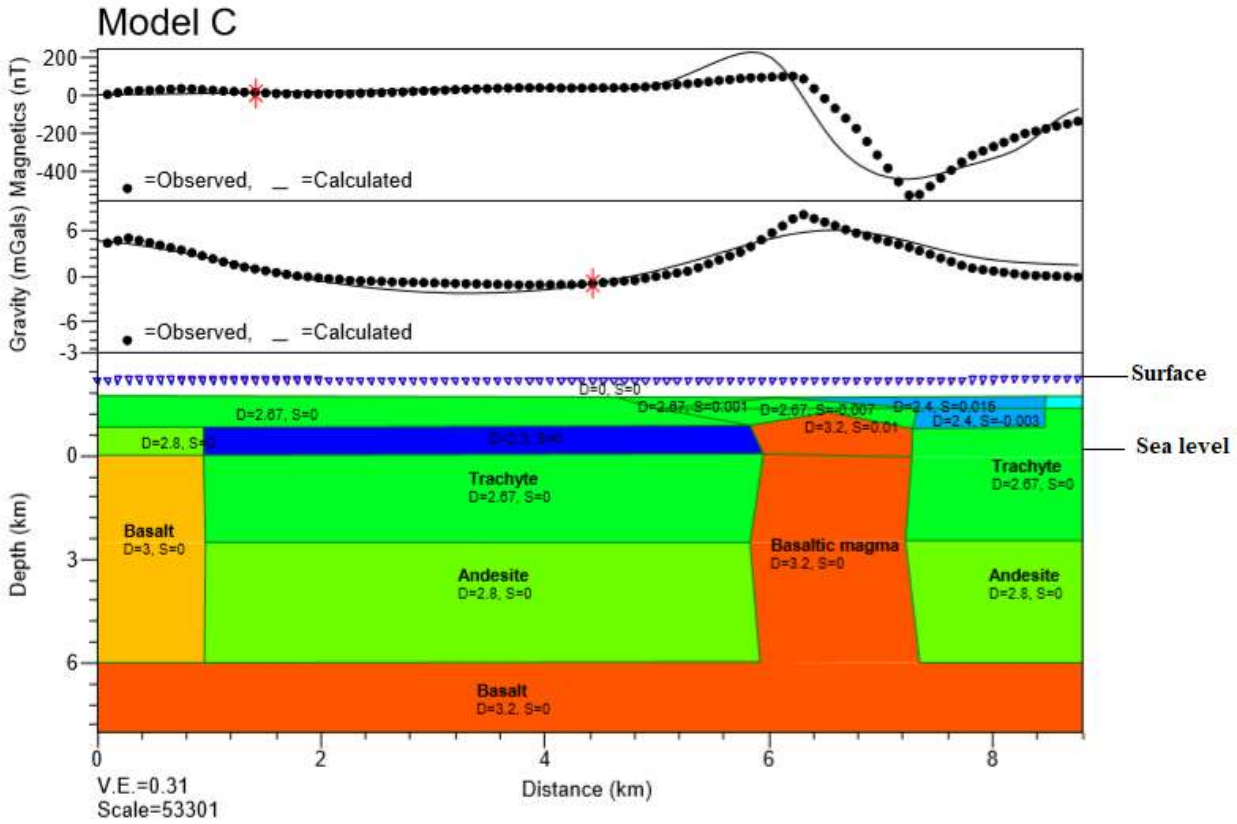

Figure 4.25: Model C constructed from profile C

Figure 4.26 shows model D constructed along profile D as shown in gravity and magnetic maps in Figure 4.21 and Figure 4.22, respectively. It is in the Northern part of the study area near Lake Elementeita. It runs from the Southwest to the Northeast of the study area and cuts along a high heat flux region, as shown in Figure 4.20. Model D was done to image the possible causes of high heat flux values and the presence of lava flows along the profile. The start model was postulated from Euler deconvolution depths. The model was constrained using stratigraphy data from existing wells and the geology of the study area. Model D reveals two mafic intrusions within volcanic rocks as shown in Figure 4.26. The first intrusion occurs at a distance of 328 m to 2324 m along the profile and the depth to the top of the anomaly source ranges between 4000 m to 5801 m. The peak of the anomaly source is imaged at 1326 m along the profile with a depth of 4000 m. This is a deep source and was interpreted to be a rhyolitic magma lying on top of basaltic magma. This could be due to the melting temperature of rocks being lowered by sipping down of water from lake Elementeita. The hot underlying basaltic magma transfers heat to the rocks causing them to melt. The melt rises, transferring heat energy to the top rocks causing their melting. This results in rhyolite magma. The second intrusion occurs at a distance range of 5067 m to 5830 m along the profile as shown in Figure 4.26. The depth to the top of the anomaly source ranges between 2486 m to 5811 m. The peak is imaged at a distance of 5314 m along the profile with a depth of 2486 m to the top of the anomaly source. This was interpreted to be a mafic intrusion in the form of basaltic magma from the mantle. The model also shows top layers with andesite, trachyte, rhyolite, ignimbrites, and tuff volcanic rocks. This implies volcanic activity in the area, hence explaining the presence of lava flows in the area. The density of the two modelled intrusions is $3.2\ \mathrm{gcm}^{-3}$ which is a gravity high. Gravity high indicates denser materials than the host rocks, probably originating from the mantle. The magnetic susceptibility of the two modelled intrusions is zero, implying a higher temperature than the curie temperature of rocks. The magnetic susceptibility of top

layers ranges between $0.001 - 0.03$ cgs units indicating lower temperatures than curie temperature.

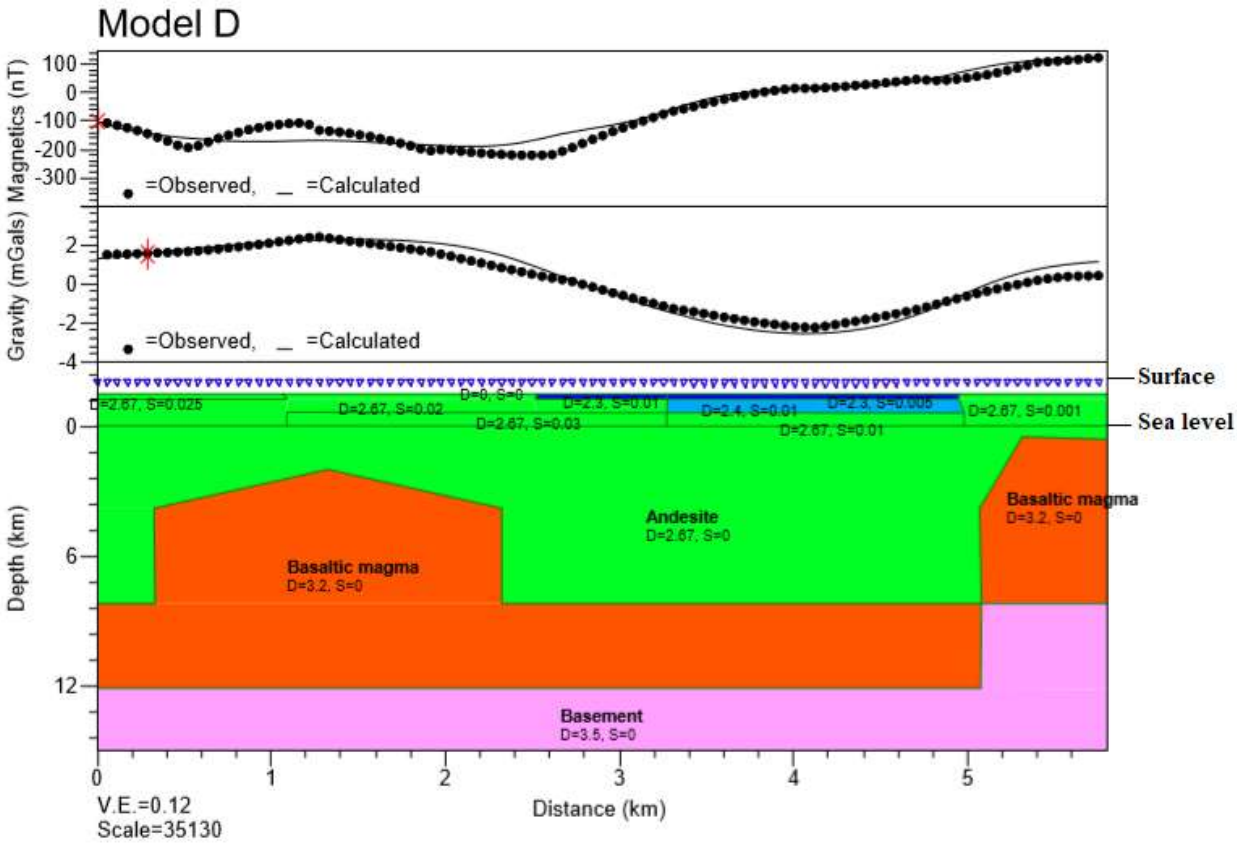

Figure 4.26: Model D constructed from profile D

4.6 Profile intersection points

The intersection points of the profiles show that the corresponding models imaged similar results. Modelling was constrained to ensure similar results at these intersection points. Profile A, B, and C cross each other at three intersection points, as shown in Figures 4.20 – 4.22. Profile A intersects profile C at Easting 197590 m and Northing 9934980 m. Their corresponding models at this point show an intruding magma at 2677 m deep with a density of 3.2 $gcm^{-3}$and magnetic susceptibility of zero. Profile A intersects profile B at Easting 192800 m and Northing 9937280 m,

as shown in Figure 4.20. Their corresponding models show an intruding magma at 4141 m deep with a density of 3.2 $gcm^{-3}$and magnetic susceptibility of zero. Profile B intersects profile C at Easting 194078 m and Northing 9934952 m. At this point, their corresponding models show an intruding magma at a depth of 3882 m deep with a density of 3.2 $gcm^{-3}$and magnetic susceptibility of zero.

4.7 Discussion

Heat flow measurements were used to map areas with elevated temperatures and high heat flux. Temperatures at 1-metre depth in this study area were found to vary between 13.8 ℃ to 94.2 ℃, with a mean temperature of 39.75 ℃. Areas with isotherm temperature greater than 40 ℃ (Mwawongo, 2017) were considered to be thermally active grounds oriented in a North-South direction and are located to the Central South of the study area. The geothermal temperature gradient varies from $0.01℃m^{-1}$ to a maximum of 46.4 $℃m^{-1}$. The mean geothermal temperature gradient was determined to be 5.03 $℃m^{-1}$. The low-temperature gradient implies temperature increases with depth at a slower rate. This could be due to either the presence of cold fluids within the subsurface or the region surrounded by cooler rocks that are hydraulically connected to cold, wet regions. For instance, cold water from Lake Elmenteita in the Northeast could be seeping down in this study area, resulting in a low-temperature gradient. Areas with low-temperature gradients are the best sites for recharging the geothermal system. The elevated temperature gradient implies temperature increases with depth at a higher rate from the surface towards the possible heat sources at deep depths. Areas with a temperature gradient greater than 0.03 $℃m^{-1}$ (Mburu, 2006) were considered to be thermally active. Heat flux was found to vary between 0.02 Wm^{-2} and 92.8 Wm^{-2}. The average heat flux was determined to be 10.06 Wm^{-2}. The region with high heat flux above the continental average of $0.06Wm^{-2}$ (Nurhandoko et al., 2013) indicates high heat loss implying that enough energy may be trapped underground to generate enough steam pressure for geothermal

energy generation. Therefore, high heat flux areas are of interest as they indicate accessible heat sources for geothermal resource development.

Gravity data show that positive and negative gravity anomalies characterize the subsurface in this study area. This means that the density of the underlying rocks in the Earth's crust in this study area varies. Euler deconvolution results of gravity data for structural indices of 0.5 and 1.0 shown in Figure 4.12 and Figure 4.13 produced five solutions on high gravity amplitudes indicating gravity anomaly sources on positive gravity anomalies. The depths of these gravity anomaly sources were estimated to vary from the shallowest at 433 m to the deepest at 2271 m. There are deeper solutions in the study area's Northern part, which becomes shallower towards the South. This was interpreted to be due to the volcanic crater at the South with a higher altitude than the North. Dense materials emanating from deeper depths were pushed to the near-surface. Some came out in the form of the lava flow, raising the altitude and possibly explaining these shallow Euler solutions. Therefore, Euler solutions at the Southern part of the study area are shallow because the dense bodies from the mantle appear to have been pushed to the near surface. These near-surface hot bodies could have contributed to altered ground, geothermal grass, hot springs, and fumaroles in the Eburru settlement scheme and Oldoinyo Opuru areas. Gravity solutions interpreted to be intruding hot dense materials from the mantle trapped towards the North occur at a depth range of $1434\ \text{m} - 2271\ \text{m}$. These intruding hot dense materials could be possible heat sources in the area. These gravity anomaly sources could be occurring beneath an impermeable sedimentary caprock in the form of a laccolith that prevents them from reaching shallow depths. Water from Lake Elementeita could be seeping down through subsurface fractures and faults to the geothermal heat sources. This water gets heated and migrates through geological structures and forms geothermal reservoirs if trapped underground or manifests on the surface in the form of fumaroles and hot springs.

Magnetic data reveals varying magnetic amplitude in this study area, as shown in Figure 4.15. Euler deconvolution results of ground magnetic data for structural indices of 0.5, 1.0, and 2.0, shown in Figure 4.16, Figure 4.17, and Figure 4.18, generated four to five solutions. These solutions are located either on a positive magnetic anomaly pole or a negative magnetic anomaly pole. The depth to magnetic anomaly sources was estimated to vary between 1090 m to 3973 m. There are deeper solutions in the Southern part of the study area, which becomes shallow to the Northwest. This shows that variation in magnetic susceptibility to the South is more pronounced at deeper depths than to the Northwest. This was interpreted to be due to the volcanic activity in the South which deposited similar magnetic materials to the near-surface. To the Northwest, there could be sedimentary deposition of varying magnetic susceptibility materials; hence Euler deconvolution results indicates shallow causative sources. Magnetic solutions occurring on a high magnetic anomaly amplitude were interpreted to be basic intruding igneous masses in the form of dykes and sills with high magnetic susceptibility materials. Magnetic solutions occurring on a low magnetic anomaly amplitude were interpreted to be hot spots that reduce magnetic susceptibility or it could be a zone of hot geothermal fluids that causes demagnetization; hence are the best sites for geothermal well drilling.

Spectral analysis of ground magnetic data in the Eburru study area indicates a curie point isotherm depth at approximately 2970 m. This implies that the magnetic susceptibility of rocks beneath the Earth's surface in the area disappears on average at this depth. The temperature at curie point isotherm depth is called the curie temperature. The curie temperature varies depending on the type of rocks present in the Earth's crust at this depth. Depending on their magnetism, rocks are classified as diamagnetic, paramagnetic, or ferromagnetic (Telford et al., 1990). Above the curie temperature, rocks cease to exhibit magnetic behaviour. Therefore, in this study area, the Curie temperature varies depending on the type of rocks present within the Earth's subsurface and their oxidation process. A curie point isotherm depth of 2970 m is a

shallow depth with a curie temperature range between 130 ℃ and 680 ℃ (Reynolds, 1998), classified as an accessible geothermal heat source. Eburru study area is a volcanic area commonly occupied by granite rhyolite rocks. This implies that the curie temperature at curie point isotherm depth could range between 463 ℃ and 580 ℃ depending on the oxidation process of the titanomagnetite mineral (Reynolds, 1998). If titanomagnetite is oxidized to titanmaghemite and finally to magnetite, then the curie temperature at this depth varies from 540 ℃ to 580 ℃. The average depth of geothermal wells ranges from 1500 m to 3000 m (World Energy Council, 2013). The isotherm depth in this study area which is approximately 2970 m is within the range and can be easily accessed by meteorite water for geothermal resource development.

Joint forward modelling of gravity and magnetic data for the profiles displayed in Figures 4.20, 4.21, and 4.22 revealed intrusions in the Earth's crust. The depth to the top of the intrusions ranges from the shallowest at 739 m to the deepest at 5811 m. Model C which cuts across a high heat flux region in the Opuru area images the shallowest intrusion at a depth of 739 m while model D which is relatively on a low heat flux region near Lake Elmenteita to the North of the study area images the deepest intrusion at a depth of 5811 m. This shows that areas with high heat flux have shallow heat sources while those with low or moderate heat flux have deep heat sources. These intrusions were interpreted to be magma heat sources. The densities of the anomaly sources were determined to range between 3.0 gcm^{-3} and 3.2 gcm^{-3} implying the intrusions are from the mantle materials or dykes extending from a batholith rock. This indicates that intrusions from the mantle have a higher density than the average density of crustal rocks. This verifies that the density of rocks in the Earth increases with depth (Telford et al., 1990). These intrusions were interpreted as basaltic magma and rhyolite, which have high heat-producing elements (Xi et al., 2015). The magnetic susceptibility of the intrusions was modelled to be 0, implying higher temperatures than the curie temperature of the crustal rocks. These indicate that intrusions from the mantle have higher temperatures than the curie temperature of crustal rocks and hence

could be geothermal heat sources. The study reveals that a high-temperature geothermal heat source is a causative body with positive gravity anomaly and zero magnetic susceptibility.

CHAPTER FIVE

CONCLUSIONS AND RECOMMENDATIONS

5.1 Conclusions

There is a high-temperature region at 1-metre depth to the South of the study area oriented in a North-South direction. This, in turn, leads to a high heat flux in the area starting at Opuru through the Eburru settlement scheme towards Oldoinyo Opuru in the South of the study area. Also, there are moderately high heat flux areas to the North of the study area near Lake Elmenteita and Eburru forest. These areas possibly indicate an accessible heat source or a good heat transfer mechanism from deep sources to the near-surface. Therefore, this study indicates that high heat flux areas near the Earth's surface could be possibly due to a shallow heat source or a good heat transfer mechanism from the deep heat sources.

There is a large positive gravity anomaly oriented in a North-South direction at the central part of the study area near Eburru forest and Opuru. Also, there is a large negative gravity anomaly oriented in the same direction in the Eburru settlement scheme towards the South of the study area. There is a general North-South trend of gravity anomalies in this study area. In the Northern parts of the study area towards Lake Elmenteita, a magnetic positive pole end and negative pole end indicate a magnetic body or structure oriented in a North-South direction. There is also a magnetic body or structure at the central part of the study area around Opuru and another one to the South near Oldoinyo Opuru. A North-South trend of magnetic anomalies implies the area has an underlying structure in this direction.

Euler deconvolution depths in the study area ranged between 433 m to 2271 m for gravity data and between 1090 m to 3973 m for magnetic data. These depths show that the high-temperature masses in the study area could be accessible for geothermal

energy generation. Spectral analysis of ground magnetic data estimated the curie point isotherm depth in this study area to be an average of 2970 m deep. This implies that the temperatures are higher than the curie temperature of rocks at this depth. This shows that this study area has an accessible heat source for geothermal energy generation. Joint forward modelling of gravity and magnetic data imaged intrusions in this study area with the depth to the top of the intrusions ranging from the shallowest at 739 m to the deepest at 5811 m. The intrusions were interpreted as basaltic magma possibly tapping heat from deep heat sources. The shallow intrusions are in the Central part of the study area in Opuru and the Southern part of Oldoinyo Opuru, explaining the high heat flux observed in the regions. The deepest intrusions are to the Northern parts of the study area near Lake Elmenteita, explaining the low heat flux values observed.

Therefore, these depths indicate that possibly the study area has an accessible heat source that can be harnessed to generate geothermal energy. The heat sources are possibly in the form of dykes tapping heat from deep hot masses and faults oriented in a North-South direction. Geothermal wells should be drilled vertically above the intrusions with high heat flux values near the Earth's surface. This is because the intrusions in the form of dykes are linked to deep heat sources. Also, the heat could be flowing upward, as evidenced by surface heat flux values. This implies that once the fluids have been heated, they rise and get trapped at a particular depth to generate the steam pressure necessary for geothermal energy production. Suppose geothermal wells are not drilled vertically above the intrusions with high heat flux values near the Earth's surface. In that case, there is a possibility of locating them in recharge areas that might not produce steam pressure. This could be why the five wells did not generate the steam pressure, yet the area has an accessible heat source from this study.

Euler deconvolution of gravity and magnetic data can locate and estimate depth to the top of potential anomaly sources within the Earth's subsurface. The depths were

confirmed by spectral analysis of ground magnetic data and joint forward modelling of gravity and magnetic data. The depths can be used to determine if the resource is economically viable or not. This is achieved by assessing if the depth is within the range that can be exploited economically. This study also shows that spectral analysis of ground magnetic data can estimate the curie point isotherm depth and its curie temperature in an area. This can further be applied to assess if the temperatures are high enough to support the development of a geothermal system at accessible depths. The temperature of the resource becomes higher than the curie temperature of crustal rocks, while its depth is the curie isotherm depth. From this study, high heat flux areas should be sited for geothermal well drilling as they indicate a shallow heat source with a reducing geothermal gradient with depth.

Spectral analysis of ground magnetic data in this study area imaged a curie point isotherm depth within the depth range determined by forward modelling of gravity and magnetic data. This was concluded that at the curie point isotherm depth, the temperature should be greater than the curie temperature of crustal rocks. The geothermal gradient reduces with depth, considering the heat flux values at the Earth's surface and the curie isotherm depth. This indicates that the heat from the source is trapped at a particular depth within the Earth's subsurface and does not flow freely to the Earth's surface. When the heat source is approached, the temperature becomes constantly high. A permeable rock could cause this between the heat source beneath and the impermeable rock on top, which lowers the heat transfer rate to the surface by conduction. Conduction is the main heat transfer method in the Earth's crust (World Energy Council, 2013). Therefore, spectral analysis of ground magnetic data can be used to estimate the depth and temperature of the resource. If the depth is an average of 3000m (World Energy Council, 2013), then a more detailed study can be carried out and eventually lead to geothermal resource development.

Joint forward modelling of gravity and magnetic data in this study area shows that the geothermal heat source has a positive gravity anomaly and 0 magnetic susceptibilities. Positive gravity anomaly verifies that the density of rocks in the Earth increases with depth, explaining the higher density of materials intruding from the mantle than the density of crustal rocks. Magnetic susceptibility of 0 indicates that these intrusions from the Earth's mantle have a higher temperature that destroys the magnetism of constituent rocks, hence could be hot geothermal heat sources. Generally, the models show intrusions with pyroclastic, ignimbrites and tuffs lying on top of trachyte, rhyolite, andesite and basalt. This shows the characteristics of a volcanic area. All intrusions imaged by the modelling are in the form of basaltic magma in a volcanic region.

5.2 Recommendations

This study recommends deeper measurement of temperature up to approximately 100 metres in depth. This will be necessary as the heat flow data obtained will have minimal effect from external heat sources such as the sun. The study also recommends other gravity and magnetic filtering techniques to generate regional and residual maps. These include butterworth filter, cosine roll-off filter, directional pass or reject filter, and the Gaussian regional or residual filter.

This study recommends coverage of a large area, approximately 100 by 100 square kilometres, for better power spectrum calculation. The study recommends trial 3-Dimensional joint modelling of gravity and magnetic data. This study also suggests overlaying the current position of the drilled geothermal wells with the heat flux and intrusions imaged in this study. Furthermore, integrating the results from geophysical, geochemical, and geological methods in this study area is recommended for geothermal well location before drilling is done.

REFERENCES

Abdelfettah, Y., Hinderer, J., Calvo, M., Dalmais, E., Maurer, V., & Genter, A. (2020). Using highly accurate land gravity and 3D geologic modeling to discriminate potential geothermal areas: Application to the Upper Rhine Graben, France. *Geophysics*, *85*(2), 35-56. doi: 10.1190/geo2019-0042.1

Aziz, F., Miller, R., Giraldo, C., & Carigali, P. (2019, September 17th). *Improving deep crustal structure depth interpretation by integrating 2D gravity-magnetic modelling and structural restoration: Offshore Borneo.* Paper presented at the SEG International Exposition and 89th Annual Meeting, San Antonio, USA.

Batir, J., Blackwell, D., & Richards, M. (2015). *Updated Heat Flow Map of Alaska: Developing a Regional Scale Map for Exploration from Limited Data.* Paper presented at the Proceedings World Geothermal Congress 2015, Melbourne, Australia.

Beard, L., & Szidarovszky, A. (2018). *Estimating depths of magnetic bodies under volcanic cover using Euler deconvolution.* Paper presented at the SEG International Exposition and 88th annual Meeting.

Beltran, V., & Manuel, J. (2003). The origin of pantellerites and the geology of the Eburru volcanic complex, Kenya Rift, Africa. ETD collection for university of Texas, El paso.

Castro, F., Oliveira, S., deSouza, J., & Ferreira, F. (2019). *Constraining Euler deconvolution solutions through combined tilt derivative filters*. Paper presented at the SEG International Exposition and 89th Annual Meeting.

Chen, H., & Zhuozhou. (2019). *Gravity, magnetic, and electromagnetic surveys' applications and challenges.* Paper presented at the International Workshop on Gravity, Electrical & Magnetic Methods and Their Applications, Xi'an, China.

Coolbaugh, M., Sladek, C., Zehner, R., & Kratt, C. (2014). Shallow temperature surveys for geothermal exploration in the great basin, USA, and estimation of shallow aquifer heat loss. *GRC Transactions, 38*.

Dawi, E. L., Tianyou, M. G., Hui, L., & Dapeny, L. (2004). Depth estimation of 2-D magnetic anomalous sources by using Euler deconvolution method. *American Journal of Applied Sciences*.

Dickerson, W. (2004). *Field geophysical training of astronauts in Taos valley*. University of Texas Austin.

Fedi, M., & Mastro, S. (2018). *Bounded-Region Wavelet spectrum: a new tool for depth estimation of gravity and magnetic data.* Paper presented at the SEG International Exposition and 88th annual Meeting, Napoli, Italy.

Felipe, F., & Valeria, C. (2017). *What to expect from Euler deconvolution estimates for isolated sources.* Paper presented at the 15th International Congress of the Brazilian Geophysical Society, Rio de Janeiro, Brazil.

Georgsson. (2009). *Geophysical methods used in geothermal exploration.* Paper presented at the Short Course IV on Exploration for Geothermal Resources, organized by UNU-GTP, KenGen and GDC, , Lake Naivasha, Kenya.

Georgsson. (2013). Geophysical methods used in geothermal exploration. *Short course VIII on exploration for geothermal resources, organized by UNU-GTP, GDC and KenGen, Lake Bogoria and Lake Naivasha, Kenya.*

Hinze, W. J. (2003). Bouguer reduction density, why 2.67? *Geophysics, 68*(5), 1559–1560. doi: 10.1190/1.1620629

Hirt, C. (2015). Gravity Forward Modelling *Encyclopedia of geodesy*.

Hochstein, M., & Kagiri, D. (1997). *The Role Of 'Steaming Ground' Over High Temperaturer Systems In The Kenya Rift.* Paper presented at the Twenty-First

Workshop on Geothermal Reservoir Engineering, Itanford University, Stanford, California.

Hong, L., Jianbao, Y., Hui, L., Pengfei, X., & Sinopec Geophysical Research Institute, C. (2017). *Gravity and aeromagnetic data interpretation of the Xiongxian geothermal system, China.* Paper presented at the SEG International Exposition and 87th Annual Meeting.

Jiao, L., & Lei, Y. (2019). *Curie point depth inversion and its potential application to geothermal resource exploration.* Paper presented at the International Workshop on Gravity, Electrical & Magnetic Methods and Their Applications, Xi'an, China.

Jica. (1980). Technical report on geothermal exploration in Eburru field Rift Valley. Republic of Kenya, JICA geothermal mission.

Kanda, I., & Fujimitsu, Y. (2018). *Geological structures controlling the placement and geometry of heat sources within Menengai geothermal field, Kenya as evidenced by gravity study.* Paper presented at the The 13th SEGJ International Symposium, Tokyo, Japan.

Kearey, P., Brooks, M., & Hill, I. (2002). *An introduction to geophysical exploration*. Iowa, USA: Iowa state university press.

Kenya Government. (2005). *Eburru Badlands Toposheet*.

Kiende, R., & Kandie, R. (2015). *Structural Geology of Eburru Volcano and Badlands Geothermal Prospects in Kenya.* Paper presented at the Fortieth Workshop on Geothermal Reservoir Engineering, Stanford University, Stanford, California.

Kiruja, J. (2011). *Direct Utilization Of Geothermal Energy.* Paper presented at the Short Course VI on Exploration for Geothermal Resources, Lake Bogoria and Lake Naivasha, Kenya.

Lowrie, W. (2007). *Fundamentals of Geophysics* (Second ed.). Newyork: Cambridge University Press.

Maithya, J., & Fujimitsu, Y. (2018). *Analysis and Interpretation of Gravity Data to delineate structural features in Eburru Geothermal Field of Kenya.* Paper presented at the The 13th SEGJ International Symposium, Tokyo, Japan.

Maithya, J., & Fujimitsu, Y. (2019). *Three-dimensional Magnetotelluric Inversion to map geothermal structures in Eburru Geothermal field, Kenya.* Paper presented at the Japan Geoscience Union Meeting, Makuhari Messe, Chiba, Japan.

Manzella, A. (2017). *Geothermal Energy*. Paper presented at the EPJ Web of conferences.

Mariita, N. (1995). Exploration for Geothermal Energy in Kenya – A Historical Perspective. *Geothermal research report*. Japan: Kyushu University.

Mariita, N. (2011). *Application of geophysical methods to geothermal energy exploration in Kenya.* Paper presented at the Short Course VI on Exploration for Geothermal Resources, UNU-GTP, GDC and KenGen, Lake Bogoria and Lake Naivasha, Kenya.

Mburu, M. (2006). *Geothermal mapping using temperature measurements*. Paper presented at the Fourth African Rift Geothermal Conference, Addis Ababa, Ethiopia.

Melo, F., & Barbosa, V. (2018). Correct structural index in Euler deconvolution via base-level estimates. *Geophysics, 83*(6), J87-J98. doi: 10.1190/GEO2017-0774.1

Moghaddam, M., Oskooi, B., Mirzaei, M., & Jouneghani, J. (2012). *Magnetic studies for geothermal exploration in Mahallat, Iran*. Paper presented at the International geophysical conference and oil & gas exploration., Istanbul, Turkey.

Mohamed, H., & Saibi, H. (2017). *3-D Forward Modelling of Magnetic Data from Al-Mubazzarah Geothermal Field, Al-Ain, UAE.* Paper presented at the ICEG, Al-Ain, Abu Dhabi, UAE.

Monasterial, C. J. (2015). Microgravity survey in 2009-2010 around Bacman geothermal field, Philippines - gravity corrections and interpretations. UNU-GTP

Orkustofnun, Grensasvegur 9, Reports 2015 IS-108 Reykjavik, Iceland Number 23.

Mulaha, T. (2013). *An Overview of Geothermal Resources Development in Kenya. Roundtable on the Global Geothermal Development Plan*. The Hague, Netherlands.

Mwangi, A. (2012). *MT and TEM Joint Inversion of Eburru high Temperature Geothermal Field, Kenya.* Paper presented at the 4th African Rift Geothermal Conference, Nairobi, Kenya.

Mwangi, A. (2018). *Magnetotelluric Analysis Of Central Kenya Kenyan Rift Volcanoes For Geothermal Development.* University of Texas at El Paso, Digital commons @UTEP.

Mwarania, F. (2014). Reservoir evaluation and modelling of the Eburru geothermal system, Kenya. United Nations University Geothermal Training Programme: University of Iceland

Mwawasi, H. M. (2012). Heat Loss Assessment of Selected Kenyan Geothermal Prospects. *GRC Transactions, 36*, 717-722.

Mwawongo, G. (2005). Kenya's geothermal prospects outside olkaria: Status of exploration and development. (Vol. 4, pp. 41-50): United Nations University, Geothermal Training Programme.

Mwawongo, G. (2013). *Geothermal mapping using temperature measurements.* Paper presented at the Short course VIII on exploration for geothermal resources, organized by UNU-GTP, GDC and KenGen, Oct. 31 – Nov. 22., Lake Bogoria and Lake Naivasha, Kenya.

Mwawongo, G. (2017). *Geothermal mapping using temperature measurements.* Paper presented at the SDG Short Course II on Exploration and Development of

Geothermal Resources, organized by UNU-GTP, GDC and KenGen, November. 9th -29th., Lake Bogoria and Lake Naivasha, Kenya.

Ndombi, J. M. (1981). The structure of the shallow crust beneath the Olkaria geothermal field, Kenya, deduced from gravity studies. *J. Volcanol. Geotherm. Res, 9*(237-251).

Nurhandoko, B., Kurniadi, R., Budi, M., Ardi, S., Rizal, I., & Kusharyo, D. (2013). *Geothermal Heat Flow Measurement and its Inversion Modeling for Source Rock Characterization*. Paper presented at the HAGI-IAGI Joint Convention, Medan.

Nyakundi, E. R., Githiri, J., & Ambuso, W. (2017). Geophysical investigation of geothermal potential of the Gilgil area, Nakuru county, Kenya using gravity. *journal of geology and geophysics, 6*(2). doi: 10.4172/2381-8719.1000278

Ochieng, L. (2013). *Overview of geothermal surface exploration methods.* Paper presented at the Short Course VIII on Exploration for Geothermal Resources, organized by UNU-GTP, GDC and KenGen, Lake Bogoria and Lake Naivasha, Kenya.

Okubo, Y., Graf, J., R, Hansen, R., O, Ogawa, K., & Tsu, H. (1985). Curie point depths of island of Kyushu and surrounding areas Japan. *Geophysics, 53*.

Omenda, P., Opondo, K., Lagat, J., Mungania, J., Mariita, N., Onacha, S., . . . Ouma, P. (2000). Ranking of geothermal prospects in the Kenya Rift. (pp. 121): Kenya Electricity Generating Company Limited, internal report.

Parasnis, D. S. (1952). A Study of Rock Densities in the English Midlands. *Geophysical Supplements to the Monthly Notices of the Royal Astronomical Society*. (Vol. 6, pp. 252-271).

Parasnis, D. S. (1986). *Principles of applied geophysics*. Newyork, USA: Chapman and Hall Ltd.

Pawan, D., Ramprasad, T., Ramana, M. V., Desa, M., & Shailaja, B. (2007). Automatic interpretation of magnetic data using Euler deconvolution with nonlinear background. *Pure and Applied Geophysics, 164*, 2359-2372.

Pipan, M. (2009). *Remote sensing and geophysical methods for geothermal exploration. Presented at the School on Geothermics, organized by ICTP, ICS-UNIDO and IAEA, Trieste, Italy.*

Reid, A. B., Allsop, J. M., Granser, H., Millett, A. J., & Somerton, W. I. (1990). Magnetic interpretation in three dimensions using Euler deconvolution. *Geophysics, 55*, 80-91.

Reid, A. B., & Thurston, J. B. (2014). The structural index in gravity and magnetic interpretation: Errors, uses, and abuses. *Geophysics, 79*, J61-J66.

Reynolds, J. M. (1998). *An introduction to applied and environmental geophysics*. Chichester, England: John Wiley & sons Ltd.

Rivas, J. A. (2013). *Seismic activity, gravity and magnetic measurements.* Paper presented at the Short Course V on Conceptual Modelling of Geothermal Systems, organized by UNU-GTP and LaGeo, Santa Tecla, El Salvador.

Ronoh, I. (2015). Evolution and Geology of Eburru-Badlands Geothermal Prospect Central Kenyan Rift. *GRC Transactions, 39*.

Santos, P. A., & Rivas, A. J. (2009). *Gravity Survey Contribution to Geothermal Exploration in El Salvador. The cases of Berlin, Ahuachapán and San Vicente areas.* Paper presented at the Short course on surface exploration for geothermal resources organized by UNU-GTP and LaGeo, Ahuachapan and Santa Tecla, El Salvador.

Schermerhorn, W., Ritzinger, B., Anderson, M., Witter, J., Glen, J., Forson, C., . . . Fournier, D. (2017). *Geothermal exploration of Mount Baker hot springs through ground-based magnetic and gravity surveys.* Paper presented at the 42nd

workshop on geothermal reservoir engineering, Stanford university, Stanford, California.

Scintrex. (2012). CG-5 Scintrex Autograv TM System Operation Manual. SCINTREX Limited. Ontario Canada.

Shah, M., Sircar, A., Dwijen, V., Sahajpal, S., Chaudhary, A., & Dhale, S. (2015). Overview of geothermal surface exploration methods. *ResearchGate publications 1*(4).

Simiyu, S. M., & Keller, G. R. (1997). Integrated geophysical analysis of the East African Plateau from gravity anomalies and recent seismic studies. *Journal of Tectonophysics, 278*, 291-314.

Sippel, J., Meeßen, C., Cacace, M., Mechie, J., Fishwick, S., Heine, C., . . . Strecker, M. (2017). The Kenya Rift revisited: insights into lithospheric strength through data-driven 3-D gravity and thermal modelling. *Solid Earth, 8*(45), 45-81. doi: 10.5194/se-8-45-2017

Spector, A., & Grant, F. S. (1970). Statistical models for interpreting aeromagnetic data. *Geophysics, 35*(2), 293-302.

Telford, W. M., Geldart, L. P., & Sheriff, R. E. (1990). *Applied Geophysics*. Cambridge: Cambridge University Press.

Thompson. (1982). EULDPH: A new technique for making computer-assisted depth estimates from magnetic data. *Geophysics, 47*(31).

Thompson, & Dodson, R. (1963). Geology of the Naivasha area. Report No.55: Geological Survey of Kenya.

Woodhall, D. G., & Clarke, M. C. G. (1988). *Geological map of Longonot volcano, The greater Olkaria and Eburru volcanic complexes and adjacent areas*. England: Cook Hammond & Kell Ltd.

World Energy Council. (2013). World Energy Resources (pp. 354-415). London.

Xi, Y., Wang, Y., Hu, X., Liu, S., Zhao, Y., & Liu, T. (2015). *Geothermal structure revealed by Curie isotherm surface in Guangdong province.* Paper presented at the International Workshop on Gravity, Electrical & Magnetic Methods and Their Applications, Chengdu, China.

Yehuwalashet, E., & Malehmir, A. (2018). *Gravity and magnetic survey, modeling and interpretation in the Blötberget iron-oxide mining area of central Sweden.* Paper presented at the SEG International Exposition and 88th annual Meeting.

Zhi, J., Li, H., Du, J., Liang, Q., Liu, Y., & Chen, C. (2018). *Curie point depth estimates based on spectrum analysis from aeromagnetic data in Guangxi Province, China.* Paper presented at the SEG International Exposition and 88th annual Meeting.

APPENDICES

Appendix I: Heat flow data

Station	At 50cm (℃)	At 100cm (℃)	M ($℃m^{-1}$)	q (Wm^{-2})
1	48.2	58.2	20	40
2	58.7	60.5	3.6	7.2
3	92.2	92.4	0.4	0.8
4	92.4	92.6	0.4	0.8
5	14	16.6	5.2	10.4
6	16.3	16.7	0.8	1.6
7	13.5	13.8	0.6	1.2
8	91	91.3	0.6	1.2
9	21	23.6	5.2	10.4
10	91.5	94.2	5.4	10.8
11	19.7	20	0.6	1.2
12	87.6	89.6	4	8
13	86.2	91.4	10.4	20.8
14	36.6	56.4	39.6	79.2
15	91	91.8	1.6	3.2
16	90.8	91.4	1.2	2.4
17	87.5	90.6	6.2	12.4
18	70.5	87.5	34	68
19	73	86.5	27	54
20	81.5	89.5	16	32
21	73.2	74.8	3.2	6.4
22	83.4	91	15.2	30.4
23	27.3	30.9	7.2	14.4
24	34.4	42.5	16.2	32.4
25	22.5	27.2	9.4	18.8
26	26.1	31.2	10.2	20.4
27	54.8	56.6	3.6	7.2
28	41.8	41.8	0	0
29	85	85	0	0
30	53.1	53.3	0.4	0.8
31	66.7	76	18.6	37.2
32	86	86	0	0
33	55.1	78.3	46.4	92.8

34	75	88.6	27.2	54.4
35	90.8	91.1	0.6	1.2
36	20.5	21	1	2
37	19.5	19.7	0.4	0.8
38	22.1	27	9.8	19.6
39	19.4	19.9	1	2
40	21	21.4	0.8	1.6
41	36	46	20	40
42	54	60	12	24
43	57	57.3	0.6	1.2
44	77	82.6	11.2	22.4
45	46.2	51.2	10	20
46	57.2	78.2	42	84
47	37.6	46.1	17	34
48	57.5	62.6	10.2	20.4
49	31.1	41.8	21.4	42.8
50	54.6	69.5	29.8	59.6
51	19.4	20.4	2	4
52	19.1	19.6	1	2
53	21	24.9	7.8	15.6
54	21.3	35.4	28.2	56.4
55	24.6	24.6	0	0
56	21.2	21.2	0	0
57	20.8	20.9	0.2	0.4
58	21.5	23.1	3.2	6.4
59	23.1	24.1	2	4
60	23.9	24.1	0.4	0.8
61	27.1	27.2	0.2	0.4
62	25.4	26.1	1.4	2.8
63	20.9	21	0.2	0.4
64	24.1	26.4	4.6	9.2
65	24.6	24.6	0	0
66	26.7	27	0.6	1.2
67	27.3	27.3	0	0
68	28.4	28.4	0	0
69	27.6	27.6	0	0
70	23.3	23.3	0	0
71	25.6	27	2.8	5.6
72	26.1	31.5	10.8	21.6

73	25.5	27.6	4.2	8.4
74	24	24	0	0
75	19	19.2	0.4	0.8
76	24.2	24.2	0	0
77	23.5	23.7	0.4	0.8
78	23.2	23.3	0.2	0.4
79	23	25	4	8
80	23.2	23.9	1.4	2.8
81	24	24	0	0
82	24.8	24.9	0.2	0.4
83	25.3	25.6	0.6	1.2
84	30.5	31	1	2
85	28.3	28.5	0.4	0.8
86	28	28	0	0
87	26.8	28	2.4	4.8
88	28.1	28.6	1	2
89	31.6	32.2	1.2	2.4
90	29.3	29.6	0.6	1.2
91	29.8	33.6	7.6	15.2
92	30.5	30.8	0.6	1.2
93	30.2	30.6	0.8	1.6
94	27.9	28.2	0.6	1.2
95	24.4	25	1.2	2.4
96	23.6	23.9	0.6	1.2
97	25.5	27.7	4.4	8.8
98	23.4	23.6	0.4	0.8
99	26.2	27.1	1.8	3.6
100	29.6	29.9	0.6	1.2
101	29.9	30.2	0.6	1.2
102	32.7	34.4	3.4	6.8
103	34.3	34.9	1.2	2.4
104	32.8	33	0.4	0.8
105	33	34.4	2.8	5.6
106	33.6	34.1	1	2
107	24.8	25	0.4	0.8
108	23.8	24.6	1.6	3.2
109	26	26.6	1.2	2.4
110	28.9	29.1	0.4	0.8
111	28.7	29.9	2.4	4.8

112	30.2	33.3	6.2	12.4
113	30.3	30.5	0.4	0.8
114	34	34.2	0.4	0.8
115	35.2	36.6	2.8	5.6
116	33.7	34.1	0.8	1.6
117	24.4	25.2	1.6	3.2
118	25.1	27	3.8	7.6
119	57	57.1	0.2	0.4
120	29	29.8	1.6	3.2
121	33.4	35.5	4.2	8.4
122	34.6	34.8	0.4	0.8
123	31.7	32.4	1.4	2.8
124	85.6	85.9	0.6	1.2
125	85.2	86.6	2.8	5.6
126	91.4	91.9	1	2
127	64.4	65.1	1.4	2.8
128	89.6	90.3	1.4	2.8
129	91.3	92.1	1.6	3.2
130	76.2	77.1	1.8	3.6
131	73.8	74	0.4	0.8
132	41	51	20	40
133	30.6	32.3	3.4	6.8
134	82.9	83.2	0.6	1.2
135	63.5	78.1	29.2	58.4
136	66.3	71	9.4	18.8
137	64.1	82.1	36	72
138	50	56	12	24
139	20.6	20.8	0.4	0.8
140	26.2	27.7	3	6
141	28.2	30.7	5	10
142	26.5	26.9	0.8	1.6
143	69.8	80.8	22	44
144	27.9	34.9	14	28
145	27.7	32.8	10.2	20.4
146	26.9	27.4	1	2
147	26.7	30.4	7.4	14.8
148	25.1	27	3.8	7.6
149	25.2	26.1	1.8	3.6
150	25.8	26	0.4	0.8

151	25.8	27	2.4	4.8
152	24.7	26.7	4	8
153	29.2	29.6	0.8	1.6
154	28.9	31.1	4.4	8.8
155	27	29	4	8
156	27.5	29	3	6
157	27	28.6	3.2	6.4
158	26	27.5	3	6
159	27.1	27.7	1.2	2.4
160	27.1	28	1.8	3.6
161	26.5	27.1	1.2	2.4
162	28.6	28.9	0.6	1.2
163	26.8	30.6	7.6	15.2
164	26.3	28	3.4	6.8
165	29.2	29.3	0.2	0.4
166	24	25.7	3.4	6.8
167	26.8	26.9	0.2	0.4
168	26.7	26.7	0	0
169	25.7	25.9	0.4	0.8
170	25	27.1	4.2	8.4
171	24.7	29.9	10.4	20.8
172	26	29	6	12
173	27	29	4	8
174	27.6	29.1	3	6
175	28	31	6	12
176	25.5	27.2	3.4	6.8
177	27.5	27.9	0.8	1.6
178	28.6	28.8	0.4	0.8
179	27.8	32.4	9.2	18.4
180	25.2	31.6	12.8	25.6
181	28	28.7	1.4	2.8
182	25.5	26	1	2
183	26.8	27.2	0.8	1.6
184	28.4	28.7	0.6	1.2
185	26.2	27.5	2.6	5.2
186	28	28.9	1.8	3.6
187	29.8	30.4	1.2	2.4
188	26.5	26.8	0.6	1.2
189	29.4	33	7.2	14.4

190	30.7	31.3	1.2	2.4
191	51.1	60.9	19.6	39.2
192	28.7	29.2	1	2
193	25.8	27.2	2.8	5.6
194	24.8	25.7	1.8	3.6
195	69.2	73.6	8.8	17.6
196	64.9	74.2	18.6	37.2
197	26.9	28.8	3.8	7.6
198	62.7	74.5	23.6	47.2
199	50	52.6	5.2	10.4
200	83.1	85.7	5.2	10.4
201	22.4	23.6	2.4	4.8
202	21.3	23.8	5	10
203	27	30.9	7.8	15.6
204	26.6	27.4	1.6	3.2
205	24.2	24.4	0.4	0.8
206	27.6	30.3	5.4	10.8
207	27.3	28.1	1.6	3.2
208	30.8	31.2	0.8	1.6
209	30	31.5	3	6
210	28	29.7	3.4	6.8
211	28.6	28.9	0.6	1.2
212	27.6	27.7	0.2	0.4
213	27.2	29.8	5.2	10.4
214	32	32.5	1	2
215	32.5	33.8	2.6	5.2
216	27.1	27.8	1.4	2.8
217	28	28.1	0.2	0.4
218	28.6	29.2	1.2	2.4
219	30.7	32.3	3.2	6.4
220	28.8	29.7	1.8	3.6
221	27.6	28.2	1.2	2.4
222	26.6	26.8	0.4	0.8
223	28.6	30.1	3	6
224	27.5	30.8	6.6	13.2
225	24.1	24.6	1	2
226	25.6	25.8	0.4	0.8
227	30.6	36	10.8	21.6
228	26.1	26.4	0.6	1.2

Appendix II: Gravity data

Stations	Drift (mGal)	GA (mGal)	Latitude (°)	LC (mGal)	FAC (mGal)	BC (mGal)	TC (mGal)	CBA (mGal)
1	-0.0234	977295.27	-0.6211	978033.28	714.5099	259.0844	0.56044	-282.0314
2	-0.0265	977296.47	-0.6230	978033.29	712.8774	258.4924	0.85329	-281.5826
3	-0.0322	977297.08	-0.6266	978033.29	711.5063	257.9953	1.16131	-281.5471
4	-0.0340	977297.35	-0.6280	978033.30	708.2947	256.8307	2.15936	-282.3255
5	-0.0379	977299.99	-0.6281	978033.30	708.8474	257.0311	1.95561	-279.5376
6	-0.0413	977299.68	-0.6263	978033.29	712.2753	258.2741	0.98105	-278.6288
7	-0.0454	977296.92	-0.6246	978033.29	713.5813	258.7477	0.71783	-280.8230
8	-0.0481	977296.22	-0.6227	978033.29	714.9765	259.2536	0.48995	-280.8562
9	-0.0521	977295.11	-0.6210	978033.28	714.9160	259.2317	0.49877	-281.9902
10	-0.0547	977294.58	-0.6211	978033.28	716.4050	259.7716	0.30711	-281.7625
11	-0.0596	977293.10	-0.6229	978033.29	716.8945	259.9490	0.25521	-282.9904
12	-0.0622	977293.58	-0.6246	978033.29	715.2172	259.3409	0.45572	-283.3776
13	-0.0655	977294.81	-0.6249	978033.29	720.0598	261.0968	0.03873	-279.4789
14	0.0114	977294.03	-0.6204	978033.28	713.7977	258.8261	0.67906	-283.6016
15	0.0233	977301.75	-0.6160	978033.27	701.1873	254.2536	6.59934	-277.9927
16	0.0213	977298.37	-0.6121	978033.27	702.8908	254.8713	5.14493	-281.7269
17	0.0337	977318.48	-0.6077	978033.26	677.0628	245.5059	1.12923	-282.0907
18	0.0521	977322.52	-0.6035	978033.25	672.7585	243.9452	0.36119	-281.5520
19	0.0719	977328.81	-0.5990	978033.24	663.8708	240.7224	0.06674	-281.2135
20	0.0793	977332.16	-0.5947	978033.23	657.5550	238.4323	0.80829	-281.1421
21	0.0942	977337.85	-0.5905	978033.23	647.3184	234.7205	5.16359	-277.6165
22	-0.0032	977317.39	-0.6169	978033.28	678.7108	246.1035	1.57920	-281.6943
23	-0.0051	977320.84	-0.6126	978033.27	673.4430	244.1933	0.45020	-282.7282
24	-0.0060	977321.09	-0.6082	978033.26	676.2898	245.2256	0.95144	-280.1522

25	-0.0081	977320.17	-0.6032	978033.25	676.9987	245.4827	1.11370	-280.4524
26	-0.0090	977327.12	-0.5991	978033.24	665.8965	241.4569	0.00418	-281.6785
27	-0.0112	977337.70	-0.5952	978033.23	650.3770	235.8295	3.22014	-277.7716
28	-0.0126	977340.63	-0.5909	978033.23	645.2406	233.9671	6.98814	-274.3327
29	-0.0145	977343.14	-0.5866	978033.22	640.6138	232.2893	13.57652	-268.1746
30	-0.0156	977346.94	-0.5822	978033.21	633.4675	229.6981	8.17699	-274.3243
31	-0.0174	977349.67	-0.5778	978033.20	628.3679	227.8489	3.85832	-279.1539
32	-0.0184	977355.79	-0.5729	978033.19	618.5529	224.2900	0.54654	-282.5921
33	-0.0245	977367.54	-0.5692	978033.19	602.6890	218.5377	0.68129	-280.8121
34	0.0050	977297.48	-0.6225	978033.29	712.5330	258.3676	0.92498	-280.7173
35	0.0093	977314.88	-0.6182	978033.28	684.1144	248.0628	3.97911	-278.3666
36	0.0111	977316.64	-0.6137	978033.27	681.1465	246.9867	2.45687	-280.0085
37	0.0142	977313.78	-0.6096	978033.26	685.5327	248.5771	4.93720	-277.5878
38	0.0158	977317.79	-0.6059	978033.25	679.4696	246.3786	1.82292	-280.5482
39	0.0196	977325.76	-0.6018	978033.25	669.4228	242.7356	0.07398	-280.7255
40	0.0199	977335.85	-0.5977	978033.24	655.5275	237.6971	1.27121	-278.2870
41	0.0226	977340.10	-0.5933	978033.23	647.4005	234.7502	5.10097	-275.3773
42	0.0244	977342.83	-0.5890	978033.22	642.6536	233.0290	10.08374	-270.6804
43	0.0275	977351.37	-0.5848	978033.21	630.0705	228.4663	5.00087	-275.2362
44	0.0292	977353.58	-0.5806	978033.21	625.1968	226.6991	2.29203	-278.8373
45	0.0325	977362.28	-0.5761	978033.20	610.9107	221.5189	0.00012	-281.5263
46	0.0338	977368.10	-0.5717	978033.19	604.1866	219.0807	0.44667	-279.5341
47	0.0057	977311.59	-0.6180	978033.28	688.2974	249.5796	7.38428	-275.5898
48	0.0069	977316.11	-0.6135	978033.27	679.1076	246.2474	1.70356	-282.5987
49	0.0078	977324.50	-0.6093	978033.26	669.2334	242.6669	0.06438	-282.1267
50	0.0093	977322.78	-0.6048	978033.25	675.4461	244.9197	0.77903	-279.1632
51	0.0102	977323.03	-0.6006	978033.24	674.8764	244.7131	0.67450	-279.3773
52	0.0116	977324.60	-0.5961	978033.24	670.4480	243.1074	0.13794	-281.1604
53	0.0127	977336.23	-0.5917	978033.23	651.7780	236.3375	2.55406	-278.9998

54	0.0155	977350.05	-0.5869	978033.22	630.5025	228.6229	5.33228	-275.9538
55	0.0166	977350.94	-0.5824	978033.21	625.5945	226.8433	2.45518	-281.0643
56	0.0181	977350.08	-0.5780	978033.20	626.7595	227.2657	2.98438	-280.6418
57	0.0190	977353.82	-0.5736	978033.19	621.5590	225.3800	1.13998	-282.0558
58	0.0205	977356.43	-0.5690	978033.19	619.4627	224.6198	0.69830	-281.2114
59	0.0216	977357.91	-0.5643	978033.18	617.0901	223.7596	0.34667	-281.5888
60	0.0232	977360.57	-0.5643	978033.18	617.0901	223.7596	0.34667	-278.9272
61	-0.0093	977296.95	-0.6207	978033.28	713.0367	258.5502	0.82137	-281.0208
62	-0.0129	977303.90	-0.6167	978033.28	701.6339	254.4155	6.18697	-275.9682
63	-0.0141	977310.73	-0.6121	978033.27	693.3072	251.3962	15.39828	-265.2289
64	-0.0174	977314.96	-0.6079	978033.26	686.0826	248.7765	5.35764	-275.6324
65	-0.0188	977320.08	-0.6033	978033.25	677.6714	245.7266	1.28358	-279.9407
66	-0.0225	977325.40	-0.5988	978033.24	668.9195	242.5531	0.04998	-281.4296
67	0.0232	977253.09	-0.6146	978033.27	766.9799	278.1103	1.17981	-290.1331
68	0.0269	977272.00	-0.6101	978033.26	742.8696	269.3678	6.42004	-281.3360
69	0.0283	977287.53	-0.6056	978033.25	722.4770	261.9733	0.00113	-285.2173
70	0.0318	977301.17	-0.6019	978033.25	702.9152	254.8801	5.12632	-278.9139
71	0.0223	977316.81	-0.5984	978033.24	681.2697	247.0313	2.50913	-279.6867
72	0.0366	977327.66	-0.5965	978033.24	665.0592	241.1534	0.02086	-281.6543
73	0.0384	977335.06	-0.5952	978033.23	653.4537	236.9452	1.90134	-279.7641
74	0.0421	977331.70	-0.5981	978033.24	656.5857	238.0808	1.01277	-282.0252
75	0.0435	977328.26	-0.6005	978033.24	660.2781	239.4197	0.37542	-283.7477
76	0.0477	977335.51	-0.5936	978033.23	651.4321	236.2121	2.70751	-279.7913
77	0.0496	977340.67	-0.5896	978033.22	645.3073	233.9912	6.92173	-274.3174
78	0.0534	977347.12	-0.5851	978033.22	635.5478	230.4524	10.97828	-270.0187
79	0.0443	977354.78	-0.5806	978033.21	623.1227	225.9470	1.56700	-279.6861
80	0.0616	977367.59	-0.5732	978033.19	599.4675	217.3695	1.41067	-282.0920
81	0.7018	977238.02	-0.6288	978033.30	793.8636	287.8584	3.21629	-286.0545
82	1.1256	977240.61	-0.6256	978033.29	787.1547	285.4257	0.90204	-290.0549

83	1.2315	977240.97	-0.6221	978033.29	785.1438	284.6966	0.53836	-291.3348
84	1.5626	977246.41	-0.6175	978033.28	774.9841	281.0126	0.06589	-292.8320
85	1.7744	977267.77	-0.6183	978033.28	749.4391	271.7499	17.19628	-270.6181
86	2.1585	977276.99	-0.6141	978033.27	735.2373	266.6003	1.89822	-285.7423
87	2.4498	977290.05	-0.6122	978033.27	717.8354	260.2902	0.16988	-285.4993
88	2.7279	977295.06	-0.6101	978033.26	709.9895	257.4453	1.57911	-284.0777
89	0.0089	977369.30	-0.5710	978033.19	604.6165	219.2366	0.38973	-278.1249
90	0.0113	977369.43	-0.5716	978033.19	603.6849	218.8988	0.51883	-278.4546
91	0.0131	977370.13	-0.5746	978033.20	603.4164	218.8014	0.56006	-277.8931
92	0.0144	977370.34	-0.5762	978033.20	603.5053	218.8336	0.54620	-277.6435
93	0.0193	977372.21	-0.5790	978033.20	601.3275	218.0440	0.94856	-276.7628
94	0.0213	977372.47	-0.5786	978033.20	601.0331	217.9372	1.01382	-276.6279
95	0.0226	977373.52	-0.5752	978033.20	599.5888	217.4135	1.37674	-276.1271
96	0.0244	977367.75	-0.5765	978033.20	598.6831	217.0851	1.64423	-282.2116
97	0.0259	977371.43	-0.5747	978033.20	598.6464	217.0718	1.65578	-278.5322
98	0.0278	977371.99	-0.5727	978033.19	598.3655	216.9699	1.74604	-278.0567
99	0.0290	977369.83	-0.5712	978033.19	597.7684	216.7534	1.94959	-280.3954
100	0.0329	977371.99	-0.5697	978033.19	595.3610	215.8805	2.95295	-278.7622
101	0.0339	977374.66	-0.5670	978033.18	593.1344	215.0731	4.20309	-276.2601
102	0.0355	977376.44	-0.5639	978033.18	590.5132	214.1226	6.20916	-274.1371
103	0.0376	977375.77	-0.5602	978033.17	588.5681	213.4173	8.20060	-274.0526
104	0.0376	977376.12	-0.5589	978033.17	587.3698	212.9828	9.71369	-272.9471
105	0.0409	977376.86	-0.5574	978033.17	587.1269	212.8948	10.05336	-272.0183
106	0.0430	977375.57	-0.5562	978033.16	590.4274	214.0915	6.28681	-274.9691
107	0.0445	977376.28	-0.5531	978033.16	590.0697	213.9618	6.61990	-274.1462
108	0.0468	977377.90	-0.5537	978033.16	588.9076	213.5404	7.81539	-272.0798
109	0.0480	977379.44	-0.5528	978033.16	588.8394	213.5157	7.89138	-270.5014
110	0.0523	977380.27	-0.5508	978033.15	591.2807	214.4009	5.55111	-270.4549
111	0.0567	977372.06	-0.5642	978033.18	600.8800	217.8817	1.04886	-277.0670

112	0.0596	977370.69	-0.5594	978033.17	601.0124	217.9297	1.01851	-278.3803
113	0.0623	977369.82	-0.5544	978033.16	601.2111	218.0018	0.97402	-279.1600
114	0.0649	977364.83	-0.5513	978033.16	604.5709	219.2200	0.39557	-282.5813
115	0.0678	977366.77	-0.5497	978033.15	601.4525	218.0893	0.92169	-282.0990
116	0.0705	977367.59	-0.5482	978033.15	600.3467	217.6883	1.17711	-281.7195
117	0.0731	977367.06	-0.5441	978033.14	602.8637	218.6010	0.65087	-281.1660
118	0.0755	977364.27	-0.5386	978033.13	604.4561	219.1784	0.41047	-283.1799
119	0.0784	977367.23	-0.5345	978033.13	600.7084	217.8195	1.08907	-281.9216
120	0.0813	977366.25	-0.5353	978033.13	599.4888	217.3773	1.40467	-283.3649
121	0.0840	977367.54	-0.5390	978033.13	601.3821	218.0638	0.93676	-281.3437
122	0.0861	977367.33	-0.5374	978033.13	604.2953	219.1201	0.43186	-280.1907
123	0.0885	977365.78	-0.5417	978033.14	605.0483	219.3931	0.33693	-281.3683
124	0.0906	977365.31	-0.5456	978033.15	604.9051	219.3412	0.35396	-281.9173
125	0.0954	977367.93	-0.5408	978033.14	601.9579	218.2726	0.81795	-280.7059
126	0.0977	977367.68	-0.5460	978033.15	602.2820	218.3901	0.75548	-280.8146
127	0.1007	977368.47	-0.5495	978033.15	601.6114	218.1469	0.88823	-280.3286
128	0.1033	977370.15	-0.5515	978033.16	600.3507	217.6898	1.17611	-279.1634
129	0.0270	977378.64	-0.5720	978033.19	591.6377	214.5304	5.26622	-272.1733
130	0.0301	977378.44	-0.5727	978033.19	591.0134	214.3040	5.77298	-272.2723
131	0.0317	977380.10	-0.5686	978033.19	588.9930	213.5714	7.72111	-269.9398
132	0.0334	977380.59	-0.5634	978033.18	588.2475	213.3011	8.58104	-269.0541
133	0.0356	977379.41	-0.5611	978033.17	590.4222	214.0896	6.29158	-271.1355
134	0.0376	977379.31	-0.5585	978033.17	591.1603	214.3573	5.65010	-271.4031
135	0.0446	977378.60	-0.5560	978033.16	592.0219	214.6697	4.97376	-272.2330
136	0.0534	977376.52	-0.5397	978033.14	591.1671	214.3598	5.64447	-274.1679
137	0.0557	977376.64	-0.5384	978033.13	591.9216	214.6334	5.04873	-274.1553
138	0.0573	977376.07	-0.5381	978033.13	591.7584	214.5742	5.17283	-274.7105
139	0.0601	977378.02	-0.5353	978033.13	588.8949	213.5358	7.82943	-271.9203
140	0.0624	977374.98	-0.5386	978033.13	591.5418	214.4956	5.34153	-275.7650

141	0.0649	977376.75	-0.5423	978033.14	591.6445	214.5329	5.26093	-274.0135
142	0.0670	977373.00	-0.5449	978033.14	594.2713	215.4854	3.52046	-277.8380
143	0.0693	977369.73	-0.5492	978033.15	601.7104	218.1828	0.86777	-279.0293
144	0.0971	977372.97	-0.5164	978033.10	597.8622	216.7874	1.91653	-277.1386
145	0.1028	977373.90	-0.5205	978033.10	595.5212	215.9386	2.87603	-276.7414
146	0.1056	977373.64	-0.5249	978033.11	594.8089	215.6803	3.23058	-277.1065
147	0.1079	977371.03	-0.5291	978033.12	599.5564	217.4018	1.38575	-278.5422
148	0.1110	977373.39	-0.5281	978033.12	595.6137	215.9721	2.83229	-277.2531
149	0.1136	977368.28	-0.5290	978033.12	605.5757	219.5844	0.27818	-278.5671
150	0.1167	977364.88	-0.5316	978033.12	610.0386	221.2027	0.00886	-279.3938
151	0.1195	977368.93	-0.5358	978033.13	602.7649	218.5652	0.66796	-279.3347
152	0.1215	977370.22	-0.5395	978033.13	600.5149	217.7493	1.13561	-279.0148
153	0.1249	977366.08	-0.5322	978033.12	605.8951	219.7002	0.24559	-280.5982
154	0.1286	977362.55	-0.5282	978033.12	612.5512	222.1137	0.02104	-280.1111
155	0.1190	977370.74	-0.5511	978033.15	601.8422	218.2306	0.84102	-277.9593
156	0.1519	977371.51	-0.5295	978033.12	599.4827	217.3750	1.40641	-278.0971
157	0.1566	977366.60	-0.5249	978033.11	608.0043	220.4650	0.08356	-278.8827
158	0.1609	977367.49	-0.5201	978033.10	607.1711	220.1629	0.13685	-278.4696
159	0.1647	977372.67	-0.5156	978033.10	600.0767	217.5904	1.24583	-276.6930
160	0.1814	977369.93	-0.5121	978033.09	604.2110	219.0895	0.44332	-277.5898
161	0.0284	977393.50	-0.5111	978033.09	567.7740	205.8773	1.62831	-276.0646
162	0.0303	977394.03	-0.5105	978033.09	567.1719	205.6590	1.44809	-276.0970
163	0.0323	977386.89	-0.5069	978033.08	577.1875	209.2907	7.36968	-270.9248
164	0.0346	977390.91	-0.5040	978033.08	568.9377	206.2993	2.02076	-277.5077
165	0.0364	977393.11	-0.5000	978033.07	565.4978	205.0519	1.01900	-278.4949
166	0.0381	977392.35	-0.5016	978033.07	570.8437	206.9904	2.80860	-274.0592
167	0.0404	977390.01	-0.5057	978033.08	573.3973	207.9164	4.21844	-273.3690
168	0.0434	977389.57	-0.5116	978033.09	573.8562	208.0828	4.52412	-273.2199
169	0.0494	977377.97	-0.5196	978033.10	591.4810	214.4736	5.38972	-272.7384

170	0.0560	977398.26	-0.4913	978033.06	558.7039	202.5885	0.09513	-278.5888
171	0.0579	977402.64	-0.4861	978033.05	553.6460	200.7544	0.03054	-277.4877
172	0.0599	977404.12	-0.4813	978033.04	553.2528	200.6119	0.04512	-276.2365
173	0.0617	977405.85	-0.4804	978033.04	551.1337	199.8435	0.17459	-275.7258
174	0.0636	977405.53	-0.4797	978033.04	551.1318	199.8428	0.17474	-276.0426
175	0.0650	977404.66	-0.4794	978033.04	551.5929	200.0100	0.13904	-276.6554
176	0.0671	977392.45	-0.4743	978033.03	573.6618	208.0123	4.39243	-270.5392
177	0.0284	977401.22	-0.4752	978033.03	559.6294	202.9241	0.15882	-274.9509
178	0.0356	977403.79	-0.4760	978033.03	556.3425	201.7322	0.00673	-274.6243
179	0.0536	977404.08	-0.4827	978033.04	554.2012	200.9557	0.01482	-275.7058
180	0.0607	977402.44	-0.4843	978033.05	555.7787	201.5278	0.00081	-276.3493
181	0.0722	977402.13	-0.4824	978033.04	555.9694	201.5969	0.00217	-276.5409
182	0.0859	977402.70	-0.4822	978033.04	555.2631	201.3408	0.00043	-276.4208
183	0.0935	977400.64	-0.4840	978033.05	558.0784	202.3617	0.06154	-276.6278
184	0.0990	977400.51	-0.4849	978033.05	558.3059	202.4441	0.07289	-276.6037
185	0.1094	977400.24	-0.4880	978033.05	559.8813	203.0154	0.17912	-275.7644
186	0.1149	977399.31	-0.4872	978033.05	560.9959	203.4196	0.28494	-275.8812
187	9.5601	977390.99	-0.4858	978033.05	558.1012	202.3699	0.06263	-286.2667
188	0.1285	977403.10	-0.4838	978033.05	554.0601	200.9046	0.01828	-276.7753
189	0.1444	977402.36	-0.4866	978033.05	554.9100	201.2128	0.00294	-276.9870
190	0.1553	977400.78	-0.4902	978033.06	557.9303	202.3079	0.05468	-276.6018
191	0.1657	977398.16	-0.4945	978033.06	561.6245	203.6475	0.35657	-276.5663
192	0.1767	977393.99	-0.4964	978033.06	567.3765	205.7332	1.50769	-275.9192
193	0.1865	977393.19	-0.4996	978033.07	570.3181	206.7998	2.57151	-273.7939
194	0.1958	977390.69	-0.5043	978033.08	573.7278	208.0362	4.43680	-272.2540
195	0.2057	977391.91	-0.5071	978033.08	571.6152	207.2701	3.18709	-273.6371

Appendix III: Magnetic data

Stations	Reading (nT)	Diurnal correction (nT)	Latitude (°)	D (°)	I (°)	IGRF (nT)	Anomaly (nT)
1	33594.2	2.0	-0.624	0.824	-22.243	33546	46.4
2	33790.8	0.2	-0.626	0.823	-22.248	33546	244.6
3	33671.2	0.4	-0.626	0.823	-22.248	33546	124.8
4	33689.8	-1.0	-0.629	0.823	-22.255	33545	145.8
5	33435.4	-2.4	-0.631	0.822	-22.260	33545	-107.2
6	33462.6	-4.0	-0.631	0.822	-22.259	33545	-78.4
7	33632.4	-5.2	-0.629	0.822	-22.254	33545	92.6
8	33666.2	-1.2	-0.627	0.823	-22.250	33546	121.4
9	33741.2	-10.0	-0.625	0.823	-22.245	33546	205.2
10	33246.8	-14.9	-0.624	0.823	-22.242	33546	-284.3
11	33829.4	-14.0	-0.624	0.823	-22.242	33546	297.4
12	33677.0	-19.0	-0.626	0.823	-22.247	33546	150.0
13	33662.6	-22.9	-0.627	0.822	-22.249	33546	139.5
14	33568.2	-4.6	-0.628	0.825	-22.257	33545	27.8
15	33663.2	-3.6	-0.623	0.826	-22.245	33545	121.8
16	33796.2	-4.0	-0.619	0.827	-22.235	33546	254.2
17	33553.0	-4.2	-0.615	0.828	-22.227	33546	11.2
18	33667.4	-10.3	-0.610	0.830	-22.216	33547	130.7
19	33436.6	-16.1	-0.606	0.831	-22.207	33547	-94.3
20	33481.8	-21.0	-0.602	0.832	-22.198	33548	-45.2
21	33422.8	-27.1	-0.597	0.834	-22.187	33548	-98.1
22	33413.4	-33.2	-0.593	0.835	-22.178	33549	-102.4
23	33879.4	16.6	-0.620	0.825	-22.234	33546	316.8
24	33635.8	18.4	-0.615	0.827	-22.223	33547	70.4

25	33641.0	20.2	-0.611	0.828	-22.214	33547	73.8
26	33512.0	21.2	-0.606	0.830	-22.203	33548	-57.2
27	33247.0	22.6	-0.602	0.831	-22.194	33548	-323.6
28	33412.0	18.6	-0.598	0.832	-22.186	33549	-155.6
29	33335.2	16.7	-0.594	0.834	-22.177	33549	-230.5
30	33484.2	13.8	-0.589	0.835	-22.166	33550	-79.6
31	33204.8	9.8	-0.585	0.837	-22.157	33550	-355.0
32	33154.6	4.1	-0.581	0.838	-22.148	33550	-399.5
33	33223.4	2.9	-0.576	0.839	-22.136	33551	-330.5
34	33502.2	-7.2	-0.572	0.840	-22.128	33551	-41.6
35	33289.6	11.0	-0.514	0.858	-21.989	33559	-280.4
36	33567.2	15.4	-0.513	0.859	-21.987	33559	-7.2
37	33401.8	16.0	-0.510	0.860	-21.980	33559	-173.2
38	33306.8	18.6	-0.507	0.860	-21.972	33560	-271.8
39	33332.6	17.2	-0.503	0.861	-21.963	33560	-244.6
40	32893.4	17.3	-0.504	0.862	-21.968	33560	-683.9
41	33255.8	20.4	-0.508	0.861	-21.978	33559	-323.6
42	33472.4	22.0	-0.514	0.860	-21.992	33558	-107.6
43	33429.6	-0.8	-0.522	0.857	-22.010	33557	-126.6
44	33303.0	-3.2	-0.494	0.864	-21.942	33561	-254.8
45	33408.8	-18.7	-0.489	0.865	-21.930	33562	-134.5
46	33441.2	-26.0	-0.484	0.866	-21.919	33563	-95.8
47	33334.8	-27.2	-0.483	0.868	-21.919	33562	-200.0
48	33397.6	-34.3	-0.482	0.869	-21.918	33562	-130.1
49	33526.0	-34.0	-0.482	0.869	-21.920	33562	-2.0
50	33270.2	-27.0	-0.477	0.867	-21.900	33564	-266.8
51	33560.6	-27.0	-0.478	0.867	-21.902	33564	23.6
52	33215.4	0.5	-0.478	0.868	-21.903	33564	-349.1
53	33399.4	-1.8	-0.479	0.868	-21.906	33563	-161.8

54	33736.2	0.7	-0.485	0.868	-21.924	33562	173.5
55	33582.2	-2.8	-0.487	0.867	-21.930	33562	23.0
56	33755.6	-5.2	-0.485	0.868	-21.926	33562	198.8
57	33344.6	3.4	-0.485	0.869	-21.927	33561	-219.8
58	33751.2	5.6	-0.487	0.868	-21.931	33561	184.6
59	33935.2	5.8	-0.488	0.868	-21.933	33561	368.4
60	33597.2	6.2	-0.491	0.867	-21.940	33561	30.0
61	33649.8	4.3	-0.490	0.867	-21.938	33561	84.5
62	33985.8	0.7	-0.489	0.868	-21.937	33561	424.1
63	33340.8	-2.6	-0.487	0.869	-21.933	33561	-217.6
64	33379.2	-9.2	-0.489	0.869	-12.940	33560	-171.6
65	33420.0	-9.2	-0.493	0.868	-21.949	33560	-130.8
66	33235.2	-3.5	-0.497	0.867	-21.959	33559	-320.3
67	33295.8	-2.4	-0.499	0.866	-21.963	33559	-260.8
68	33050.6	-9.6	-0.502	0.865	-21.969	33559	-498.8
69	33259.2	-13.4	-0.507	0.864	-21.980	33558	-285.4
70	33496.4	-15.2	-0.510	0.864	-21.989	33558	-46.4
71	33457.2	4.6	-0.511	0.862	-21.986	33558	-105.4
72	33873.4	5.6	-0.515	0.861	-21.996	33558	309.8
73	33014.0	0.4	-0.515	0.861	-21.998	33557	-543.4
74	33090.0	2.6	-0.513	0.862	-21.995	33557	-469.6
75	33061.0	0.4	-0.513	0.863	-21.995	33557	-496.4
76	33423.0	-4.4	-0.509	0.866	-21.991	33557	-129.6
77	33277.4	4.5	-0.574	0.842	-22.133	33551	-278.1
78	33444.4	5.4	-0.574	0.842	-22.131	33551	-112.0
79	33210.4	5.7	-0.578	0.843	-22.145	33550	-345.3
80	33417.6	6.0	-0.579	0.843	-22.150	33549	-137.4
81	33315.8	6.1	-0.582	0.843	-22.158	33549	-239.3
82	33223.4	6.2	-0.580	0.844	-22.155	33549	-331.8

83	33230.4	5.8	-0.578	0.845	-22.152	33549	-324.4
84	33287.6	6.4	-0.579	0.846	-22.156	33548	-266.8
85	33297.2	6.2	-0.575	0.849	-22.151	33548	-257.0
86	33228.8	5.0	-0.572	0.850	-22.144	33548	-324.2
87	33211.0	4.4	-0.573	0.849	-22.147	33548	-341.4
88	33289.4	3.8	-0.573	0.850	-22.148	33548	-262.4
89	33324.2	4.1	-0.573	0.850	-22.149	33548	-227.9
90	33287.6	2.6	-0.565	0.851	-22.128	33549	-264.0
91	33217.4	2.2	-0.567	0.851	-22.133	33549	-333.8
92	33388.8	0.8	-0.565	0.852	-22.128	33549	-161.0
93	33247.0	-1.2	-0.563	0.852	-22.124	33549	-300.8
94	33750.4	-3.6	-0.562	0.853	-22.122	33549	205.0
95	33203.4	-3.6	-0.560	0.853	-22.117	33550	-343.0
96	33415.4	-5.6	-0.559	0.853	-22.114	33550	-129.0
97	33476.8	-9.6	-0.556	0.854	-22.107	33550	-63.6
98	32957.0	-9.5	-0.556	0.853	-22.106	33550	-583.5
99	33721.0	-8.0	-0.556	0.853	-22.105	33551	178.0
100	33629.0	-8.4	-0.554	0.853	-22.100	33551	86.4
101	33371.6	6.4	-0.569	0.843	-22.118	33552	-186.8
102	33252.6	6.5	-0.567	0.843	-22.113	33552	-305.9
103	33149.0	5.0	-0.566	0.843	-22.111	33552	-408.0
104	33249.0	4.4	-0.564	0.844	-22.107	33552	-307.4
105	33178.4	3.8	-0.563	0.845	-22.105	33553	-378.4
106	33318.0	4.1	-0.560	0.846	-22.099	33553	-239.1
107	33297.0	4.2	-0.559	0.846	-22.096	33553	-260.2
108	33207.4	4.2	-0.558	0.846	-22.094	33553	-349.8
109	33220.4	4.2	-0.555	0.847	-22.087	33553	-336.8
110	33328.2	4.1	-0.553	0.848	-22.083	33554	-229.9
111	33495.8	4.0	-0.551	0.849	-22.079	33554	-62.2

112	33339.6	3.6	-0.549	0.849	-22.075	33554	-218.0
113	33244.8	2.9	-0.547	0.850	-22.070	33554	-312.1
114	33556.0	2.7	-0.546	0.850	-22.068	33554	-0.7
115	33636.2	2.3	-0.545	0.851	-22.067	33554	79.9
116	33014.6	1.5	-0.543	0.851	-22.062	33554	-540.9
117	33283.2	-1.0	-0.542	0.852	-22.060	33554	-269.8
118	33117.2	-2.0	-0.541	0.852	-22.057	33555	-435.8
119	32971.2	-2.6	-0.540	0.852	-22.055	33555	-581.2
120	33591.6	-4.0	-0.538	0.853	-22.050	33555	40.6
121	32990.2	-6.6	-0.539	0.852	-22.052	33555	-558.2
122	33505.2	-8.8	-0.541	0.852	-22.057	33555	-41.0
123	33208.2	-9.5	-0.541	0.851	-22.056	33555	-337.3
124	33971.6	-9.3	-0.541	0.851	-22.055	33555	425.9
125	33339.2	-9.5	-0.543	0.850	-22.059	33555	-206.3
126	33547.0	-9.7	-0.542	0.850	-22.056	33555	1.7
127	33475.2	-9.6	-0.542	0.850	-22.055	33555	-70.2
128	33502.2	-7.6	-0.543	0.849	-22.057	33555	-45.2
129	33249.0	-8.0	-0.544	0.849	-22.059	33555	-298.0
130	33243.4	-9.0	-0.546	0.849	-22.064	33555	-302.6
131	33221.8	-8.9	-0.549	0.848	-22.070	33555	-324.3
132	33238.6	-8.4	-0.551	0.847	-22.075	33554	-307.0
133	32641.8	-7.5	-0.553	0.846	-22.079	33554	-904.7
134	33316.2	-7.4	-0.556	0.845	-22.086	33554	-230.4
135	33140.8	-8.2	-0.558	0.845	-22.091	33554	-405.0
136	32977.4	-7.6	-0.560	0.844	-22.095	33553	-568.0
137	32929.4	-7.8	-0.562	0.844	-22.101	33553	-615.8
138	33010.8	10.6	-0.575	0.846	-22.144	33549	-548.8
139	33342.6	12.4	-0.576	0.846	-22.148	33549	-218.8
140	33057.4	14.0	-0.571	0.848	-22.136	33549	-505.6

141	33466.2	12.6	-0.566	0.849	-22.124	33550	-96.4
142	33182.0	13.6	-0.564	0.849	-22.119	33550	-381.6
143	33046.6	15.9	-0.561	0.850	-22.112	33551	-520.3
144	33124.8	16.8	-0.559	0.851	-22.108	33551	-443.0
145	33171.4	9.8	-0.554	0.845	-22.079	33554	-392.4
146	33283.6	9.1	-0.552	0.845	-22.073	33555	-280.5
147	33076.0	7.5	-0.549	0.844	-22.062	33556	-487.5
148	33204.6	6.2	-0.545	0.845	-22.052	33557	-358.6
149	33098.8	5.4	-0.540	0.847	-22.041	33557	-463.6
150	33254.2	4.1	-0.537	0.848	-22.034	33557	-306.9
151	33651.4	2.5	-0.536	0.848	-22.033	33557	91.9
152	33307.6	2.4	-0.527	0.851	-22.012	33559	-253.8
153	33262.6	2.2	-0.524	0.852	-22.005	33559	-298.6
154	33291.8	2.5	-0.519	0.853	-21.993	33560	-270.7
155	33362.8	2.5	-0.515	0.854	-21.984	33560	-199.7
156	33695.6	2.5	-0.509	0.856	-21.970	33561	132.1
157	33247.6	2.2	-0.505	0.857	-21.961	33561	-315.6
158	33374.4	1.8	-0.501	0.858	-21.952	33562	-189.4
159	33276.6	0.8	-0.498	0.859	-21.945	33562	-286.2
160	33007.4	0.4	-0.495	0.860	-21.940	33562	-555.0
161	33347.0	-0.2	-0.492	0.861	-21.933	33563	-215.8
162	33439.2	-1.0	-0.487	0.863	-21.922	33563	-122.8
163	33658.2	-1.2	-0.484	0.864	-21.915	33564	95.4
164	33611.2	-1.7	-0.479	0.865	-21.904	33564	48.9
165	33359.8	5.2	-0.519	0.854	-21.995	33559	-204.4
166	33215.8	2.8	-0.523	0.853	-22.004	33559	-346.0
167	33352.4	1.8	-0.528	0.851	-22.015	33558	-207.4
168	33265.8	1.2	-0.532	0.849	-22.023	33558	-293.4
169	33350.0	0.2	-0.531	0.850	-22.022	33558	-208.2

170	33283.2	-1.5	-0.532	0.851	-22.027	33557	-272.3
171	33160.0	-3.2	-0.534	0.851	-22.033	33557	-393.8
172	33330.4	-5.4	-0.539	0.850	-22.046	33556	-220.2
173	33309.2	-6.8	-0.542	0.850	-22.054	33555	-239.0
174	33165.0	-10.8	-0.535	0.851	-22.037	33557	-381.2
175	33271.6	-11.8	-0.531	0.852	-22.027	33557	-273.6
176	33811.8	-8.3	-0.621	0.826	-22.237	33546	274.1
177	33538.4	-0.6	-0.616	0.827	-22.226	33547	-8.0
178	33638.0	5.2	-0.612	0.829	-22.217	33547	85.8
179	33552.2	9.4	-0.609	0.830	-22.211	33547	-4.2
180	33700.0	12.4	-0.605	0.831	-22.202	33548	139.6
181	33581.8	15.4	-0.600	0.833	-22.191	33548	18.4
182	33492.0	18.2	-0.596	0.834	-22.182	33549	-75.2
183	33414.0	18.3	-0.592	0.835	-22.173	33549	-153.3
184	33375.2	17.0	-0.588	0.836	-22.164	33549	-190.8
185	33286.6	18.4	-0.583	0.838	-22.153	33550	-281.8
186	33100.4	18.1	-0.579	0.839	-22.145	33550	-467.7
187	33363.4	18.4	-0.574	0.841	-22.133	33551	-206.0
188	33728.0	10.2	-0.621	0.825	-22.234	33547	170.8
189	33659.0	8.0	-0.616	0.826	-22.223	33547	104.0
190	33436.8	16.4	-0.612	0.828	-22.214	33548	-127.6
191	33529.6	14.4	-0.608	0.829	-22.205	33548	-32.8
192	33550.6	10.2	-0.603	0.830	-22.194	33548	-7.6
193	33332.8	10.8	-0.599	0.832	-22.185	33549	-227.0
194	33430.2	8.3	-0.594	0.833	-22.173	33550	-128.1
195	32573.6	10.7	-0.590	0.834	-22.164	33550	-987.1
196	32944.2	6.5	-0.585	0.836	-22.152	33551	-613.3
197	33291.0	7.2	-0.581	0.837	-22.143	33551	-267.2
198	33319.8	8.8	-0.576	0.838	-22.132	33552	-241.0

199	33246.4	7.8	-0.572	0.839	-22.123	33552	-313.4
200	33218.8	7.1	-0.567	0.841	-22.111	33553	-341.3
201	33197.6	6.3	-0.563	0.842	-22.102	33553	-361.7
202	33562.0	7.5	-0.623	0.827	-22.245	33545	9.5
203	33729.6	9.5	-0.619	0.828	-22.236	33546	174.1
204	33461.8	14.3	-0.615	0.830	-22.227	33546	-98.5
205	33645.0	14.8	-0.611	0.831	-22.219	33546	84.2
206	33462.4	16.4	-0.606	0.832	-22.207	33547	-101.0
207	33378.4	15.7	-0.602	0.833	-22.198	33547	-184.3
208	33512.2	15.9	-0.617	0.835	-22.246	33543	-46.7
209	33385.6	12.6	-0.613	0.836	-22.236	33544	-171.0
210	33490.8	7.1	-0.608	0.837	-22.225	33544	-60.3
211	33493.2	-5.6	-0.605	0.838	-22.218	33545	-46.2
212	33347.0	-14.8	-0.601	0.840	-22.210	33545	-183.2
213	33474.2	-19.7	-0.599	0.841	-22.207	33545	-51.1
214	33483.6	-15.8	-0.598	0.842	-22.207	33545	-45.6
215	33641.4	-17.4	-0.601	0.842	-22.215	33544	114.8
216	33484.4	-19.8	-0.603	0.842	-22.222	33544	-39.8
217	33366.6	-22.1	-0.596	0.843	-22.204	33545	-156.3
218	33440.0	-26.2	-0.592	0.844	-22.193	33545	-78.8
219	33371.4	-28.0	-0.588	0.845	-22.184	33546	-146.6
220	33303.6	-30.4	-0.583	0.847	-22.173	33547	-213.0
221	33301.0	-39.0	-0.576	0.849	-22.157	33547	-207.0
222	33420.0	70.8	-0.631	0.829	-22.273	33542	-192.8
223	33610.6	70.8	-0.628	0.830	-22.267	33543	-3.2
224	33584.8	69.0	-0.625	0.832	-22.261	33543	-27.2
225	33581.0	73.4	-0.620	0.833	-22.249	33543	-35.4
226	33548.8	70.4	-0.621	0.832	-22.250	33544	-65.6
227	33503.8	56.4	-0.617	0.833	-22.240	33544	-96.6

228	33530.6	45.9	-0.615	0.833	-22.234	33545	-60.3
229	33476.0	33.8	-0.613	0.833	-22.227	33545	-102.8

Appendix IV: Structural Index (SI)

Geologic model	Number of infinite dimensions	Gravity SI	Magnetic SI
Sphere	0	2	3
Pipe	1 (z)	1	2
Horizontal cylinder	1 (x-y)	1	2
Dyke	2 (z and x-y)	0.5	1
Sill	2 (x and y)	0.5	1
Thick step/Contact	3 (x, y and z)	-	0.5

Appendix V: Instrumental drift curve for gravity station 1

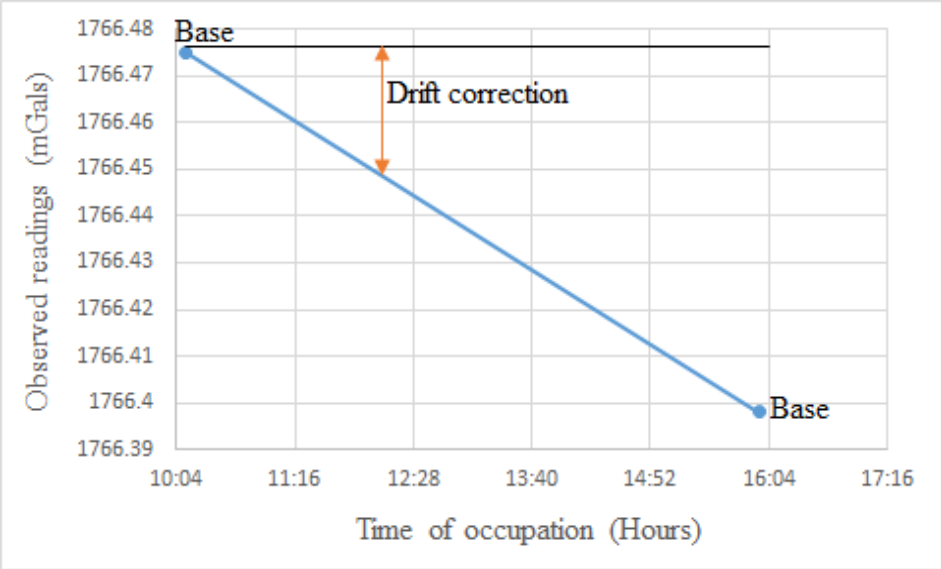

Appendix VI: Diurnal curve for magnetic station 1